

**Use of pointed water vapor radiometer observations
to improve vertical GPS surveying accuracy**

by

Fredrick Stuart Solheim

B.S., Engineering Physics, University of Colorado 1967

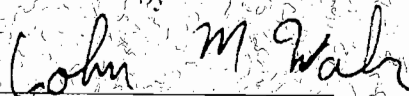
M.S., Astrophysics, University of Colorado 1969

A thesis submitted to the
Faculty of the Graduate School of the
University of Colorado in partial fulfillment
of the requirements for the degree of
Doctor of Philosophy
Department of Physics

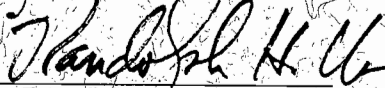
1993

This thesis for the Doctor of Philosophy degree by
Fredrick Stuart Solheim
has been approved for the
Department of Physics

by



John M. Wahr



Randolph H. Ware

Date 11/19/93

Abstract

Atmospheric water vapor is a source of propagation delay, and therefore error, in Global Positioning System (GPS) geodesy. While GPS geodesy is now capable of millimeter level positioning, unmodelled water vapor can result in errors of several centimeters. Anisotropies in water vapor observed at ground sites have prompted the investigation into their effect upon GPS geodesy. Driven by the geophysical community's desire for more accurate baseline measurements, several previous attempts to improve geodesy with pointed water vapor radiometer (WVR) observations yielded dubious results.

The development of an accurate, stable, steerable portable microwave water vapor radiometer, as well as improved oxygen and water vapor line shape models, has made possible more accurate water vapor measurements along the propagation paths to the GPS satellites. This radiometer development started in 1987 with funding from the Department of Commerce and still continues.

This thesis will discuss the considerations relating to ionospheric and atmospheric refractivity (which induces phase delay in GPS signals) and to atmospheric microwave absorption (related to the microwave radiometer observable, emission). The microwave radiometer, its development, and its theoretical and measured performance characteristics are also described. Finally, a four month field experiment, called WVR92, is described wherein pointed water vapor radiometer observations were incorporated into modified GPS analysis software to correct for anisotropies in water vapor. A factor of two improvement was realized over stochastic methods and over zenith only WVR measurements.

An interesting corollary finding resulted from this field experiment; it was found that, if the GPS position software were allowed to estimate the

tropospheric water vapor by minimizing position residuals in a least squares sense, the zenith *difference* in water vapor burdens between GPS antenna locations could be measured to within a millimeter or so. Absolute water vapor burdens can be determined if WVR observations are taken at one of the GPS sites. This finding is of great interest to the meteorological community, and has triggered the installation of GPS receivers for water vapor measurements at meteorological network sites.

ACKNOWLEDGEMENTS

I would like to thank my thesis advisor, Randolph “Stick” Ware, for his longstanding and unwavering encouragement and prodding, as well as his insightful suggestions. I would like also to thank my titular thesis advisor, John Wahr, for agreeing to be so, in spite of his full schedule. Chris Röcken of the University Navstar Constortium (UNAVCO) gave valuable guidance during the field experiment.

I would like to thank Dr. Ed Westwater, Division Chief of the Environmental Radiometry Division of NOAA’s Environmental Technology Laboratory (formerly the NOAA Wave Propagation Laboratory), and also of my thesis committee, for making access to NOAA data, publications, and facilities effortless. Data included many months of surface meteorology and zenith WVR data from NOAA’s Platteville facility and furnished by Janelle Reynolds. Michael Falls furnished data for several ancillary experiments. Dedicated telephone access between Boulder and Platteville was implemented by Rich Beeler. Access to the Denver Stapleton site and Platteville was coordinated through Duane Hazen and Bill Madsen. And enlightening discussion and pertinent suggestions regarding radiometer hardware occurred with Jim Jordan of NOAA Environmental Technology Laboratory.

Much of the computing was accomplished by Teresa Van Hove, Chris Alber, and Jim Johnson of UNAVCO. They deserve recognition for their talented contributions.

RAOBs were made accessible by Mark Govett of the Forecast Systems Laboratory of NOAA. Retrieval inversion software was furnished by Steve Keihm of JPL through Jim Liljegren of the Department of Energy ARM Project.

The two water vapor radiometers used in this experiment were furnished gratis by Radiometrics Corporation of Boulder Colorado.

This work was accomplished under NSF support EAR-9117568, *Development of Tropospheric Correction Techniques to Optimize Vertical GPS Accuracy*.

Table of Contents

Chapter 1 Introduction	1
1.1 The Global Positioning System (GPS)	1
1.2 Importance of vertical accuracy in GPS geodesy	2
1.3 Need for tropospheric corrections in GPS geodesy	5
1.4 Overview of thesis	6
Chapter 2 Atmospheric and ionospheric radio refractivity and absorption	9
2.1 The delay due to the ionospheric plasma	11
2.2 Atmospheric refractive radio phase path delays	16
2.2.1 Phase path refractive delay due to the “dry” atmosphere	19
2.2.2 Water vapor: general atmospheric distribution	20
2.2.3 Phase path refractive delay due to water vapor	23
2.2.4 Phase path refractive delay due to non-gaseous tropospheric constituents	24
1) Phase delay due to cloud, rain, fog, and haze	25
2) Phase delay due to snow, glaciated clouds	27
3) The radio propagation delay due to scattering	28
4) Phase delay due to aerosols	29
2.2.5 Summary of atmospheric refractivity	30
2.3 atmospheric water vapor and oxygen absorption	31

Chapter 3 Microwave radiometers	
and water vapor measurements	34
3.1 The basis for microwave remote sensing of water vapor;	
partial linearization of the Radiative Transfer Equation	34
3.2 Retrieval coefficients for water vapor radiometers	37
3.3 The importance of the atmospheric Mean Radiating Temperature	
and the mean water vapor temperature	42
3.3.1 Atmospheric mean temperatures	
and liquid water (cloud) retrieval	45
3.3.2 Mapping functions	46
3.4 Line shape and continuum absorption models	49
3.5 Conversion of relative humidity or temperature-dewpoint	
data to water vapor density	50
3.6 Discussion of WVR instrumental and retrieval errors and sources	52
3.6.1 RAOB errors	52
3.6.2 Statistical and instrumental errors of retrieval methods	53
3.6.3 Instrumental errors	55
3.6.4 Errors in Mean Radiating Temperature	55
3.6.5 Radiometer leveling errors	56
3.7 Generation of retrieval coefficients for WVR92	58

Chapter 4 The water vapor radiometers	
used in these experiments	60
4.1 Description of the Radiometrics WVR-1100 radiometer	60
4.1.1 Overview of the radiometer	60
4.1.2 Electronic description of the radiometer	62
4.1.3 Radiometer modifications	62
4.2 The resolving power, ΔT ,	
of the Radiometrics WVR-1100 radiometer	65
4.3 Uncertainty in phase path delay	
as a function of uncertainty in brightness	72
4.4 WVR-1100 receiver Noise Figure	73
4.5 Demonstration of accuracy and precision;	
WVR intercomparisons and LN2 target tests at Boulder	77
4.5.1 Intercomparison	77
4.5.2 Verification of the tip curve calibration of the radiometer	78
4.6 WVR-1100 receiver gain temperature coefficient	82
4.6.1 Antenna system analysis	83
1) Etalon effects of	
the Microwave window and Rexolite TM lens	83
a) The microwave window	83
b) The plano-parabolic Rexolite lens	84
2) Temperature dependent dielectric effects	
of the microwave window and Rexolite lens	84
3) The corrugated feed horn and the waveguide	85
4.6.2 Temperature coefficient of the	
system electronics - the analog board	91
4.6.3 Conclusions regarding the temperature coefficient of gain	93
4.6.3.1 Antenna system	93
4.6.3.1 Electronics	94

4.7 Observation reduction algorithms of the	
Radiometrics WVR-1100 water vapor radiometer	94
4.7.1 The radiometer measurements	94
4.7.2 The radiometer equation	95
4.7.3 Tipping (tip) curves as calibration	95
4.7.4 Line of sight measurements	98
4.7.5 Software corrections to the measurements	99
1) Hydrocarbon window correction	95
2) Antenna beamwidth corrections	100
3) Receiver temperature correction	102
4.7.6 Quality control algorithms	104
Chapter 5 The WVR and geodesy experiments and Results	105
5.1 The UNAVCO-Platteville baseline	105
5.2 Results	107
5.2.1 Experimental errors	114
1) Retrieval errors	114
2) WVR errors	114
3) GPS orbit errors	114
4) GPS receiver temperature coefficient	115
5) Nonzero mean antenna multipath effects	115
6) Total rms error	115
7) Bias due to the barometers	115
5.2.2 Sensitivity to length of data set for daily solutions	115
5.2.3 Short baseline insensitivity	
to errors in T_{mr} and in retrieval coefficients	117
5.2.3 Inference of water vapor from GPS solutions	117
Chapter 6 Epilogue - an improved follow-on Experiment	120
References	122

TABLES

TABLE 2.1 Sources, magnitudes, uncertainties of propagation delay	10
TABLE 2.2 Typical particle sizes, delays, occurrences	30
TABLE 3.1 Radiometer leveling errors	57
TABLE 4.1 Average point-to-point noise of blackbody observations	65
TABLE 4.2 The theoretical resolving power, ΔT , of various radiometer types	67
TABLE 4.3 WVR-1100 Measurement uncertainties	69
TABLE 4.4 WVR-1100 Component losses	76
TABLE 4.5 WVR-1100 Cryogenic target measurements	81
TABLE 4.6 Sources and magnitudes of WR34 waveguide losses and temperature coefficients	89
TABLE 4.7 VSWR and Reflection Coefficients	91
TABLE 5.1 Vertical repeatabilities (mm) under different measurement and analysis methods	111
TABLE 5.2 Comparison of Retrieval Coefficients with old and new line shape models	117

FIGURES

FIGURE 1.1 Gradient measurements from the TOPEX Harvest oil platform.	6
FIGURE 2.1 Saturation water vapor pressure as a function of temperature.	21
FIGURE 2.2 The atmospheric absorption spectrum between 0 and 40 GHz.	32
FIGURE 3.1 The spectrum of a humid atmosphere at several pressures.	39
FIGURE 3.2 Radiometer receiver antenna temperature vs. total integrated atmospheric water vapor for 531 RAOBs at Denver in 1991.	40
FIGURE 3.3 The mean radiating temperature of the atmosphere above Denver for the year 1991.	43
FIGURE 3.4 Plot of the ratio of vapor-induced phase path delay to total integrated water vapor, from Denver 1991 RAOBs.	44
FIGURE 4.1 The WVR-1100 microwave water vapor radiometer	61
FIGURE 4.2 Noise spectra of the water vapor radiometer.	70
FIGURE 4.3 Intercomparison of WVR7 and WVR8.	77
FIGURE 4.4 The cryogenic blackbody target.	80
FIGURE 4.5 WVR observations of the cryogenic target.	81
FIGURE 5.1 Typical field data.	108
FIGURE 5.2 Comparison of the several data reduction methods.	112
FIGURE 5.3 Difference in height of UNAVCO and Platteville, as determined by the various data reduction methods.	113
FIGURE 5.4 Comparison of zenith water vapor burdens as estimated by GPS solutions and as measured by WVRs.	119

Chapter 1 Introduction

1.1 The Global Positioning System (GPS)

Beginning in the late 1970s the U.S. Department of Defense began launching the Global Positioning Satellite System for navigation, time transfer, and positioning. These measurements are accomplished via timing of the propagation delay from each of the satellites to passive receivers. Although the original military goal was real-time positioning of a single receiver with about 10 meters rms error, and in spite of several intentional degradations of accuracy of the system, technologies and techniques have pushed baseline length accuracies via differential or relative positioning techniques from several centimeters in the mid 1980s to the current precision of several millimeters.

As of this year the planned constellation of 21 satellites and 3 spares is nearly complete. There are currently 25 satellite vehicles in 6 orbital planes, several of which are replacing aging and less accurate *Block I* satellites. These vehicles are in nominally 12 hour orbits at an altitude of about 19,700 km. The inclination and spacing of orbital planes is such that at least 6 satellites are in view at all times and over most of the globe. A minimum of 4 satellites are required to determine 3 axes of position and clock error.

The satellites transmit timing information at 1.2276 GHz (L_2) and 1.57542 GHz (L_1); these carriers are multiplied up from a common stable Rb or Cs clock oscillator at 10.23MHz (actually 4.5×10^{-10} below this to offset the gain in frequency because the photons propagate to receivers in lower gravitational potential). The clock stability of about $1 : 10^{13}$ does not preclude clock drift induced errors, so *single* and *double differencing* techniques are utilized to remove clock and other errors common in mode to the receivers. These “other” errors can include ionospheric, tropospheric, and GPS orbital errors. *Single differencing* is

the differencing of the phase path lengths from two receivers to a single satellite; *double differencing* is the differencing of *single differences* for two satellites.

The L_2 carrier is modulated at 10.23 MHz (P code), and L_1 at 10.23 and 1.023 MHz (the C/A code). The P code is a pseudorandom biphasic modulation, repetitive in 35 weeks but renewed each week. The C/A code on L_1 is in quadrature to the P code. Without knowledge of the P code, single receiver accuracy is limited to about 50 meters.

Two forms of accuracy degradation have been imposed upon civilian users by the Department of Defense. S/A, or selective availability, involves dithering of the oscillator clock frequency by several cycles over periods of several minutes. Simple precautions, however, can eliminate the effect of S/A on precise geodesy [Röcken and Meertens, 1991]. The predictive orbit ephemerides that are modulated onto the carrier (called broadcast orbits) are also degraded under S/A. Under A/S (antispoofing), the P code is being occasionally replaced with a more cryptic Y code.

Precise geodesy is achieved by determining the total carrier phase between the satellites and the receiver. This phase path length is subject to refractivity in the ionosphere and atmosphere, which must be modeled out or measured. We continue to better understand these and other sources of error. Care in making GPS observations is currently yielding accuracies of $1 : 10^8$ to $1 : 10^9$ of the baseline length in some cases (1 centimeter between the U.S. and Europe).

1.2 Importance of vertical accuracy in GPS geodesy

The most precise method of measuring vertical position on short baselines is by spirit leveling, but this is expensive and is generally not applicable (e.g. island sites, difficult terrain). Absolute gravity measurement gives a vertical uncertainty of less than 1 cm, but is expensive and requires skillful operators and the ability to correct for subsurface water and atmospheric variations. VLBI and satellite laser ranging are likewise expensive and require a significant facility at each observing site. GPS offers a relatively inexpensive portable and accurate

alternative that functions on all baseline lengths and across any terrain.

The vertical resolution of GPS is generally about a factor of 3 worse than the horizontal because position solutions are not constrained by satellites in the hemisphere below the antenna. Yet, because GPS geodesy has evolved (to ppb accuracy under certain circumstances), subcentimeter accuracies in the vertical dimension are now being attained. The largest remaining errors for vertical accuracy are the uncertainty in the troposphere and its varying structure, and antenna multipath propagation. Multipath can be removed by long observation periods (days) which tend to randomize the multipath error. The troposphere, on the other hand, requires accurate estimation or direct measurement.

Some of the more obvious geodetic needs are mentioned below.

Tide gauges, global change: In an effort to gain knowledge and understanding of global change, the absolute sea surface elevation is being monitored, as it is a direct thermometer of global warming. Unfortunately, there are difficulties in determining the trend and rate of the sea surface change in a timely manner. During the past century the sea level has risen at a rate of 1 to 3 *mm/year*. The NRC's Board on Atmospheric Sciences and Climate and others estimate the sea level may rise 70 cm within the next century. Note that increasing accuracy in vertical measurements by a factor of 3 can enable us to define trends in about 3 years rather than 10 years.

The possibility that the sea level may be accelerating or decelerating in trend is of enormous consequence for civilization. Significant long-term planning is in order to minimize the consequences on and to preserve human life, communities, facilities, and the environment. Because of the possible magnitude of the impact of rising sea levels, accurate monitoring of sea surface elevation and rate of change are necessary.

Current estimates of the velocity of sea level change have large uncertainties due to inadequacies in observational stability and ignorance in interpretation, yet these estimates are based on studies of 60 to 100 years of data. If we are to obtain an improved and more timely measure of velocity we need at least an

order of magnitude increase in measurement accuracy. One major problem in estimating sea level rise is a variance at periods of several years that exceeds 5 cm. A new network of tidal gauges (known by the acronym GLOSS) will provide a more uniform coverage of the world's oceans and it is proposed that these gauges will be related to a vertical datum based on a VLBI-derived frame of reference. Since VLBI site occupations are very expensive, a minimal number of VLBI installations could be tied to numerous tide gauges by GPS if difficulties in correcting for the wet troposphere could be overcome.

Glacial rebound and postseismic displacements: The rebound of the Earth's crust with the change in ice loading produces crustal changes that must be considered in local vertical references such as historical and current tide gauge measurements. Rebounds are generally of the magnitude of several mm/year; resolute measurements must therefore be made to assess such motions in acceptable time intervals.

Seismic displacements can affect strain fields far from the seismic event. The Landers event of June 28 1992 exhibited cm-level vertical displacements more than 50 *km* away from the rupture [Massonnet et al., 1993]. Creep displacements are much smaller, even proximate to the fault. Precise GPS offers a tool for measuring such displacements.

Satellite altimetry: Absolute calibration of satellite altimeters such as the TOPEX-Poseidon altimeter require precise measurement of vertical references over short time periods. For instance, TOPEX is calibrated against the (changing) sea surface offshore, which is in turn determined through GPS geodesy. The importance of water vapor measurements in this calibration is two-fold: the altimeter propagation is subject to the refractivity of water vapor, and the GPS-measured vertical position of the sea surface likewise requires knowledge of the water vapor.

Airborne gravity measurements: Airborne gravity measurements are currently being made at a resolution of about 3 milligals over 3 *km*. Analysis of current GPS and gravity sensor capabilities indicate that 1 milligal over 1

km may be achievable. Critical to this measurement is precise knowledge of the vertical position of the airborne platform (centimeter level) in time, because the second time derivative of this vertical position is acceleration, which is indistinguishable by the gravity sensor from gravitational acceleration. To achieve the above accuracy will require measurement from the platform of water vapor above the platform.

1.3 Need for Tropospheric Corrections in GPS Geodesy

There has been some evidence in the literature of the anisotropy of atmospheric water vapor [Snider, 1984], and more specifically, that these anisotropies effect GPS geodesy [Röcken, 1988; Röcken et al., 1991; Ware et al, 1986; Morgan et al., 1990].

Elgered et al. [1990] find rms values of temporal time gradients at Onsala of 0.63 cm/hour in a study of 11,500 cases. Similar gradients were found at Kauai ($.63 \text{ cm/hour}$), Fort Davis TX ($.47 \text{ cm/hour}$), and Mojave ($.40 \text{ cm/hour}$) VLBI sites. These gradients are generally associated with change in air parcels due to horizontal flow, and are therefore also manifested as spatial gradients. Unless corrected for, these spatial gradients induce position errors in GPS solutions.

In August of 1990 we gathered data with an early model Radiometrics water vapor radiometer in concert with the TOPEX Harvest oil platform experiment located about 10 km off the coast of Santa Barbara. Part of the observing scheme was to measure water vapor along paths at 30 degrees of elevation and in 4 orthogonal directions. Shown are brightness temperature (blackbody temperature) measurements of the sky, which are highly correlated to atmospheric water vapor. These several days of observations revealed a chronic gradient in water vapor from northeast (shoreward) to southwest (seaward) that persisted for several days, then shifted to a gradient from southeast to northwest. The magnitude of this gradient was about a 15% difference in water vapor along these slanted observation paths. The anisotropic data are shown in Figure 1.1 below.

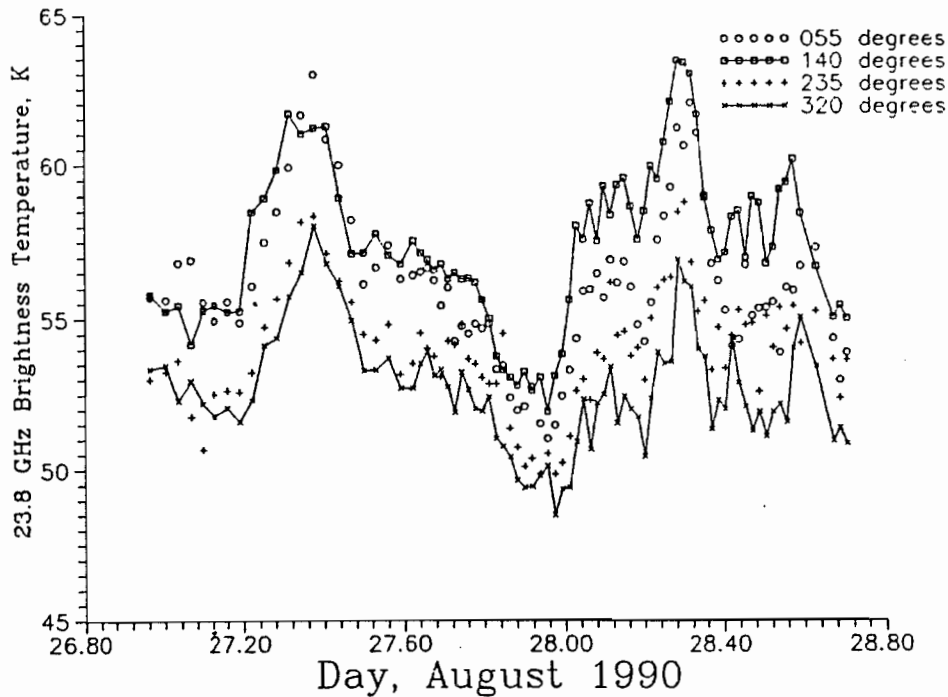


FIGURE 1.1 Sky brightness temperature measurements at 23.8 GHz and at 30 degree elevation angle observed from the Texaco Harvest offshore oil platform are shown. A chronic gradient from southeast to northwest can be seen. This gradient rotated and diminished with the passage of a weather front on day 29.

Errors in zenith delay of an azimuthally symmetric troposphere manifest themselves as errors in vertical position only, and by a factor of 2.6 to 3.9 (depending upon latitude) times the zenith delay [Rothacher, 1992]. Unmodeled spatial gradients or other inhomogenities in the troposphere manifest themselves mostly in vertical errors rather than horizontal coordinate errors. The tropospheric wet delay generally dominates other error sources in precise geodesy when high-accuracy analysis methods and precise orbits are utilized.

1.4 Overview of Thesis

Prior GPS geodesy experiments with water vapor radiometers produced

mixed results. Vertical uncertainties exceeded 10 *mm* for baselines of lengths from several *km* up to 2000 *km* [Ware et al., 1986; Tralli et al., 1988, and Tralli and Lichten, 1990; Davis et al. 1989; Dixon and Kornreich Wolf, 1990; Dixon et al, 1991]. Errors independent of baseline length were experienced, indicating that tropospheric wet delay errors were larger than orbit errors. These experiments utilized previous generation WVRs with only centimeter accuracy in measurement of propagation delay, and generally only incorporated *zenith* water vapor measurements. Subsequent advances in radiometry that produced resolutions of better than .5 *mm* of water vapor, coupled with evidence that large anisotropies in atmospheric water exist, indicate that GPS geodesy could be improved with water vapor measurements along the propagation path to each of the GPS satellites being utilized.

The purpose of this thesis was to develop a dual-channel radiometer system to the accuracy and resolution required to produce an enhancement in accuracy of GPS geodesy by more accurately measuring the tropospheric delay, and to determine with field experiments the level of accuracy that could be attained. This thesis describes in detail the technical and performance aspects of a dual-channel water vapor radiometer system that was developed under Department of Commerce (and later on, private) funding.

That measurement of tropospheric water vapor can improve GPS geodesy was tested in field experiments described herein. The enhancement in vertical accuracy is accomplished by direct measurement of atmospheric water vapor along the propagation path to each of the GPS satellites being observed. Ancillary to this experiment was the finding that the *difference* in water vapor burdens between GPS sites can be accurately determined from the GPS measurements alone. The latter finding is of significant interest to the meteorological and global climate communities.

Chapter 2 describes the refractive delays encountered by GPS propagation. This includes the ionosphere as well as the troposphere. All tropospheric delays are considered and compared, not just those induced by water. Both

the ionosphere and tropospheric water are highly variable and require real-time measurements to accurately model their effects; the other meteorological phenomena analyzed are found to be negligible in effect. Microwave emission in the vicinity of the 22 GHz water vapor line is also discussed. This vapor line is, of course, directly related to absorption and therefore to emission, the radiometer observable.

Chapter 3 presents the theoretical basis for microwave radiometry, and describes the methodology surrounding inference of atmospheric liquid water (cloud) and water vapor from two-channel microwave measurements. The chapter ends with a discussion of errors associated with dual channel radiometry.

Chapter 4 describes in detail the water vapor radiometers used in these experiments. The enhancements to the instruments that advanced the accuracy, resolution, and stability are described. The theoretical analyses and testing that went into the development of the WVR are discussed. WVR stability, accuracy, and intercomparison tests are discussed. The controlling software, observing scheme and corrections, and quality control algorithms are also discussed.

Chapter 5 describes the laboratory and field experiments that were undertaken, and presents the results of those experiments. Following absolute accuracy and intercomparison tests, WVR and GPS observations were made at the ends of a 50 *km* baseline between the UNAVCO (University Navstar Consortium) at Boulder and Platteville CO. In total over 600 hours of useable data were gathered during the period September through December 1992. These data fell into 26 days wherein at least 12 hours of concurrent data from all systems were collected and where Center for Orbit Determination in Europe (CODE) GPS orbits were available, and 19 days wherein Permanent Geodetic Geophysical Array (PGGA) orbits and more than 20 hours of data were available.

Chapter 6 describes improvements in the instruments and methods that are to be applied to a proposed subsequent experiment. It is hoped that better than 2 *mm* precision on the 50 *km* UNAVCO-Platteville baseline can be demonstrated.

Chapter 2 Atmospheric and ionospheric radio refractivity and absorption

In this chapter, I model all possible ionospheric and tropospheric sources of GPS propagation delay and their relative magnitudes. Current models can still suffer uncertainties in these delays as large as tens of centimeters. Because the effect of hydrometeors (rain, snow, fog, aerosol haze) can be significant when present, they are included in the following analysis. They were not considered in the field experiments performed, however, because useable data were not obtained during their presence. The ionospheric and the dry and wet tropospheric propagation delays were measured and/or modeled in all cases in the field experiment.

If GPS and VLBI propagation paths were not subjected to the uncertainties in the propagation through the temporally and spatially variable ionosphere and the troposphere, position accuracies could be greatly improved, especially from short-term (< several hours) observations and especially in the vertical dimension. At present, limitations in models of ionospheric and tropospheric refractivity and antenna multipath propagation restrict accuracy of baseline solutions. Additionally, because of ionospheric and tropospheric modeling deficiencies, observation elevation angles for GPS observations are generally limited to angles greater than 10 degrees; below this level, uncertainties in all these effects tend to increase unacceptably.

Much success has been achieved in using a *stochastic* method of estimating unmodeled delays in solving for position [Herring, 1990]. This stochastic method minimizes position error by allowing unmodeled atmospheric- tropospheric delays to be estimated during the position solution determination. The method utilizes a plane parallel medium in the model, and therefore does not, at present, consider the residual ionospheric error or spatial gradients or anisotropies in the troposphere. An inversion for a more spatially complex model of the delaying medium would not appear to be promising because the increase in the number of unknown variables of the present position solution techniques will increase process noise, and because long

observation times required to accommodate the increase in unknowns by allowing satellites to move across the sky would also permit changes to occur in the water vapor anisotropies. As an alternative, long term GPS observations tend to average out delay uncertainties, but chronic deviations from plane parallel (e.g., orographic effects, seasonal gradients) are generally not effectively removed. Furthermore, there are requirements for accurate GPS solutions from short duration observations. For instance, more accurate frequent interval solutions at fiducial sites could further improve GPS satellite orbit determination which in turn improves GPS geodesy; such solutions require a more accurate model or measurement of the delay.

Typical ranges of propagation delays, and the *error bars* suffered in presently used modeling techniques, are given in the Table below.

TABLE 2.1 Sources, Magnitudes, Uncertainties of Propagation Delay		
Delaying Medium	Typical range of magnitude (zenith)	Typical uncertainty of present models elev>15 deg
Ionosphere:	10 m (night) →50 m (day)	2 to 20 cm ⁽¹⁾
Troposphere: dry troposphere	2.35 to 2.45 m at sea level	predictable, 1 mb = 2.4 mm
water vapor	6 to 30 cm	$\left\{ \begin{array}{l} \text{stochastic, zen. : } 2\text{cm} \\ \text{anisotropies : } 2\text{cm} \end{array} \right.$
hydrometeors (cloud, rain, fog, haze)	0 to several cm	
Propagation Multipath: at receiver antenna at spacecraft antenna	0 to several cm unknown but small	removed by: averaging not removed

⁽¹⁾ Brunner et al., 1991. Note that these uncertainties are for a *single path*, to one satellite, and are in general largely removed by differencing, especially on short baselines.

Additional position uncertainty comes from the strength of the geometry of the satellites in the position solution. Propagation paths from GPS satellites to the receiver antenna are only in the upper hemisphere above the antenna site. Because of the geometry of the position solution is not constrained by observations from the lower hemisphere, the vertical dimension of the position solution suffers a greater error than the horizontal, typically about three times as great. The accuracy with which one can measure position is determined by the strength of the geometry, called *GDOP* (geometric dilution of position, the rms position error) or *PDOP* (position dilution of position, the rms radial range error). *PDOP* is inversely proportional to the volume of a polyhedron described by unit vectors from the antenna position to each of the GPS satellites, the polyhedron being defined by lines interconnecting the positions of the unit vectors (but excluding the observer point) [Spilker, 1978]. One can therefore see that, in the case of four satellites a tetrahedron is described, and the maximum strength of the GPS position solution requires one satellite overhead and the three others equally spaced around the horizon. Increased solution strength would therefore come from being able to observe to lower elevation angles.

Due to ray bending and sphericity of the atmosphere, mapping functions of the tropospheric propagation path are required in VLBI and GPS geodesy. These mapping functions do not adequately model the highly variable water and water vapor delays, nor do they adequately model the delay, ray bending, and bifurcation of the two GPS carrier frequencies due to the spatially and temporally varying ionosphere. Mapping functions are described in §3.3.1.

2.1 The delay due to the ionospheric plasma

The ionosphere lies above 99.9% of the mass of the Earth's atmosphere and between 50 and 1000 *km*. Because the sun is the primary source of free electron production, the ionosphere varies greatly with the rotation of the Earth and with solar activity. Viewed as a density contour map projected onto the surface, it roughly resembles a bullseye with the center about an hour east of the subsolar

point. The free electron population in the ionosphere is created by a complex ion production–recombination mechanism via the ionization of the tenuous upper reaches of our atmosphere by ultraviolet and more energetic radiation from the sun and cosmic sources. The losses involve recombination via an intermediate attachment of free electrons to neutral atoms and molecules. Because the neutral gas density is determined by hydrostatic equilibrium, the gas density profile is roughly exponential with altitude. Ionization rates and ionizing flux attenuation are proportional to density, and recombination to density and pressure. The ion density can therefore roughly be described as a superposition of several Chapman layers (each layer associated with an atmospheric constituent) wherein the free electron density initially increases in each layer with increasing optical depth downward into the atmosphere, peaks, and then rapidly falls off due to the attenuation of the ionizing flux and higher recombination rates.

The ionospheric profile is generally classified into the D, E, F1, and F2 regions. These various layers are predominately the product of several prominent ultraviolet lines and the Lyman continuum from solar flux, all of whose attenuation with depth into the atmosphere differ. At night, recombination and some transport processes diminish and reshape the ionospheric profile; The *E* layer diminished to a fraction of its daytime value, and the *F*₁ layer disappears.

The ionosphere is the first delay encountered by GPS radio propagation. As shown below, this delay is quite accurately modeled and measured from each GPS satellite for elevation angles above about 15 degrees and is therefore not a great source of uncertainties for measurements above this elevation. Additionally, double differencing between sites that see roughly the same ionosphere (e.g., short baselines) removes ionospheric error. Below this elevation of 15 degrees, other propagation errors such as multipath, tropospheric uncertainties, separation (bifurcation) of the *L*₂ and *L*₁ carriers, and ionospheric propagation path uncertainties become significant. There is interest and promise in accurately modeling the ionosphere at lower elevation angles to include collisions and the Earth’s magnetic field in addition to with the electronic plasma frequency [Brun-

ner and Gu, 1991]; therefore, the complete ionospheric magnetoplasma delay is defined below.

Because of the presence of the Earth's magnetic field, the ionosphere is a magnetoplasma rather than merely an electron plasma. To date, GPS technology has largely ignored the effect of the Earth's magnetic field upon delay and polarization. The plasma refractivity is due to mobility of free ions (primarily due to the less massive free electrons) under the effect of the electromagnetic wave.

The Appleton-Hartree formula [Davies, 1965; Budden, 1985] gives the complex index of refraction for *phase* in a magnetoplasma:

$$n_{phase,complex}^2 = 1 - \frac{R_p^2}{1 - iR_c - \frac{R_H^2 \sin^2 \theta}{2(1 - R_p^2 - iR_c)} \pm \left[\frac{R_H^4 \sin^4 \theta}{4(1 - R_p^2 - iR_c)^2} \right]^{1/2} + R_H^2 \cos^2 \theta} \quad (2.1)$$

where I have abbreviated the ratios:

$R_p = \frac{f_p}{f}$ = electronic plasma to carrier frequency,

$R_H = \frac{f_H}{f}$ = gyromagnetic to carrier frequency,

$R_c = \frac{f_c}{f}$ = ion collision to carrier frequency, and where

f is the carrier frequency,

and θ is the angle between the magnetic field and the Poynting vector for the propagation.

For 0.5 gauss (typical Earth's magnetic field at ionosphere altitudes), f_H is 1.42 MHz, or $R_H \simeq 10^{-3}$. The electronic plasma frequency ranges of the ionosphere varies from about 2 MHz when and where the ionization rate is low, to about 20 MHz during high solar activity ($R_p \sim 1.5 \times 10^{-3}$ to 10^{-2}). The collision frequency ranges from $10^5/sec$ in the D layer to less than $10^3/sec$ in the other layers ($R_c \sim 10^{-6}$ to 10^{-4}). GPS frequencies are greater than collision frequencies by 4 orders of magnitude. We can therefore ignore collisions. Ratio-

nalizing the above formula for the real component (while ignoring collisions) we obtain:

$$n_{phase,real}^2 = 1 - \frac{2R_p^2(1 - R_p^2)}{2(1 - R_p^2) - R_H^2 \sin^2 \theta \pm \sqrt{R_H^4 \sin^4 \theta + 4(1 - R_p^2)^2 R_H^2 \cos^2 \theta}} \quad (2.2)$$

Clearly the plasma frequency dominates over the gyromagnetic frequency. It has been the practice in GPS geodesy, therefore, to ignore the Earth's magnetic field. Under this assumption, the above expression for radio propagation velocity through a plasma can be approximated by the following expression [Jackson, 1975]:

$$n_{phase}^2 = 1 - \left(\frac{f_p}{f}\right)^2 = 1 - \left(\frac{N_e e^2}{\pi m_e}\right) \left(\frac{1}{f^2}\right) \quad (2.3)$$

That the phase index of refraction is less than unity implies that carrier phase velocity exceeds the speed of light, but does not violate relativity; energy and information of the GPS signal are carried at the group velocity, which is $\leq c$.

Ignoring collisions, the group index of refraction for dispersion is related to phase index of refraction by:

$$\begin{aligned} n_{group}^2 &= \frac{1}{n_{phase}^2} \\ &= 1 + \frac{2R_p^2(1 - R_p^2)}{2(1 - R_p^2)^2 - R_H^2 \sin^2 \theta \pm \sqrt{R_H^4 \sin^4 \theta + 4(1 - R_p^2)^2 R_H^2 \cos^2 \theta}} \end{aligned} \quad (2.4)$$

and, with a binomial expansion,

$$n_{group} \simeq 1 + \frac{R_p^2(1 - R_p^2)}{2(1 - R_p^2)^2 - R_H^2 \sin^2 \theta \pm \sqrt{R_H^4 \sin^4 \theta + 4(1 - R_p^2)^2 R_H^2 \cos^2 \theta}} \quad (2.5)$$

for the magnetoplasma, but ignoring collisions. Or, ignoring the Earth's magnetic field,

$$n_{group} = 1 + \left(\frac{f_p}{f}\right)^2 \quad (2.6)$$

Because the ionosphere is dispersive, the ionospheric group delays can be determined (within the accuracy of the above approximate equation) with a dual-frequency GPS receiver by measuring the offset in the two GPS carrier phases (properly frequency divided). Both the L_1 (1.575 GHz) and the L_2 (1.227 GHz) carriers are generated by multiplying up from a reference of 10.23 MHz (10.23×154 and 10.23×120).

Because the atmospheric index of refraction is very nearly unity, it is convention to define *refractivity*, N , as parts per million difference from unity:

$$N = (n - 1) \times 10^6 \quad (2.7)$$

The plasma refractivity is therefore:

$$N \cong \left(\frac{f_p}{f}\right)^2 \times 10^6 \simeq \frac{4.03 \times 10^{-5} n_e}{f^2} \quad (2.8)$$

where f is in MHz . Under the assumptions of this approximation, we can write what is called the L_3 linear combination, free of the ionospheric plasma dispersive delay:

$$\Phi_{L_3,corrected} = 2.545\Phi_{L_1,measured} - 1.984\Phi_{L_2,measured} \quad (2.9)$$

where Φ_{L_i} is the total phase in cycles of each of the carriers. This expression is based on ignoring the gyromagnetic and collision frequencies of the ionospheric plasma.

Radio propagation through the plasma from near zenith at the two carrier frequencies travels through less plasma, and does not bifurcate appreciably because it is aligned with the plasma gradient. The delay is therefore quite accurately evaluated with this expression (within the assumptions that the ionosphere has no imposed magnetic field and is collisionless).

The above approximation to the Appleton-Hartree formula, along with unmodeled plasma gradient-induced ray curvature and unmodeled dual frequency birefringence induced by the Earth's magnetic field, will result in errors in the calculated ionospheric delay at low elevation angles and/or high plasma values. A more comprehensive model, including the above deficiencies, is developed by Gu and Brunner [1990] and Brunner and Gu [1991]. Their improved model is reported to diminish ionospheric model errors from 33 to 0.2 *mm* at 15 degree elevation angle and for high solar activity (zenith TEC of 1.4×10^{18}), and from 200 to 0.1 *mm* for extreme solar activity (TEC of 4.5×10^{18}).

An additional frequency of known phase relationship to L_1 and L_2 would enable much more accurate modeling of the ionosphere by utilizing a three-term nonlinear combination that would remove most of the bending and bifurcation effects, and thus allow observations at lower elevation angles. In addition to the increased PDOP, a larger number of GPS satellites could be used at any given time for a greater geometric strength of position solution. There exists a third frequency being transmitted from the GPS satellites at 1.381 GHz, but it has a strictly military function at this time, and little is known about the characteristics of this transmission. There are two other continuous emissions from the satellite vehicles that may be useable, one at 2.2 GHz (S-band) and a transponder at 8.5 GHz (X-band). No commercial receivers are currently available that are capable of receiving these frequencies.

2.2 Atmospheric refractive radio phase path delays

In addition to the radio delays induced by the ionospheric plasma, there are delays caused by several atmospheric effects. When such delays cannot be accurately measured or modeled, they result in error in the GPS position solution.

These delays are due to refractivity of and scattering by gases and hydrometeors. In dry air, refractivity is proportional to air mass in the propagation

path and is therefore predictable from atmospheric pressure; in the presence of water vapor cloud, rain, snow, or hygroscopic aerosol, refractivity can be modeled with the aid of additional measurements. Refractivity can be separated into nondispersive and dispersive components; the nondispersive component is real and is due to permittivity and permeability, while the dispersive component is complex and is due to interactions with line resonances in the vicinity of the propagation carrier frequency. The GPS carrier frequencies are far-wing (the atmospheric lines are far removed), and consequently are little affected by line resonances. It will be shown later that, at GPS carrier frequencies, the complex component of refractivity can be ignored as a delay factor. The total refractivity can be written as a linear sum of the above components:

$$N = N_0 + N'(f) + iN''(f) \quad (2.10)$$

where:

N_0 is the nondispersive refractivity, due to dielectric properties;

$N'(f)$ is the real part of the complex dispersive component;

$N''(f)$ is the imaginary part of dispersion.

The real part is conservative, whereas the imaginary part is attenuation as is shown below:

$$\begin{pmatrix} E \\ H \end{pmatrix} = \begin{pmatrix} E_0 \\ H_0 \end{pmatrix} e^{i(n\vec{k}\cdot\vec{x}-\omega t)} \quad (2.11)$$

where $\vec{k} = \frac{\omega}{c}$ is the *in vacuo* wave number. We can write:

$$\begin{pmatrix} E \\ H \end{pmatrix} = \begin{pmatrix} E_0 \\ H_0 \end{pmatrix} e^{-N''\vec{k}\cdot\vec{x}} e^{i((1+N_0+N')\vec{k}\cdot\vec{x}-\omega t)} \quad (2.12)$$

The first exponential factor $e^{-N''\vec{k}\cdot\vec{x}}$ is amplitude decay, whereas the second exponential factor $e^{i((1+N_0+N')\vec{k}\cdot\vec{x}-\omega t)}$ is harmonic. It should be noted that the radio delay is due to the real part of refractivity, whereas absorption (and consequently microwave emission, the WVR observable) is due to the imaginary part. GPS carrier phase delays are therefore delayed by the real part, whereas

the water and water vapor that induces the (refractive and scattering) delays are detected and quantified radiometrically by their absorption properties (the imaginary part).

Both polar atmospheric gases and the suspended hydrometeors and other particulate matter contribute to nondispersive atmospheric refractivity. In bulk water (cloud droplets, rain, snow, haze) refractivity is due to displacement of charge in the dielectric medium. In atmospheric gases the refractivity is due to displacement of the charge distribution of the constituents of the gas, and additionally, to alignment of polar molecules with the propagated electric and magnetic fields. Electrically polar molecules of major constituency include CO_2 , water vapor, oxides of nitrogen, and many chlorine and organic compounds. With the exception of water vapor and to a much lesser extent CO_2 , the partial pressure of the major polar molecules is essentially constant. The only molecule of import that has a magnetic moment is oxygen; this is due to 9 of the 16 electrons being spin-aligned in the same direction, and resulting in a net spin moment of the quantum mechanical projection of two Bohr magnetons. This net moment couples with the angular momentum vector of the molecule.

The atmospheric refractivity at radio frequencies can be written empirically as the sum of the refractivity due to the dry atmospheric gases plus that due to water vapor:

$$\begin{aligned}
 N &= N_{dry} + N_{vapor} \\
 &= k_1 \frac{P_{dry}}{T} + k_2 \frac{P_{vapor}}{T} + k_3 \frac{P_{vapor}}{T^2} \\
 &= k_1 R_d \rho + k_2 R_v \rho + k_3 R_v \frac{\rho}{T}
 \end{aligned}$$

or:

$$N = k'_1 \rho_{dry} + k'_2 \rho_{vapor} + k'_3 \frac{\rho_{vapor}}{T} \quad (2.13)$$

where the primed constants indicate that the gas constants have been absorbed into the coefficients. $R_d = 2.87 \times 10^6 \text{ cm}^2/\text{sec}^2 \text{ K}$. The vapor gas constant is

$R_v = R_d \frac{M_d}{M_v}$ where $M_d = 28.964g/g\text{-mole}$ and $M_v = 18.015g/g\text{-mole}$ are the gram molecular weights. The generally accepted values of the coefficients are [Bevis et al., 1993]: $k_1 = 77.60 \pm 0.05K/mb$, $k_2 = 70.4 \pm 2.2K/mb$, $k_3 = 3.739 \pm 0.012 \times 10^5 K^2/mb$. The “ k_1 ” and “ k_2 ” terms are due to the polarizability of the gas atoms and molecules by displacement of the electron clouds, whereas the “ k_3 ” term is due to the orientation of the electric dipole moment water molecules by the electric vector of the radio propagation. The “ k_3 ” term dominates the “ k_2 ” term by about a factor of 20.

In the following sections, the tropospheric delays are conveniently separated into those due to the dry (without water or water vapor) delay, water vapor delay, and the delays due to various forms of hydrometeors and particulates.

2.2.1 Phase path refractive delay due to the “dry” atmosphere

By far the largest tropospheric delay is due to the dry atmosphere. This delay is also accurately modeled and is directly proportional to atmospheric pressure. It is therefore not a source of significant GPS position error when the barometric pressure is accurately measured.

As mentioned in the section above, the refractivity of the atmospheric constituency is due to displacement of the charge distribution of molecules, and to polar molecules. The relative concentrations of the various gases of the dry atmosphere are quite constant and predictable, and their total concentrations are measurable by the total mass of the atmosphere. Because the refractivity of water vapor due to electron cloud displacement is of the same form and magnitude, and because it contributes to the total pressure and mass of the atmosphere and is therefore part of the barometric measurement, it is generally included in the *dry refractivity*. The polar refractivity of water vapor due to its electric dipole moment is much larger and is considered separately. The newly defined “dry” refractivity is therefore proportional to atmospheric density (usually expressed as *pressure(mb)/temperature* to eliminate mixing ratios):

$$\begin{aligned}
N_{dry} &= 77.6 \frac{P_d}{T} \\
N_{\text{"dry"}} &= 77.6 \frac{P_d + e}{T} = 77.6 \frac{P_{tot}}{T}
\end{aligned} \tag{2.14}$$

The utility of this definition of “dry” will now come apparent. Using the Perfect Gas Law and integrating vertically through the atmosphere we can obtain for the total zenith dry refractivity:

$$\begin{aligned}
\text{total zenith “dry” delay} &= 77.6 \int_0^\infty \frac{P_{tot}}{T} dh = 77.6 \frac{RP_{surface}}{\bar{m}} \\
\text{total zenith “dry” delay} &= 0.00228P_{surface}
\end{aligned} \tag{2.15}$$

where R is the gas constant and \bar{m} is the mean molecular weight of the atmosphere. A barometric measurement therefore defines the integrated zenith delay of the “dry” atmosphere by measuring the mass of the atmosphere; the delay is directly proportional to barometer. This delay is about 2.35 meters at sea level in the zenith direction. The hydrostatic delay can be refined to include variations due to those of local gravity [Johansson et al., 1993]:

$$\text{total zenith “dry” delay} = \frac{0.0022768P_{surface}}{(1 - 0.00266\cos 2\Phi - 0.00028H)} \tag{2.16}$$

where Φ is the latitude and H is the height of the station in km above the geoid.

2.2.2 Water vapor: general atmospheric distribution

The most variable component of atmospheric radio phase delay is water in its three phases. It is discussed in general terms below; the physical properties of vapor, liquid, and ice, as they specifically relate to geodesy and radiometry, will each be subsequently discussed.

The Earth is unique among the solar planets because of its abundance of water and water vapor. This, coupled with a suitable flux of solar energy, gives

a terrestrial climate suitable for life based on water and carbon chemistry. The large heat of fusion and heat of vaporization of water buffer daily and seasonal temperature swings that occur because of the planetary rotation and the nonorthogonality of the Earth's spin axis to the plane of the ecliptic. This buffering is augmented by the mobility of water and by the relatively high specific heat capacity of water that enables the oceans to absorb and release vast amounts of heat without much temperature change. Additionally, atmospheric water vapor, the most significant and most variable of the greenhouse gases, has a tremendous ability to trap infrared heat that would otherwise be lost to space. Water vapor induces about 30C warming due to longwave trapping, and is therefore an order of magnitude more significant than second ranking CO_2 [Turco, 1992].

The highly nonlinear Clausius-Clapeyron equation for saturation water vapor pressure e_s over water reflects the atmosphere's ability to hold water as a function of temperature:

$$\frac{de_s(T)}{dT} = \frac{m_v L_c e_s(T)}{RT^2} \quad (2.17)$$

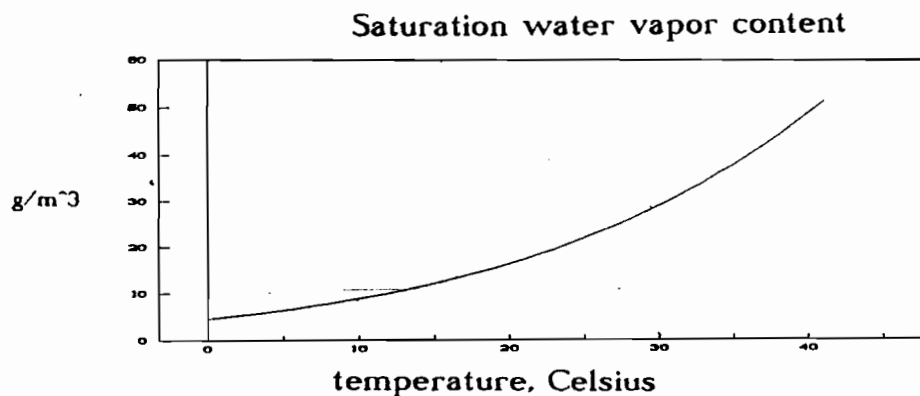


FIGURE 2.1 Saturation water vapor density over water as a function of temperature.

Increases in air temperature over water will increase water intake of the atmosphere; increases over absolute desert will not. The partial pressure of

water vapor, and therefore the ability of the atmosphere to hold water vapor, is a positive nonlinear function of atmospheric temperature; the resultant feedback mechanism tends to amplify increases in global atmospheric temperatures (see figure 2.1). The scientific jury is still out on whether countervailing mechanisms (increased albedo due to cloud, buffering mechanisms) limit this amplification, and therefore global warming.

In the context of relevance to global change, a 2K increase in temperature results in about a 10% increase in the saturation vapor pressure. The equilibrium vapor pressure increases exponentially with increasing temperature; thus the significance of small increases in global temperatures. An increase in water vapor mass does not necessarily directly follow an increase in temperature, however. The water source must be present.

Water vapor distribution in the troposphere is dependent upon many static and dynamic effects. These include vapor sources and sinks, mixing processes driven by flow on all scales, heating and cooling, phase changes, and hydrostatic forces. The dynamically-driven distribution is perhaps most easily described as a chaotic field of eddy mixing imbedded in large scale flow fields, and is therefore not amenable to simple modelling, but rather requires a number of measurements of fields of flow, turbulence, and state parameters. The outer scale of this dynamic distribution starts with large scale effects such as large scale flow fields, an orographic barrier, or a cumulus cloud (scale of many kilometers), moves into the scale of eddy motions of less than 1 *km* and then cascades down by eddy diffusion to centimeter scales where viscous processes dissipate the energy of motion into heat. The distribution of wavelengths in these eddy fields follow the *5/3 law*: $E(k) \propto k^{-5/3}$ where $k = 2\pi/\lambda$, the wave number. These eddy sizes, coupled with their motions, define the high frequency temporal and spatial variations in atmospheric refractivity.

Except for an insignificant contribution from ice-laden meteors and some trace oxidation of methane and other hydrocarbons in the stratosphere, the source of water vapor is at the surface. The major surface source is oceanic. A

primary mechanism for transport of water vapor to higher altitudes is buoyancy started by surface solar heating, orographic or frontal lofting, or convergence. This lifting is often augmented by release of latent heat of vaporization (and heat of fusion if freezing is involved in the precipitation process) in the formation of clouds. Such is the mechanism of cumulus build-up. Healthy cumulus clouds (those with sufficient water vapor, and rising through an adequate temperature lapse rate) can reach the tropopause, thereby bringing water (ice) to as high as 20 *km*. Surrounding cumulus build-up is general subsidence of drier air from aloft, some of which is entrained back into cloud growth, evaporating liquid water within the cloud and diminishing buoyancy, and some of which reaches the surface to replace lofted air.

Such processes, coupled with eddy mixing, gaseous diffusion, and precipitation mechanisms, establish a vertical water vapor distribution with a highly variable scale height generally roughly approximated at 2 *km* (the Bernese GPS software used herein uses 1.6 *km*). Were it not for the dynamic processes in the atmosphere that flux water within all of its phases, diffusional processes would establish the water vapor scale height at about 12 *km*. Thus the sinks, the precipitation processes, play a significant role in water vapor distribution. See, for instance, J.T. Kiehl [1992]. The average global precipitable water vapor is about 2 g/cm^2 (about 13 *cm* of zenith delay).

2.2.3 Phase path refractive delay due to water vapor

The second largest contributor to tropospheric delay (after the predictable delay due to the dry atmosphere) is water vapor. It is also the most highly variable component of tropospheric delay. This delay must be corrected for in precise GPS geodesy. The delay is due to the polar nature of water molecules; the electric dipole moment of water vapor is due to the great affinity of oxygen for electrons to complete the 2p shell, inducing an asymmetry in the electron cloud. These dipoles are oscillated by electromagnetic waves. The refractivity of water vapor is expressible as [Thayer, 1974; Bevis, et al., 1993]:

$$N_{vap} = 64.8 \frac{P_{vap}}{T} + 3.776 \times 10^5 \frac{P_{vap}}{T^2} = 64.8 \frac{\rho_{vap} R}{m_{vap}} + 3.776 \times 10^5 \frac{\rho_{vap} R}{m_{vap} T} \quad (2.18)$$

where R is the gas constant and m_{vap} is the gram molecular weight of water. The first term is due to electron cloud displacement and was assimilated into the dry atmospheric pressure term in equation 2.15. The second term in this expression, the refractivity due to the polar nature of water vapor, dominates the first by about a factor of 20.

Recall that the water vapor radiometer measures emission by water vapor, which is proportional to local temperature (emission from an altitude h $I_{vap}(h) \propto \rho_{vap}(h) \cdot T(h)$), whereas the refractivity due to water vapor has an inverse relationship to temperature. The radiometer measurement is, therefore, not a direct measurement unless the temperature regime is known. Statistically, however, radiometric retrievals have proven to be quite accurate (to within several millimeters of water vapor), presumably because the water vapor population tends to lie in the lowest levels of the atmosphere and at rather consistent temperatures. The microwave emission of water vapor is therefore statistically predictable.

2.2.4 Phase refractive delay due to non-gaseous tropospheric constituents

The most significant sources of error in GPS geodesy are propagation multipath and tropospheric delays. Multipath errors are being diminished by antenna design and placement and software algorithms. The propagation delay due to water vapor has been the subject of much analysis. Line shape and intensity models of the permittive atmospheric components have evolved and been improved [Becker and Autler, 1946; Gross, 1955; Waters, 1976; Keihm, 1991; Liebe, 1983, 1985, 1987, 1989a,b, 1991, 1992, 1993], thereby facilitating accurate atmospheric measurement by water vapor radiometers. Stochastic estimation and direct measurement of water vapor have improved GPS positioning accuracy to

the sub-centimeter level under some circumstances. Because of the successes in diminishing uncertainties due to water vapor and other sources of error, a previously unaddressed source of error is now surfacing. This is the delay due to liquid and ice phase water (when present) of the air.

1) Phase delay due to cloud, rain, fog, and haze

While the delay from water vapor is due to the polar nature of the water molecule and therefore to permittivity, the phase delay due to liquid water, ice and aerosol particles is due to the permittivity of bulk (liquid) water, and to a much lesser extent, to Rayleigh scattering. Compared to the delays due to the very predictable “dry” troposphere and to water vapor, this delay is the most difficult to characterize and estimate because of the high spatial and temporal variability of hydrometeors.

Water vapor in clear air can be accurately measured with a single channel radiometer operating in the vicinity of the 22.235 GHz water vapor resonance. This is because the emission spectrum is essentially due only to the (predictable) contribution of oxygen and to water vapor. In an effort to measure water vapor in the presence of cloud as well as in clear air, a second channel is incorporated into water vapor radiometers. This channel is generally located around 31 GHz. Water vapor dominates the 22 GHz contribution, while liquid water dominates at 31 GHz; applying a little algebra to measurements at both frequencies will separate the vapor and the liquid signals (see Figure 3.3).

For local thermodynamic equilibrium (LTE) wherein collisional processes dominate radiative, valid to about 100 km for the microwave region, absorption varies as the volume of water droplets. Therefore, absorption (and by Kirchoff’s Law, emission) is independent of the droplet distribution, and the total integrated liquid water along a propagation path is directly related to attenuation.

By the Clausius-Mossotti equation, dielectric refractivity is proportional to the total mass of the water along the propagation path and is independent of the shape of the water droplet or ice particle (see, for instance, Born and Wolf,

1980; Jackson, 1975). For the refractivity of liquid water we can thus write:

$$N_{rain} = W \frac{3}{2} \left[\frac{\epsilon_0 - 1}{\epsilon_0 + 2} \right] \quad (2.19)$$

where W is the columnar mass, or total mass per unit area, of bulk water along the propagation path and ϵ_0 is the permittivity.

So the delay due to liquid water can be directly measured with dual-frequency radiometer, and this measurement of liquid water directly relates to nonresonant refractivity. The WVR therefore precludes the need for estimation of rainfall rates and extents, but we shall give examples of rainfall rates and resultant delays at the end of this chapter to give the reader a qualitative feel for the magnitude of delays incurred in various precipitation scenarios.

The permittivity ϵ_0 of water is a slight inverse function of temperature. Liquid water exists over a range of atmospheric temperatures (- 15C to +50C), and the permittivity for liquid water consequently varies from about 92 to 74. But since it dominates in both the numerator and the denominator in the following expression, we can approximate to within 1%:

$$N_{cloud} = W \frac{3}{2\rho_w} \frac{\epsilon_0 - 1}{\epsilon_0 + 2} \simeq 1.45W \quad (2.20)$$

where:

$\epsilon_0 = 77.66 + 103.3(\theta - 1)$, where $\theta = 300/T$ is the inverse temperature [Liebe 1989a],

ρ_w is the density of water ($\simeq 1$),

and W is the columnar liquid state water content in mm .

The subscript *cloud* is used to describe all forms of suspended liquid water droplets: cloud, fog, haze. Recall that the refractivity N is the deviation from the *in vacuo* value of propagation in *ppm*. A convenient scale for N for cloud, whose dimensions are on the order of kilometers, is mm/km . And a concentration of $1 g/m^3$ for a distance of $1 km$ is an integrated columnar liquid value of $1 mm$.

So a 1 g/m^3 cloud of thickness of 1 km has a vertical columnar liquid water burden of 1 mm and would induce a zenith path delay of 1.5 mm .

To estimate the magnitude of the *complex* refractivity, we calculate it for cloud. For frequencies below 100 GHz , the *single Debye relaxation* formulation for the complex permittivity of water is sufficient [Liebe et al., 1991b]. Rationalizing the Van De Hulst expression, the real part of the complex refractivity is:

$$N'_{cloud} = \frac{9}{2}W \left(\frac{1}{\epsilon_0 + 2} - \frac{\eta}{\epsilon''(1 + \eta^2)} \right) \quad (2.21)$$

$$N'_{cloud} \simeq .0004W \text{ at } 1.228\text{GHz} \quad (2.22)$$

$$N'_{cloud} \simeq .0006W \text{ at } 1.575\text{GHz} \quad (2.23)$$

where:

$$\eta = \frac{2+\epsilon'}{\epsilon''}$$

$$\epsilon_0 = 77.66 + 103.3(\theta - 1)$$

ϵ' is the real (refractive) part of permittivity;

ϵ'' is the imaginary (absorptive) part of permittivity;

θ is the inverse temperature parameter, $\frac{300}{T(K)}$.

The primes indicate the real component, double prime is the imaginary component. As can be seen, the complex (dispersive) part of refractivity is more than three orders of magnitude down from the nondispersive part, and will therefore be ignored in all phase delay analysis herein.

2) Phase delay due to snow, glaciated clouds

Snow, ice fog, and glaciated cloud are not detected by conventional water vapor radiometers because absorption (the imaginary part of dielectric coefficient) for ice is small. Ice phase of water has therefore been treated separately here. The refractivity is [Liebe, et al., 1989b]:

$$N_{ice} = W_{ice} \frac{3}{2\rho_{ice}} \frac{\epsilon_{ice} - 1}{\epsilon_{ice} + 2} \simeq 1.58W_{ice} \quad (2.24)$$

where:

W_{ice} is the concentration of snow, ice in g/m^3 ;

$$\rho_{ice} = .916g/m^3$$

$$\epsilon_{ice} = 81.8 + 96(\theta - 1) \text{ [Hufford, 1991]}$$

To estimate the expected magnitude of this delay, we estimate the concentration of water in a heavy snowstorm of $5cm/hour$. Flakes in such a storm have a fall velocity at sea level of about 1 to $1.5m/sec$ [Oguchi, 1983] and melt to about $1mm$ of water per cm of snow. This yields a moisture content of $1g/m^3$ of water, resulting in a delay of $1.5mm/km$ of snow. A light snow yields about $0.2g/m^3$ and a delay of $0.3mm/km$. It is interesting to note that many ice habitats grow via vapor diffusion rather than accretion of liquid water, and therefore may actually diminish the water vapor content of the cloud.

It is important to note that much of the atmospheric moisture at altitudes higher than the $0C$ isotherm is ice. Liquid water seldom exists at temperatures colder than $-10C$ except in very small droplets. Therefore, even though a precipitation event may be manifested as rain, there may be ice high in the cloud. This ice phase is not detectable by a WVR, and may be as dense as several g/m^3 .

Cirrus clouds occur frequently, but seldom contain more than $0.001g/m^3$ in ice phase [Liebe et al., 1989a]. They are generally of limited vertical extent ($0.5km$), and therefore contribute delays of less than $0.1mm$ of path delay.

3) The radio propagation delay due to scattering

The propagation retardation due to scattering effects falls into the Mie regime. The Rayleigh scattering approximation criterion that $\lambda > diameter$ of atmospheric hydrometeors is valid up to about 100 GHz for atmospheric scatterers. A second Rayleigh criterion, that the imaginary (absorptive) part of the refractive index be small, is not satisfied across this frequency range, however, and limits the validity of the Rayleigh approximation to about 3 GHz [Ippolito, 1989]. Rayleigh scattering varies slightly greater than $\frac{1}{\lambda^4}$, and as $radius^6$ (or

*volume*²). So, for a given atmospheric water content, scattering is favored by a distribution of large droplets rather than the same quantity of water in a small droplet distribution. But the refractivity due to scattering is small relative to that due to polarizability.

Cloud, fog, and rain droplets are approximately spherical up to 1.5 *mm* in diameter, and trend toward oblate spheroids in the larger diameters [Oguchi, 1983; Pruppacher and Pittner, 1971]. Large droplets are in the tail of a rapidly diminishing distribution, however (see, for instance, the Marshall- Palmer drop size distribution). Additionally, delays due to scattering from rain and snow are several orders of magnitude smaller than those due to water vapor, so uncertainties in the rain model have a small effect upon the representativeness of the integrated delay model.

4) Phase delay due to aerosols

The hygroscopic aerosols are active depending upon the level of relative humidity. Provided that the condensation nucleus of the aerosol does not effect the permittivity of the aerosol droplet as a solute, the radio phase delay of aerosols is, like other liquid phase droplets, proportional to the bulk concentration of water and is therefore directly measured with a dual- channel WVR. Such aerosols tend to lie in the boundary layer, and therefore generally involve only several hundred meters of propagation path length. Additionally, normal concentrations are $\leq 0.1 \text{ g/m}^3$ [Liebe, 1989a]. Aerosols therefore induce path delays of less than 0.1 *mm*, even if any contained solute (e.g., salt) drastically increases the permittivity, and can therefore be ignored.

Sandstorms are of concern to satellite telemetry, and were therefore included in this survey. They are frequent in some locations, and nonexistent over most of the world. They can be a significant contributor to carrier depolarization, but are not a significant contributor to phase delay. Silicates have a permittivity of about 4, about 1/20th that of water. A significant sandstorm lofts densities up to about 10^{-5} g/m^3 , for a refractivity per *km* of:

$$N_{sand} \sim 0.7 \times 10^{-5} / km \quad (2.25)$$

2.2.5 Summary of atmospheric refractivity

TABLE 2.2 Typical Particle Sizes, Delays, Occurrences				
Meteorolog. Phenomenon	Range of Droplet Dia.	Conc. g/m^3	Propagation Delay ⁽¹⁾ mm/km	⁽²⁾ Frequency of occurrence
vapor (RH)	molecular	1 to 20	5 to 40cm	continuous
cloud	1 to 50 μ	0.05 to 5	.08 to 7	1 to 10%+
fog	0.1 to 5 μ <i>2-50μ</i>	0.1 <i>-0.01 to 0.4</i>	0.1	<i>Silverman, in Wx & Climate Mar 1989</i>
haze	0.01 to 1 μ	0.01 <i>Ippolito 1989</i>	0.01	
rain:	in mm:			
{ drizzle	{ 0.2 - 0.7	{ 0.1	{ 0.15	{ 2%
{ steady	{ 0.5 - 0.8	(3) { 0.3	{ 0.5	{ 0.5%
{ heavy	{ 0.7 - 1.3	{ 0.7	{ 1	{ 0.07%
{ downpour	{ 0.8 - 1.7	{ 3+	{ 4.5+	{ 0.001%
snow †	to 1cm	0.1 to 1.0	.2 to 1.5	0.1%
hygroscopic aerosol	< 10 μ	≤ 0.1	< 0.1	bndry layer < ~ 0.3km
sand, dust †		10 ⁻⁵	.7 $\times 10^{-5}$	

† Not detectable with conventional dual-frequency water vapor radiometer.

(1) Water vapor delays are total zenith values. All other delays are per km of cloud depth.

(2) Percent of time during 4-season year, typical mid-latitude location.

(3) From Zuffrey, 1972.

Table 2.2 gives perspective on the magnitude of delays due to various meteorological occurrences, and the frequency of their occurrence. Most delays

are given per *km* because of the variability of meteorological events. These delays need to be applied to the length of the propagation path; for example, a propagation path through steady rain of vertical depth 2 *km* and at 15 degrees elevation angle will incur a delay of 4 *mm* due to the rain alone. The radiometer will have measured 2.7 *mm* of liquid water. This rain delay does not include any cloud within which the rain might be contained; it is in addition to cloud delay. A propagation path through a cloud layer 3 *km* thick and at an elevation angle of 30 degrees could incur a delay of up to 4 *cm*. The vapor induced delay along such a path might be 40 *cm*, so cloud delays can be significant relative to the vapor delay.

We have shown that meteorological events can induce significant delays in propagation. All of these events (rain, fog, haze, cloud) except ice phase of water and nonhygroscopic aerosols are detectable by standard water vapor radiometers, and the delay is directly quantifiable. The dual channel water vapor radiometer directly infers liquid water along its sight path, and the resultant radio delay is:

$$\text{Propagation delay} = 1.45 \times \text{measured water burden} \quad (2.26)$$

Rain may degrade WVR data because of water on window. Ice phase is not detectable at millimeter wave frequencies.

The measurement of phase path delay due to water vapor is not so straightforward because of the temperature dependence of refractivity. The radiometric method of measuring the vapor delay is discussed in the following chapter.

2.3 Atmospheric water vapor and oxygen absorption

The discussion in the first part of this chapter described ionospheric and atmospheric refractive delay (the real part of the refractive index), important to GPS geodesy. The imaginary part, absorption of propagation by water vapor and liquid water, is significant to water vapor radiometry because the radiometer observable, emission, is equal to absorption in steady state circumstances (and

roughly proportional to temperature). The radiometer infers liquid water and water vapor content by their absorptive properties, and this content is in turn utilized to calculate propagation delay from the refractive property.

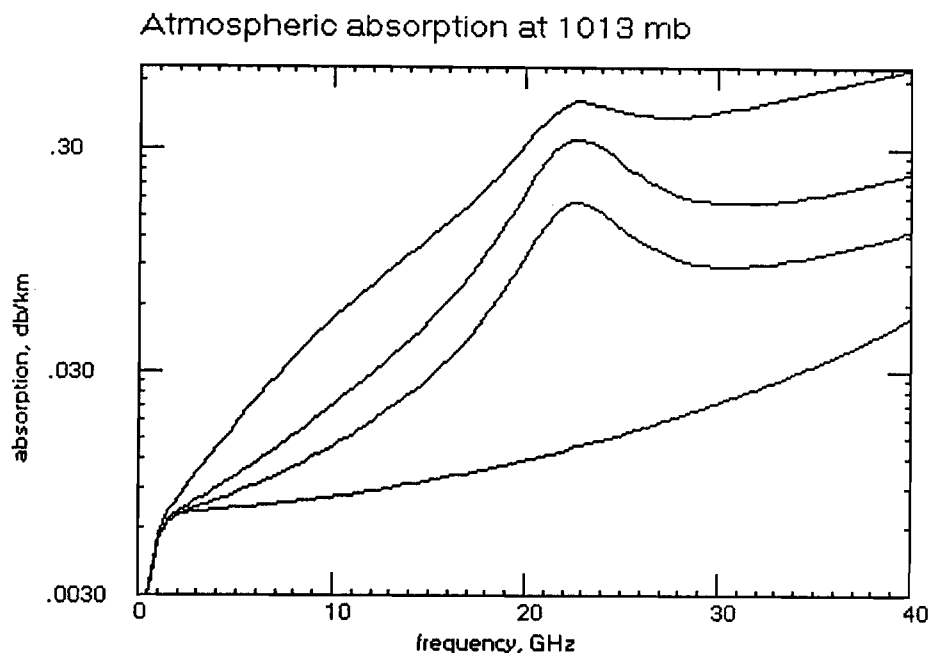


FIGURE 2.2 The atmospheric absorption spectrum between 0 and 40 GHz at standard pressure and at +15C. From the bottom, (1) the traces are for 0% RH (the underlying oxygen contribution), (2) 50% RH, (3) 100% RH, and (4) 100% RH and 0.5 g/m^3 cloud liquid. The line at 22 GHz is due to water vapor; the cloud liquid contributes as frequency^2 .

Emission of K band microwave energy in the atmosphere is due to several species of polar molecules. Although the atmosphere contains many polar gases (CO_2 , NH_3 , NO_x , chlorine compounds, and others), only water vapor and oxygen are present in enough quantity to significantly emit at millimeter wavelengths.

In the case of oxygen, the dipole is magnetic, due to 9 of the 16 electrons being spin-aligned in the same direction, and resulting in a net spin moment of the quantum mechanical projection of two Bohr magnetons that couples with

EM propagation. The electric dipole moment of water vapor is due to the great affinity of oxygen for electrons of the two hydrogen atoms, inducing an asymmetry in the electron cloud. In the case of water vapor, the dipole transition that is detected by the K-band radiometer is the electronic $6_{-5} \rightarrow 5_{-1}$ transition at 22.235 GHz.

In free space, the \vec{E} and \vec{M} components of an electromagnetic wave are equal in magnitude. The dot product of \vec{E} with typical Debye polar moments is several orders of magnitude larger than the inner product of \vec{M} and the Bohr magneton; however, the oxygen resonance in the atmosphere is roughly of the same magnitude of that of water vapor because of the relative abundances (17% for oxygen, and a maximum of about 4% for water vapor). Additionally, the oxygen resonance centered at $\lambda = 0.5\text{cm}$ is actually an assemblage of a large number of lines, with roughly 40 lines being significant absorbers.

Chapter 3 Microwave Radiometers and Water Vapor Measurements

Microwave radiometers are being increasingly utilized to remotely measure atmospheric parameters on an operational basis. The accuracies of ground-based instruments are rivaling those of balloon soundings. Unlike balloons, radiometers furnish continuous and unattended measurements. Both satellite-borne and ground-based radiometers currently measure temperature profiles to better than 1.5C, water vapor content to within about 2mm of precipitable water vapor, vapor profiles to better than 10%, and liquid water (cloud liquid) to an accuracy of about 5mm. These accuracies are expected to improve with improved line shape models and more advanced instruments. Ground-based systems are comparable in cost to the yearly operating cost of a radiosonde balloon (RAOB) release site.

3.1 The basis for microwave remote sensing of water vapor; partial linearization of the Radiative Transfer Equation

Microwave radiometric receivers measure electromagnetic noise power collected by the radiometer antenna. This received energy originates in the acceleration of free charged particles, or in the quantum mechanical energy level transitions of atomic nuclei (typified by gamma rays), electronic orbits of atoms (typified by visible light), and molecules (typified by microwaves). In the case of microwaves, the radiation can originate in the vibrational and rotational transitions of molecules. The spectral distribution of blackbody radiation from matter is embodied in Planck's Law [Jackson, 1975]:

$$I(\lambda, T) = \frac{2\pi hc^2}{\lambda^5 [e^{hc/\lambda kT} - 1]} \quad (3.1)$$

where: I is radiated power per wavelength interval, h = Planck's constant, k is Boltzmann's constant, T is temperature, c is speed of light.

This relationship was derived by Planck from first principles, under the assumption that energy is quantized; that harmonic oscillators have discrete levels of energy. Quantum mechanics, with all of its insights into nature, essentially embarked from this derivation. In the long wavelength limit, one can expand the exponential in the denominator of Planck's Law and obtain the classical Rayleigh-Jeans approximation of Planck's Law.

$$I(\lambda, T) = \frac{2\pi ckT}{\lambda^4} \quad (3.2)$$

This relationship was known empirically long before Planck derived the quantum mechanical expression, but troubled scientists because the Rayleigh-Jeans expression implies an infinite radiance of energy by matter at very short wavelengths. The explanation of the blackbody emission spectrum by Planck's Law was one of the first successes of quantum mechanics.

From the Rayleigh-Jeans expression it can be seen that radiometer measured antenna power (power above the receiver noise) is linearly proportional to the temperature of the field of view of the antenna. This measured parameter is called *brightness temperature* in radiometry. Temperature is therefore the fundamental observable of the microwave radiometer.

In the case of an antenna pointed to an emitting surface, the average temperature of the target is measured. In the case of a semi-opaque or translucent emitter such as a nonscattering gas in LTE (local thermodynamic equilibrium), Chandrasekhar's equation of radiative transfer is in effect, and the temperature along any view vector is expressed as the sum of (1) the attenuated source $I(\nu, 0)$ beyond the emitter (residual cosmic radiation in the case of atmospheric radiometry) and (2) the integral of the net radiation source $J(\nu, s')$ along the antenna field of view, as attenuated by the intervening medium:

$$\begin{aligned} I(\nu, s) &= I(\nu, 0)e^{\int_0^s \kappa \rho ds'} + \int_0^s J(\nu, s')e^{\int_s^{s'} \kappa \rho ds''} ds' \\ &= I(\nu, 0)e^{-\tau_\infty} + \int_0^s J(\nu, s')e^{-\tau(s, s')} ds' \end{aligned} \quad (3.3)$$

where: κ = absorption coefficient, ρ is density of the absorber, s is optical path length.

In the notation of atmospheric radiometry, and because radiometric antenna temperature is proportional to power, Chandrasekhar's expression is written as:

$$T_b = T_{cosmic}e^{-\tau_\infty} + \int_0^\infty T(s)\alpha(s)e^{-\tau(s)}ds \quad (3.4)$$

where: T_b = sky brightness temperature, the basic radiometer observable

$T_{cosmic} = 2.7K$, the residual cosmic radiation from outer space from the Big Bang

$\tau(s) = \int_0^s \alpha(s')ds' =$ the total attenuation of the atmosphere from the surface to point s along the optical path

$\alpha(s)$ is the attenuation coefficient at s , and equal to $\kappa\rho(s)$

$\tau_\infty = \int_0^\infty \alpha(s')ds' =$ attenuation from the surface to outer space

Utilizing the Mean Value Theorem of calculus, we can approximate and partially linearize the above integral equation by introducing a mean atmospheric temperature defined as (Schroeder and Westwater, 1991):

$$T_{mr} \stackrel{def}{=} \frac{\int_0^\infty T(s)\alpha(s)e^{-\tau(s)}ds}{\int_0^\infty \alpha(s)e^{-\tau(s)}ds} \quad (3.5)$$

This mean radiating temperature can be estimated on a monthly or seasonal basis for a given observation site, and is about 95% of the mean surface temperature. *- in the ic band?* Using the above definition (3.5) for the mean temperature, the brightness observable can be modeled from equation (3.4) as:

$$T_b = T_{cosmic}e^{-\tau_\infty} + T_{mr}(1 - e^{-\tau_\infty}) \quad (3.6)$$

Chandrasekhar's equation is thus simplified from a form previously solvable only by numerical integration. It will be shown in §3.3 that determination of a representative mean radiating temperature is important to the accuracy of the inferred water vapor.

3.2 Retrieval coefficients for water vapor radiometers

The fundamental observable of the water vapor radiometer is sky brightness temperature, the temperature of a blackbody that is emitting at the same intensity as the sky. The sky approximates a blackbody provided that the atmosphere is in local thermodynamic equilibrium (non-scattering). This requirement is satisfied up to about 20 *km*. The atmospheric parameters of interest (to be “retrieved”) are water vapor, liquid water, and radio phase path delay due to water vapor. The absorption (and, by Kirchoff’s Law, the emission) due to water and its vapor are proportional to their density. As was shown in §3.1, in the Rayleigh-Jeans approximation, the absorption and emission are also proportional to temperature.

The radiometric determination of the atmospheric parameters of total integrated water vapor, liquid water, and radio phase path delay is based on “retrieval” methods. These methods utilize large databases of RAOB data from the site of interest, or a climatologically representative site, to calculate sky brightness temperatures for each of the atmospheric profile cases and at the radiometer operating frequencies. Absorption coefficients from line shape models for water vapor and oxygen and absorption coefficients for liquid water are used in the radiative transfer equation.

Retrieval of atmospheric water vapor via microwave radiometry is typically accomplished by observing the emission of radiation from the 22.235 GHz $6_{-5} \rightarrow 5_{-1}$ rotational resonance, although a resonance exists at 183 GHz that is suitable. This emission is proportional to the density and temperature of the water vapor, integrated along the line-of-sight path from the top of the atmosphere to the receiving antenna. In the dual-frequency algorithm used in the UNAVCO-Platteville experiment, regression coefficients were derived from 5 years of Denver Stapleton RAOBs (released at 0 and 12 UT daily). To be independent of atmospheric absorption coefficients (line shape models), microwave radiometer observations simultaneous with RAOB soundings can be regressed,

but this requires a history of WVR observations concurrent with RAOBs. This is generally not practical; alternately, line shape models are utilized to calculate microwave emission along the RAOB sounding path, and these values are then numerically integrated in the radiative transfer equation (3.4). In this thesis we were constrained to the second method. The water vapor line shape model of Liebe [1987] as modified by Keihm [1991] following the joint NOAA-NCAR Winter Icing Storms Project (WISP) experiment, and the oxygen line shape of Rosenkranz [1975] were used, and bilinear regressions of RAOB-measured water, water vapor, and radio propagation delay were each performed against the two channels of radiometric observations. The general opacity-based retrieval equation for an n -channel radiometer is:

$$\text{retrieved parameter} = \sum_{i=1}^{n+1} C_i \ln\left(\frac{T_{mr} - T_{cosmic}}{T_{mr} - T_{b_i}}\right) \quad (3.7)$$

Retrieved parameter here is atmospheric water, water vapor, or vapor-induced radio phase path delay. One could also retrieve based on brightness temperatures directly, but the relationship is less linear and therefore more erroneous for situations that are away from the statistical mean.

The dual-frequency retrieval equations utilized were:

$$\text{integrated liquid} = c0_{liquid} + c1_{liquid} \times \tau_{23.8} + c2_{liquid} \times \tau_{31.4} \quad (3.8)$$

$$\text{integrated water vapor} = c0_{vapor} + c1_{vapor} \times \tau_{23.8} + c2_{vapor} \times \tau_{31.4} \quad (3.9)$$

$$\text{radio phase path delay} = c0_{delay} + c1_{delay} \times \tau_{23.8} + c2_{delay} \times \tau_{31.4} \quad (3.10)$$

Atmospheric spectra in the vicinity of the 22.235 GHz water vapor line for various pressures are shown in Figure 3.1 below. If the atmospheric water vapor lies at low altitude (higher pressure), the spectral line is collisionally broadened. There exist two *hinge points* wherein the emission is relative independent of pressure, and therefore of altitude. The hinge point at 23.8 GHz was chosen for the WVR-1100 because it is in a reserved research waveband where no radio transmission is allowed. The second radiometer frequency at 31.4 GHz is in a

local minimum between the 23.8 GHz water vapor line and the 60 GHz oxygen line. Liquid water (cloud) emits in a monotonically increasing spectrum with frequency. A measurement at 31.4 can separate the cloud liquid and water vapor contributions, as is seen in equations (3.8) and (3.9) above.

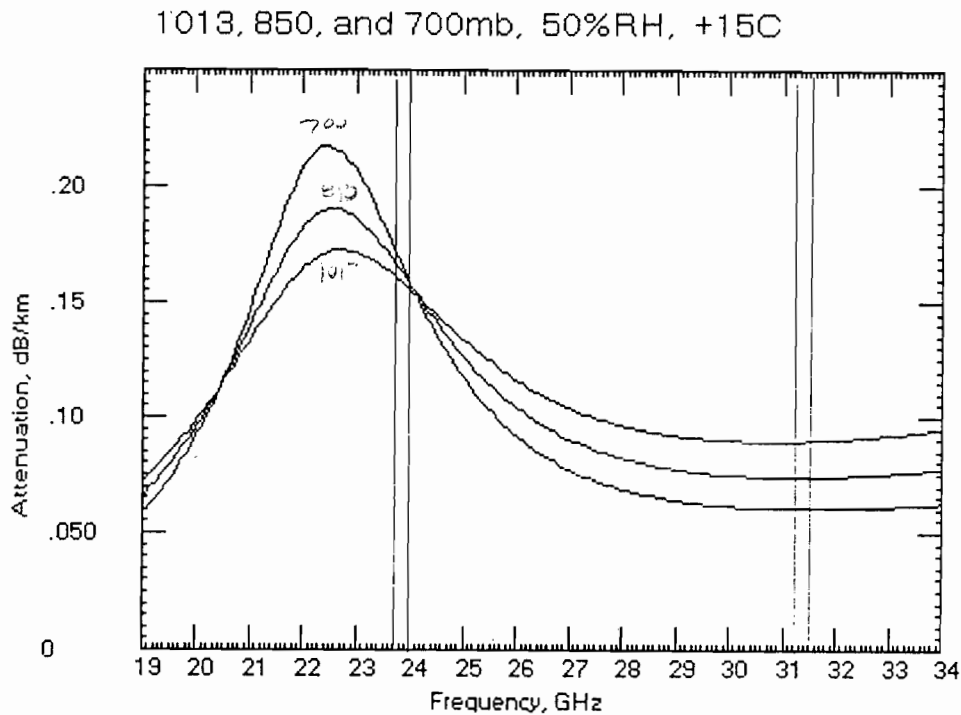


FIGURE 3.1 The spectrum of a 50% humidity 15C atmosphere at 1013,850, and 700 millibars. The receiving bandwidths of the WVR-1100 are shown at 23.8 GHz and 31.4 GHz.

Because of the highly variable distribution of water vapor on the atmospheric temperature profile, one would intuit only a moderately correlation between sky brightness (antenna temperature) and atmospheric water vapor. One would expect only a slightly better correlation between atmospheric opacity at this vapor resonance and atmospheric water vapor. However, because water vapor *tends* to lie in a consistent temperature regime, the correlation of opac-

ity with vapor is very good. And because the opacity is generally quite small (less than 0.1 nepers), the brightness temperature also correlates quite well with vapor. Figure 3.2 below demonstrates this correlation.

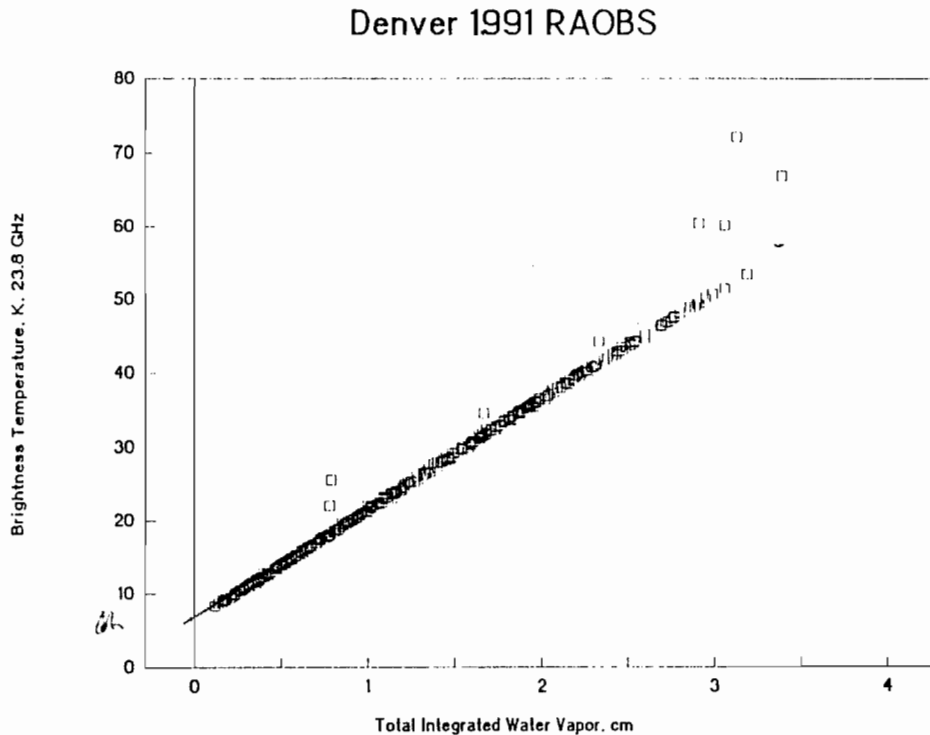


FIGURE 3.2. Radiometer receiver antenna temperature vs. total integrated atmospheric water vapor for 531 RAOBS at Denver in 1991. In the absence of cloud liquid, this single-channel correspondence is very close. These soundings span the entire year. The brightness temperature is determined by numerical integration of the radiative transfer equation from the top of the atmosphere to the surface. The Liebe line shape model as modified by Keihm was used to calculate brightness from water vapor density and local temperature.

The correlation coefficient r^2 of a linear regression fit of the data shown in Figure 3.2 is 0.99. The outliers are soundings in cloudy conditions. If total liquid contents greater than 1 micron of water are culled from these data, r^2 improves to 0.998. At a water vapor value of zero, the brightness intercept is about 5.8K;

this residual brightness is due primarily to emission of the assemblage of oxygen resonances centered at 60 GHz.

Retrieval methods: There are two approaches commonly used to relate the radiometer observables to the retrievables through histories of RAOBs. Both methods numerically integrate each RAOB for total water vapor and liquid water. Both methods utilize line shape models and absorption coefficients for the atmospheric constituents that absorb (water, water vapor, oxygen, and sometimes CO_2 and other lesser interactive molecular species).

Some investigators (e.g., JPL) use these inputs to calculate theoretical downwelling emission, and therefore brightness, for each RAOB, and in turn use these calculated brightnesses in a multilinear regression fit of brightness temperature to the numerically integrated values of water, water vapor, and radio phase path delay [Elgered et al., 1985]. Because the brightness temperatures are not linearly related to atmospheric constituent densities (they are more closely related by an exponential function), deviations from mean values of brightness temperature are sometimes employed to more closely relate the brightness observables to the retrievables.

Other investigators (see Schroeder et al, 1991, Elgered et al., 1985) calculate theoretical opacities (τ) for each RAOB case by numerical integration of the absorption through the atmosphere. This is the preferred method, and the method we implemented, because the retrieval values are more closely related to opacity than temperature. These arrays of [$\tau_{23.8}$, $\tau_{31.4}$, liquid, vapor] are treated in a least squares multilinear regression to establish coefficients for the linearized equations for liquid water, water vapor, and radio phase path delay.

These retrieval coefficients are then used in the following way. Brightness temperatures measured by the radiometer are used to calculate opacities (τ) in each of the two radiometer channels. The opacities are in turn used in the above retrieval equations (3.8-10) to determine the atmospheric parameters.

3.3 The importance of the atmospheric Mean Radiating Temperature and the mean water vapor temperature

To demonstrate the significance of mean radiating temperature in dual frequency retrieval of water vapor, liquid water, or path delay, we can differentiate equation (3.7) w.r.t. T_{mr} and obtain:

$$\begin{aligned} \frac{d(\text{retrieved parameter})}{dT_{mr}} &= \sum_{i=1}^2 C_i \frac{T_{b_i} - T_{cosmic}}{(T_{mr} - T_{cosmic})(T_{mr} - T_{b_i})} \\ &\simeq \sum_{i=1}^2 C_i \frac{T_{b_i} - T_{cosmic}}{(T_{mr})(T_{mr} - T_{b_i})} \end{aligned} \quad (3.11)$$

because $T_{cosmic} \sim 1\%$ of T_{mr} . C_i are the so-called ‘‘retrieval coefficients’’. For low brightnesses (sky brightnesses in the water vapor band around 22 GHz typically range between 8 and 80K), we can approximate the logarithmic opacity function in equation (3.6) with:

$$\begin{aligned} \text{retrieved parameter} &= \sum_{i=1}^{n+1} C_i \ln\left(\frac{T_{mr} - T_{cosmic}}{T_{mr} - T_{b_i}}\right) \simeq \sum_{i=1}^{n+1} C_i \left(\frac{T_{b_i} - T_{cosmic}}{T_{mr} - T_{b_i}}\right) \\ \text{retrieved parameter} &\simeq T_{mr} \frac{d(\text{retrieved parameter})}{dT_{mr}} \end{aligned} \quad (3.12)$$

Or:

$\left. \begin{matrix} \text{17K} \\ \text{20K vapor} \end{matrix} \right\} \delta_{\text{vap}} = .05 \text{ mm Vap}$

$$\frac{\delta_{\text{vapor}}}{\text{vapor}} \sim \frac{\delta T_{mr}}{T_{mr}}, \quad (3.13)$$

accurate to within 10% for sky brightnesses between about 5 and 40K.

Thus a 10K overestimation in T_{mr} (typically around 270K) will result in about a 3% underestimation of water vapor and a resultant underestimation in radio phase path delay. To compound this, because of the inverse temperature dependence of refractivity in the third term of equation (2.18), an overestimation of the temperature of the water vapor (highly correlated to T_{mr}) will result in an underestimation of phase delay. Error in the inferred propagation delay due

to water vapor has therefore a quadratic dependence upon the error in mean temperatures used in linearizing the radiometric equations that infer propagation delay due to water vapor.

Typical variability of the mean radiating temperature of water vapor is shown in Figure 3.3 below.

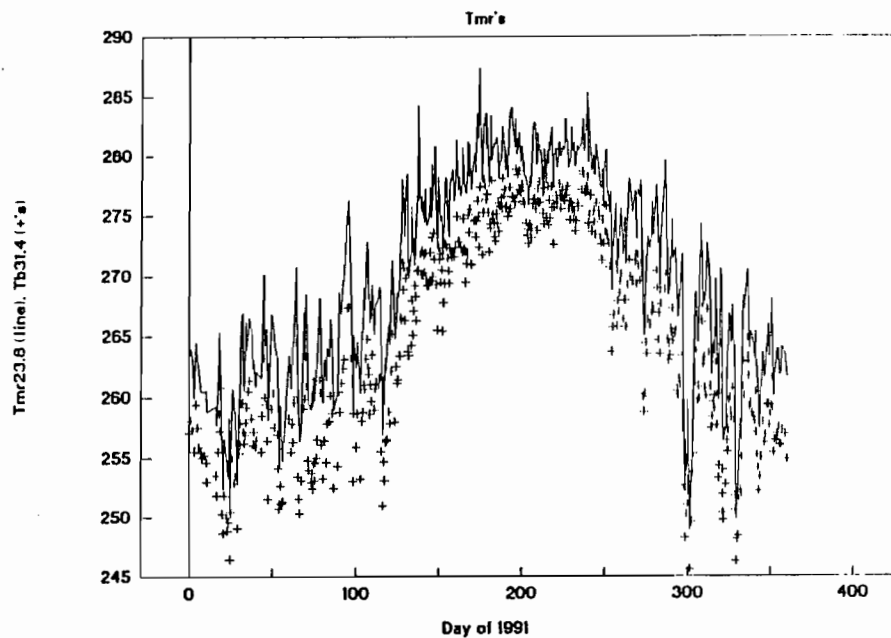


FIGURE 3.3. The mean radiating temperature of the atmosphere above Denver for the year 1991 using the Keihm-modified Liebe 1987 model. Rawinsonde observation balloons (RAOBs) are released at 0 and 12 UT; a diurnal variation of about 5K rms is evident. Weather regimes also modulate the mean radiating temperature by as much as 25K; the seasonal variation is about 20K rms.

The proportionality constant between water vapor burden and phase delay has generally taken to be $delay = 6.5 \times vapor\ burden$, but can vary between about 6.2 and 6.9 (about 5% from the mean) with season and with changes in weather. [Bevis et al., 1992; Chiswell et al., 1993]. This variability is shown in

Figure 3.4 below. This factor also varies with site and with/without solar surface and atmospheric heating (day/night). Because the accuracy of GPS geodesy has evolved (from ppm in the mid 1980s to ppb today), a more accurate relationship is needed.

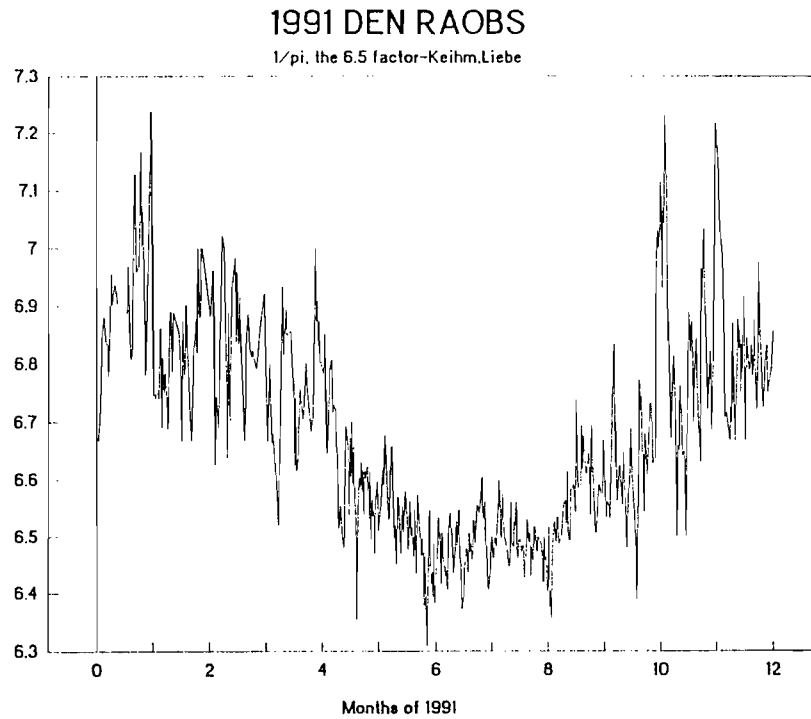


FIGURE 3.4 Plot of the ratio of vapor-induced phase path delay to total integrated water vapor (the “6.5 factor”) calculated from Denver 1991 RAOBs and using the Keihm-modified 1987 Liebe model. Diurnal, seasonal, and weather feature effects are visible in the data.

The water vapor radiometer observable *brightness temperature* is related to emission along the line-of-sight of the instrument by the Radiative Transfer equation. Emission is $\propto \rho_{vap}T$ (directly proportional to temperature at altitude), whereas the desired retrievable *refractivity* $N = 77.6 \frac{\rho_{vap}}{T} + 3.5 \times 10^5 \frac{\rho_{vap}}{T^2}$ (an inverse proportion to temperature). Therefore, the refractivity (using the

6.5 factor) derived from statistical retrieval of water vapor is only accurate to the extent that the temperature profile, weighted with the water vapor density, is predictable; this is what defines T_{mr} . Because the saturation vapor pressure is a strong function of temperature, and because the vapor source is at the surface, the vapor emission tends to be dominated by density in the warmer temperatures near the surface. The statistical validity of retrievals can be demonstrated in several ways. The routine that generates retrieval coefficients from RAOB histories also directly computes statistical parameters on the RAOB data set. Statistical retrieval errors are discussed in §3.6.

Retrieval coefficients for phase path delay can be generated from RAOBs in the same fashion that they are generated for vapor and liquid burdens. Such retrievals, in effect, include a statistical estimate of T_{mr} and therefore eliminate some of the error due to T_{mr} . Such retrieval coefficients are more accurate because they include some of the climatological as well as site dependence of delay. In the alternative, the “6.5” factor or T_{mr} can be varied by site, hour of the day, and season to accommodate such variations. Because T_{mr} is highly correlated for short baselines, T_{mr} was held constant in this experiment (see §5.2.1). Because the delay retrievals as currently calculated are unstable in the presence of cloud (apparently because of a glitch in the cloud model in the modified JPL retrieval software I used), I have chosen to use the 6.5 factor after confirming its validity during the autumn season in the Denver area by generation of RAOB retrievals for both delay and vapor, and ratioing for several days of WVR observations. This approximation did not effect the results for this short baseline.

3.3.1 Atmospheric mean temperatures and liquid water (cloud) retrieval

Retrieval of cloud liquid is based on the nonresonant emission of liquid water. This emission is proportional to absolute temperature of the radiator by the Rayleigh-Jeans approximation. The retrieval of liquid water is therefore

dependent upon the temperature regime of the liquid water being retrieved. A moderately wet cloud can contain 1 g/m^3 , and the vertical dimension can be 3 to 5 km . The freezing level can lie anywhere from below the surface to 7 or more km . A low elevation angle path through 10 km of 1 g/m^3 cloud can induce a delay of 1.45 cm (§2.2.4.1). The liquid in this cloud is generally between -5C and $+20\text{C}$, or a variation of about 10% in absolute temperature. The retrieved uncertainty can therefore be about 1.5 mm . Microwave radiometry does not at present have a method of measuring liquid water and determining its temperature. The uncertainty of the temperature of the cloud liquid is therefore a source of unmodeled error in water vapor radiometry. However, statistical retrievals include cloud habitat through the RAOBs, and tend to diminish cloud temperature errors. When dense clouds are present, path delay errors are at the mm level. Regressions of RAOB sets for cloud liquid yield statistical standard deviations between 0.4 mm and 1.6 mm for the Denver RAOB sets between 1987 and 1992; this wide variation in σ indicate that the data sets are small and/or the statistical description is poor.

3.3.2 Mapping functions

Much work has been done to map zenith water vapor observations and propagation delay measurements to non-zenith elevation angles. The functions that relate zenith observations to non-zenith values are called mapping functions (see, for example, Marini, 1972; Chao, 1972; Davis *et al.*, 1985). Additionally, these mapping functions make corrections for sphericity of the atmosphere and for radial ray bending due to refractive gradients. An example of a simple mapping function (plane parallel atmosphere, no ray bending) is the cosecant function:

$$f(\epsilon) = M(\epsilon) \times f(\text{zenith}) \quad (3.14)$$

where ϵ is the elevation angle, and

$$M(\epsilon) = \csc(\epsilon) \quad (3.15)$$

This expression is, however, far from sufficient for the level of accuracy required for GPS geodesy.

Mapping functions of the tropospheric delay as a function of elevation angle are routinely required and employed in VLBI solutions because the baselines being measured are generally long, and mutually visible celestial sources employed are consequently often at low elevation angles. The same mapping functions are applicable to GPS observations. Tropospheric and ionospheric model limitations and antenna multipath restrict GPS to elevation angles above 10 degrees. I have used current GPS receivers to track to about 0.5 degrees *below* the geometric horizon; much additional geometric strength could be gained from low observation angles. A simple mapping function for a plane parallel medium is $\csc(\theta)$ where θ is the elevation angle of the source. At low elevation angles, tropospheric and ionospheric curvature and ray bending prescribe more elegant mapping functions. Additionally, Rogers and Neill [1993] report a seasonal and latitudinal dependence of the dry atmosphere mapping function, which is primarily due to the variation in thickness of the troposphere with season and latitude.

The Davis *et al.* mapping function CfA-2.2 is a marked improvement over previous mapping functions:

$$M(\epsilon) = \frac{1}{\sin \epsilon + \frac{a}{\tan \epsilon + \frac{b}{\sin \epsilon + c}}} \quad (3.16)$$

where a and b are linear functions of surface pressure, temperature, and water vapor partial pressure, and temperature lapse rate and height of tropopause. The coefficients of these linear functions are established with multilinear regression fit of raytraced paths through various RAOB-defined atmospheres.

Lower elevation angles are required for covisibility of sources on long VLBI baselines, but for GPS geodesy the gain in position solution accuracy from low

angle observations is offset by complications of multipath propagation and tropospheric mapping requirements. VLBI antennas have large diameters and therefore narrow beamwidths which puts the accompanying side lobes close in to the main beam. Because of the small antenna aperture of water vapor radiometers, the antenna side lobes are spread from the antenna axis, and receive ground signal at low elevation angles. Because of this and the mapping function deficiencies, it is general practice in water vapor radiometer-augmented GPS geodesy to establish an elevation cutoff at 10 to 15 degrees.

Mapping functions are also normally utilized to map zenith water vapor measurements to low elevation angles. In contrast, in the UNAVCO to Platteville experiment the line of sight observations to each of the GPS satellites produces sky brightnesses at elevation angles other than zenith that are then used to infer water burdens, water vapor burdens, and propagation path delays through equations 3.10-3.12. In order to use zenith retrieved coefficients to infer these parameters for non-zenith line of sight paths it must be demonstrated that insignificant error is induced in the linearization of the Radiative Transfer Equation for a representative atmosphere. Solving Equation (3.4) for τ , (atmospheric opacity, proportional to vapor content and delay), we write:

$$\tau(\epsilon) = \ln\left(\frac{T_{mr} - T_{cosmic}}{T_{mr} - T_b(\epsilon)}\right) = \tau(z)M(\epsilon) \quad (3.17)$$

Because of the transcendental logarithmic function, it is not possible to derive an exact expression for the mapping function. Therefore, as a demonstration of the sufficiency of this approximation, Denver RAOB soundings for several years were regressed for retrievals at zenith and at 30 degrees. At elevation angles lower than about 15 degrees the simple cosecant mapping function is no longer valid; hence, for simplicity, 30 degrees was chosen. This comparison confirmed the validity of mapping $tau(\epsilon) = \tau(z)/sin(\epsilon)$ to better than 1

3.4 Line shape and continuum absorption models

As mentioned above, the retrieval coefficient determinations rely directly upon models of atmospheric absorption. Accuracy of these models has directly affected the retrieved values of vapor, liquid, and vapor delay. The major absorbers are water vapor and oxygen. This absorption spectrum has large uncertainties associated with it, and is continually being upgraded and improved. JPL has historically used the Waters 1976 water vapor line shape model and the Rosenkranz 1975 oxygen model for generating retrievals of water vapor. NOAA WPL uses the Liebe 1987 water vapor model (with line strength and width coefficients upgraded to Fall season of 1988) and the 1988 Rosenkranz oxygen model.

I used the 1991 Keihm-modified Liebe 1987 vapor and 1975 Rosenkranz oxygen models, although Liebe's 1989 vapor model (with line coefficients current to 1992 data) shows promise (I currently have no way to verify the veracity of this model, without RAOBs concurrent with 23.8 GHz radiometer observations). However, the Keihm model is based on a consistent set of recent data focused on the radiometer wavebands of interest, whereas the Liebe model is broadband (1 to 1000 GHz), and is based on data from many different experimenters and experimental techniques. These Keihm model modifications are an 8% increase of the Liebe 1987 line shape and continuum and a 15% increase in the 5 to 40 GHz wing only of the Rosenkranz 1975 absorption models. The increases are based on recent radiometer/RAOB data from a joint JPL-NOAA-NCAR-Radiometrics (WISP) experiment in the Spring of 1990, and on data from a JPL J-series water vapor radiometer that was modified to tune across the 3.3 GHz line and operated for 6 months.

The most recent 1992 Rosenkranz model is 7% below the Keihm results in the 5 to 40 GHz wing [S. Keihm, personal communication].

This required enhancement of the oxygen and water vapor absorption models is echoed by the corrections to brightness that are applied to the NOAA/WPL

radiometers [Westwater et al., 1990]. NOAA calculated expected brightness temperatures from clear sky radiosonde profiles measured at Denver and San Nicolas Island, CA. These radiosonde data were concurrent with radiometer observations. It was found that the Gross (as modified by Waters) line shape agreed better than the Van-Vleck Weisskopf [Liebe 1969] with measured data at 20.6 and 31.65 GHz; however, both models underestimated brightness (by 6% and 14%) in the vicinity of the water vapor resonance at 22.235 GHz. At 31.65 GHz, the NOAA correction is predominately an offset of about 0.8K to the Liebe 1989 model, indicating that perhaps the underlying oxygen contribution is too small (the 1988 model of Rosenkranz was used). The correction to the Waters model is also the same 0.8K offset, with an accompanying 3.5% underestimation of line strength.

At 20.6 and 31.65 GHz the 1989 Liebe model (utilized by NOAA) is about 4.5% more absorptive than the 1987 Liebe model (utilized by Keihm); the *Keihm* correction to Liebe 1989 would therefore be a 3.5% increase, in contrast to the 15% increase implied by the NOAA data. The 0.8K increase indicated by the NOAA data to the underlying continuum would be reflected in roughly a 20% increase. This estimate is inexact because the contribution from the underlying continuum is small; noise related to the total measurement is therefore very significant relative to this small component.

3.5 Conversion of relative humidity or temperature-dewpoint data to water vapor density

RAOBs are archived in different formats; some use relative humidity, others (like Forecast Systems Laboratory RAOBs that I am using) use temperature and dewpoint. To convert from these measurements to vapor density, an expression fitted to the Smithsonian Tables version of the Goff-Gratch integration of the Clausius-Clapeyron equation was utilized. This streamlined formulation matches the Smithsonian values within $\pm 0.3\%$ over the range $\pm 40C$, and was incorporated to expedite execution time of the inversion program.

The Clausius-Clapeyron equation for saturation vapor pressure over water reflects the atmosphere's ability to hold water as a function of temperature:

$$\frac{de_s(T)}{dT} = \frac{m_v L_c e_s(T)}{RT^2} \quad (3.18)$$

or, by Goff-Gratch integration over water (Smithsonian Meteorological Tables):

$$\begin{aligned} \log_{10} e_s(T) = & \overset{-7.903}{-7.903}(T_s/T - 1) + 5.028 \log_{10}(T_s/T) \\ & - 1.382 \times 10^{-7} (10^{11.34(1-T/T_s)} - 1) \\ & + 8.133 \times 10^{-3} (10^{3.491(T_s/T-1)} - 1) + \log_{10} e_s(T_s) \end{aligned} \quad (3.19)$$

The Goff-Gratch integration over ice:

$$\log_{10} e_i(T) = -9.097(T_0/T-1) - 3.567 \log_{10}(T_0/T) + 0.8768(1-T/T_0) + \log_{10} e_i(T_0) \quad (3.20)$$

where

e_s is the saturation vapor pressure over water, ^{mb} at 373.16

e_i is the saturation vapor pressure over ice, ^{mb} at 273.16

$e_s(T_s) = 1013.2 \text{ mb}$,

T is temperature (Kelvins),

$T_s = 373.16 \text{ K}$, the STP steam point,

$T_0 = 273.16 \text{ K}$, the STP ice point,

m_v is the molecular weight of water = 18g/mole

L_c is the latent heat of condensation (vaporization) = $2.5 \times 10^{10} \text{ ergs/g}$,

and R is the universal gas constant = $2.87 \times 10^6 \text{ cm}^2/\text{sec}^2 - \text{K}$.

A satisfactory and useful approximation to this integration over water is [Bögel, 1977]:

$$e_s(T) = 2.407 \times 10^8 \left(\frac{300}{T} \right)^5 \exp\left(-22.64 \frac{300}{T}\right) \quad (3.21)$$

The ratio $\frac{300}{T}$ is preserved in the above expression because it is a commonly defined inverse temperature parameter. This expression is accurate to 0.2% for $\pm 40C$ and is useful in streamlining retrieval coefficient calculations wherein tens of thousands of calculations of vapor pressure are required (for instance, in generating WVR retrieval coefficients from RAOBs). It is also a handy shortcut for hand calculators. The expression can be improved to within 0.02% of the Goff-Gratch integration over $\pm 40C$ by slightly diminishing two of the constants:

$$e_s(T) = 2.376 \times 10^8 \left(\frac{300}{T}\right)^5 \exp\left(-22.613 \frac{300}{T}\right)$$

$$= 100 \left(\frac{300}{T}\right)^5 \exp\left(\underbrace{19.427}_{\text{not quite on}} - 22.613 \frac{300}{T}\right) \quad (3.22)$$

Note that a 2K increase in temperature results in a 10% increase in the saturation vapor pressure (the *capacity* of the atmosphere to hold water, not necessarily the increase in water vapor); thus the significance of small increases in global temperatures.

use Boyel: $e_s(T) = 100 \left(\frac{300}{T}\right)^5 \exp\left[21.602 \left(1 - 1.0482 \left(\frac{300}{T}\right)\right)\right]$

3.6 Discussion of WVR instrumental and retrieval errors and sources

3.6.1 RAOB errors

Uncertainties in the three RAOB measurements (T, pressure, RH) result in uncertainties in the retrieval coefficients, and therefore in the retrieved values. The relative humidity problems due to the limitations of the carbon hygistor are dealt with in software filters within the RAOB inversion program. Typical errors of currently used RAOBs are as follows: 0.6K rms in temperature, and about 2 mb in pressure. Additionally, carbon hygistors used for the relative humidity measurement are accurate to within about 5%, are not valid below 20% RH, and are uncertain above about 93%. Hoehne [1980] reports NWS radiosonde statistics of $\pm 0.7mb$, $\pm 0.84C$, and $\pm 3.4C$ (about $\pm 18\%$) in dewpoint. Neill [1992] reports 1.6 mb pressure, 0.4K temperature, 5% relative humidity, and

~100 meters radiosonde height uncertainties. Schmidlin et al. [1982] reports similar uncertainties.

Such deficiencies in accuracy tend to make retrieval coefficients insensitive, and in the case of the hygrometers, to bias regressed retrieval coefficients. The measurement uncertainties in temperature and pressure are included in the retrieval inversion in a simplified manner: they are interpreted as an error solely in temperature and estimated at 0.9K rms.

These errors are then added in an independent sense to the radiometer measurement (calibration, resolution) errors of 0.4K, and the resultant total error is then converted to an error in opacity (this, because we are inverting for retrievals based on opacity). This opacity uncertainty is then used as a constraint (freedom) in the inversion process by adding its square to the diagonal elements in the opacity covariance matrix used in the inversion.

3.6.2 Statistical and instrumental errors of retrieval methods

Because the dual-channel retrieval of water vapor is a statistical method, there are statistical variances in the inferred water vapor data. Water vapor is not well-behaved as is, say, oxygen, a well mixed atmospheric constituent that is subject to the hydrostatic equation.

The ability to retrieve water vapor from radiometric observations depends upon the validity of the mean radiating temperature T_{mr} estimate. T_{mr} depends upon the distribution of the water vapor along the atmospheric temperature profile; variations of 10% in T_{mr} commonly occur with changes in weather regimes, and can vary 20% seasonally. As shown in §3.3, these variations result in errors of like magnitude in retrieved water vapor. Such variations are, of course, site dependent and also depend upon if cloud is present. Gary et al. [1985] find errors of about 2.7 mm rms in vapor retrieval for clear conditions, 5.1 mm for cloudy conditions, and 3.8 mm overall. These results were for retrievals based on brightness temperatures and all seasons were binned into one set. Seasonal variations are therefore not considered. Using a fixed T_{mr} , Westwater et al.

[1989] retrieve based on opacity (which is more closely related to total water vapor content) and find 2 to 3 *mm* rms deviations between NWS RAOBs and their radiometer. Westwater now utilizes monthly values for T_{mr} in the NOAA radiometer retrievals, but has not published the improvement in accuracy. Elgered [1993] also finds several *mm* rms error in dual channel retrieval algorithms. Most recently, Martner et al. [1993] report 1.1 *mm* rms difference in water vapor between NOAA dual-channel WVRs and CLASS soundings during the 1991 WISP experiment.

Johansson et al. [1987] find similar results for numerous retrieval methods, with retrievals correlated to brightness temperatures and some correlated to *linearized* opacity. The rms errors varied from 2 to 5 *mm* depending upon the site and for retrievals based on brightness only, and from 1.5 to 3 *mm* for retrievals that included seasonal (day-of-year) and surface meteorology.

Since the above studies were performed, the line shape models for oxygen and for water vapor have been updated [Keihm, 1991], with an 8% increase in the strength of the 60 GHz oxygen line wing under the 22 GHz resonance, and a 15% increase in the water vapor line itself. Dr. Liebe concurs with these increases (personal conversation), and these increases are also present in the latest Liebe [1993] MPM model. These more representative line strengths would presumably improve the above results to a small extent.

For the UNAVCO-Platteville experiment we used a seasonal set of retrieval coefficients based on opacity only. We therefore expect about 2 to 3 *mm* rms error in the retrieval. We did not stratify for the presence/absence of clouds in deriving the retrievals; the number of cloudy RAOBs available during the Fall in Colorado made the statistics rather weak. We did solve for the GPS position using WVR phase path corrections both with the updated line shape models and with the older line strengths. The results are discussed in Chapter 5.

3.6.3 Instrumental errors

As detailed in §4.2, the theoretical resolving ability of the WVR-1100 is about 0.3K. This theoretical value is confirmed by long-term observations of a stable liquid nitrogen target. This noise results caused 0.3mm rms vapor noise. Additionally, there can exist calibration drifts that manifest themselves as biases. Repetitive calibrations show this drift to be less than 1K in a diurnal cycle and can be compensated for with a temperature coefficient in the software. Furthermore, the calibration procedure was repeated several times a day during the experiment. The calibration error is therefore assumed to be less than 0.4 mm.

3.6.4 Errors in Mean Radiating Temperature T_{mr}

Errors in mean radiating temperature affect both the refractivity (path delay) due to water vapor, and the microwave emission of water vapor. In §3.3 I showed that:

$$\frac{dvapor}{vapor} \simeq \frac{dT_{mr}}{T_{mr}} \quad (3.23)$$

and in §2.2.3, that the “wet” portion of the vapor-induced refractivity is shown to be inversely proportional to temperature of the vapor:

$$N_{vap} = 64.8 \frac{P_{~~vap~~}}{T} + 3.776 \times 10^5 \frac{P_{vap}}{T^2} = 64.8 \rho_{vap} R + 3.776 \times 10^5 \frac{\rho_{vap} R}{T^2} \quad (3.24)$$

Thus, errors in T_{mr} induce quadratic errors in path delay as inferred from WVR measurements; e.g. a 2% error in estimation of T_{mr} will result in a 4% error in phase path delay. These errors are slightly mitigated by a slight temperature dependence of the absorption line shape profile.

3.6.4 Errors in Mean Radiating Temperature T_{mr}

Errors in mean radiating temperature affect both the refractivity (path delay) due to water vapor, and the microwave emission of water vapor. In §3.3 I showed that:

$$\frac{dvapor}{vapor} \simeq \frac{dT_{mr}}{T_{mr}}, \quad (3.23)$$

and in §2.2.3, that the “wet” portion of the vapor-induced refractivity is shown to be inversely proportional to temperature of the vapor:

$$N_{vap} = 64.8 \frac{P_{vap}}{T} + 3.776 \times 10^5 \frac{P_{vap}}{T^2} = 64.8 \rho_{vap} R + 3.776 \times 10^5 \frac{\rho_{vap} R}{T^2} \quad (3.24)$$

This local physical temperature T is closely related to T_{mr} and is often expressed as *mean temperature* T_m :

$$T_m = \frac{\int_0^\infty \rho dz}{\int_0^\infty \rho/T dz} \quad (3.25)$$

Thus, errors in estimation of atmospheric temperatures tend to induce quadratic errors in path delay as inferred from WVR measurements; e.g. a 2% error in estimation of T_{mr} and T_m will result in a 4% error in phase path delay. These errors are slightly mitigated by a slight temperature dependence of the absorption line shape profile.

3.6.5 Radiometer levelling errors

Because the beam steering mirror elevation angle references to the frame of the radiometer, radiometric observations are sensitive to errors in leveling of the instrument. The opacity inferred from observations is a linear function of optical path length and therefore of air mass along the observation path, and therefore has a $\frac{1}{\sin\theta}$ dependence, where θ is the elevation angle of the observation. Retrieval coefficients for water vapor and liquid water are generally formed as linear functions of atmospheric opacities at two wavebands. The dependence of these two quantities therefore follows the dependence of opacity upon elevation angle. Beamwidth of the radiometer is assumed infinitely narrow in this analysis; typical beamwidths range from 2.5 to 7.5 degrees and become significant at low elevation angles.

The absorption along any observation path at elevation angle θ can be written as (ignoring mapping functions):

$$\tau(\theta) = \int_0^\infty \alpha(s) ds = \frac{1}{\sin\theta} \int_0^\infty \alpha(h) dh \quad (3.25)$$

for a plane parallel atmosphere, where $\alpha(h)$ is the absorption coefficient along a slant path of elevation angle θ .

For slant paths we can write:

$$\tau(\theta) = \frac{\tau_z}{\sin\theta} \quad (3.26)$$

Differentiating the expression for τ w.r.t θ :

$$\frac{d\tau(\theta)}{\tau(\theta)} = -\frac{d\theta(\text{radians})}{\tan\theta} \quad (3.27)$$

yielding the dependence of opacity upon leveling errors $d\theta$. The inferred water vapor and liquid water have roughly the same error dependence (the NOAA WPL dual-band radiometer retrieval algorithm is used here):

$$\frac{d(\text{water vapor})}{\text{water vapor}} = -\frac{c_{0v} + c_{1v}\tau_{23} + c_{2v}\tau_{31}}{c_{1v}\tau_{23} + c_{2v}\tau_{31}} \frac{d\theta}{\tan\theta} \simeq -\frac{d\theta}{\tan\theta} \quad (3.28)$$

$$\frac{d(\text{liquid water})}{\text{liquid water}} = -\frac{c_{0l} + c_{1l}\tau_{23} + c_{2l}\tau_{31}}{c_{1l}\tau_{23} + c_{2l}\tau_{31}} \frac{d\theta}{\tan\theta} \simeq -\frac{d\theta}{\tan\theta} \quad (3.29)$$

because the offset coefficients c_{0x} are small, generally much smaller than 1 *mm*.

The error in τ , water vapor, and liquid water per *degree* of leveling error as a function of elevation angle is shown below in table 3.1 (again, assuming zero beamwidth):

TABLE 3.1 Leveling Errors	
Elevation angle, degrees	PerCent error/degree
10	-10
20	-5
30	-3
45	-1.7
80	-0.3
90	0

The brightness temperature error (the fundamental observable of the radiometer) as a function of $d\theta$ is not so simple:

$$T_B(\theta) = T_{\text{cosmic}}e^{-\tau(\theta)} + T_{mr}(\theta)(1 - e^{-\tau(\theta)}) \quad (3.30)$$

$$\begin{aligned} dT_B(\theta) &= (T_{mr}(\theta) - T_{\text{cosmic}})e^{-\tau(\theta)}d\tau(\theta) + (1 - e^{-\tau(\theta)})dT_{mr}(\theta) \\ &= (T_{mr}(\theta) - T_B(\theta))d\tau(\theta) + (1 - e^{-\tau(\theta)})dT_{mr}(\theta) \end{aligned}$$

$$\frac{dT_{mr}(\theta)}{d\theta} = \frac{d}{d\theta} \frac{\int_0^\infty T(h)\alpha(h)e^{-\tau(h)/\sin(\theta)} dh}{\int_0^\infty \alpha(h)e^{-\tau(h)/\sin(\theta)} dh} = \frac{\int_0^\infty T(h)\tau(h)\alpha(h)e^{-\tau(h)/\sin(\theta)} dh}{\int_0^\infty \tau(h)\alpha(h)e^{-\tau(h)/\sin(\theta)} dh} \quad (3.31)$$

This expression is insoluble to a closed form using physically meaningful expressions. But T_{mr} is a slowly varying function with elevation angle, being about 95% of the surface temperature at zenith and equal to the surface temperature for horizontal paths. Most of this 5% variation in temperature occurs at very shallow elevation angles. Thus, for elevation angles above 20 degrees the mean temperature is essentially constant, and our expression can be approximated by:

$$dT_B(\theta) = (T_{mr}(\theta) - T_{cosmic})e^{-\tau(\theta)}d\tau(\theta) \quad (3.33)$$

or

$$\frac{dT_B(\theta)}{d\theta} = \frac{T_{mr}(\theta) - T_B(\theta)}{\tan\theta}\tau(\theta) \quad (3.34)$$

3.7 Generation of retrieval coefficients for WVR92

I have modified some JPL VAX code to generate retrieval coefficients. I have converted it to run on a PC, and have further modified it to generate retrieval coefficients for liquid, water, and phase path delay based on opacity rather than upon brightness temperatures.

I obtained RAOB data from the NWS site at Stapleton for the years 1987 through 1991. I have used these data to generate retrievals for each of the years, and for the periods August through October, September through November, and September for each of these seven years, and have compared the resultant coefficients. One expects the coefficients to vary slightly due to climatological drift and other variations.

Because I originally planned an additional WVR-GPS experiment on the PGGA (Permanent Geodetic Geophysical Array) triangle, I also obtained RAOBs for 1989 through 1992 for several sites that surround the Piñon Flat (PFO) site in California; these sites are San Diego (Miramar NAS, proximate to Scripps), Point Magu Naval Air Station (25 miles west of Los Angeles International Airport), and Edwards Air Force Base (in the high California desert and about 100 miles NNW of PFO). I have also obtained Tucson to compare

for sensitivity to climatology. Preliminary results are encouraging in that Edwards and San Diego are quite close, indicating that the retrievals might be rather insensitive to location within southern California, and that retrievals can be objectively estimated to within acceptable errors for Piñon Flat from surrounding sites. Further, it was found in the UNAVCO-Platteville experiment by experimenting with variations in retrieval coefficients due to variations in water vapor line shape models, that the geodetic accuracies are somewhat insensitive to errors in the retrieval coefficients on short baselines (provided that the atmospheres at the ends of the baseline are similar).

Chapter 4 The Water Vapor Radiometers used in these Experiments

4.1 Design of the radiometer

This dual channel radiometer was originally conceived as a portable water vapor measurement device for GPS geodesy. The initial prototype, called the WVR1000, was developed under Department of Commerce SBIR funding, and was completed in 1988. It weighed about 45 lbs. and could be operated on battery power. However, this prototype was unstable with ambient temperature in its gain response, and the noise diode used as a calibration standard also had temperature dependence. The software was crude and did not model some of the crucial instrument response characteristics. Significant changes to the prototype design were required to bring the receiver to its current resolving power of 0.2K and accuracy of 0.3K. This level of performance is required to correct for tropospheric water vapor delays in GPS geodesy. The evolved receiver is called the WVR-1100.

This chapter describes in detail the theoretical analysis that was applied to the radiometer as well as the defining measurements of radiometer performance that were made. The controlling software and algorithms are also described. The modifications that brought the instrument from prototype to its current level of performance are described in §4.1.3.

4.1.1 Overview of the radiometer

The WVRs used in this experiment were designed for simplicity and portability. A drawing of the radiometer is shown below.

The Radiometrics WVR-1100 radiometer can be described as a total power radiometer, with a calibrated gain reference (a *hot load* in the form of a noise source) switched into the antenna system. This switching is done, not with a

WATER VAPOR RADIOMETER

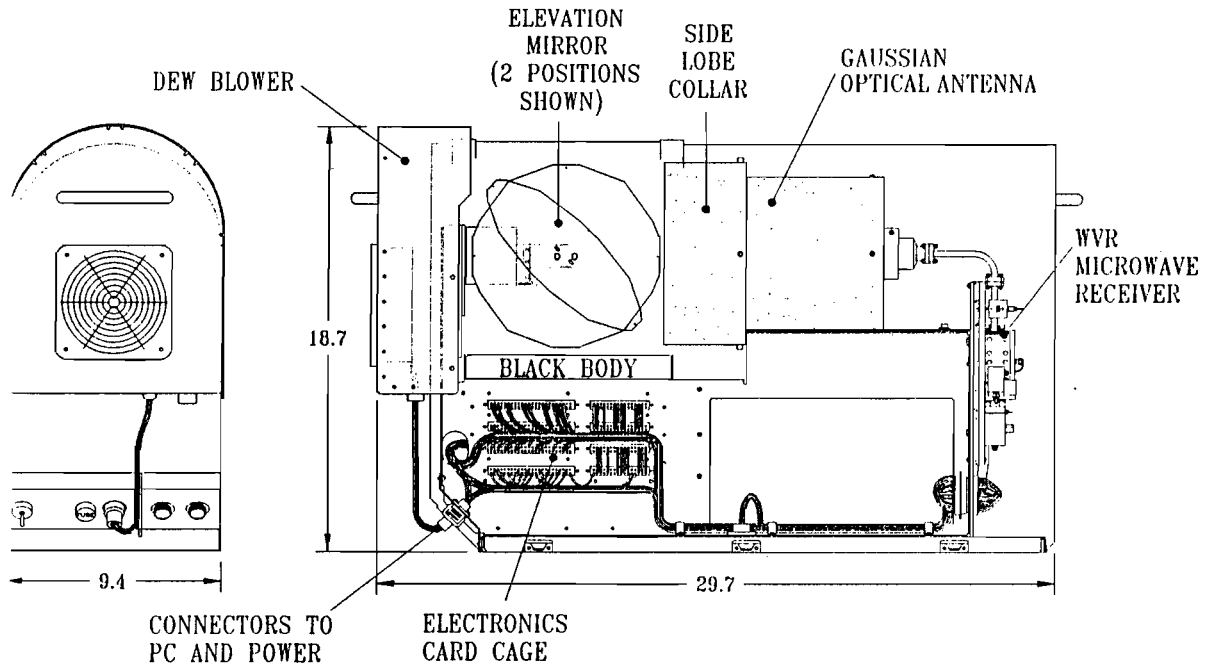


FIGURE 4.1 The WVR-1100 microwave water vapor radiometer

Dicke switch, but with a 30dB waveguide crosscoupler that couples in a noise diode that is turned on and off. Switching to an ambient reference is done by directing the mirror, and therefore the field of view of the radiometer, to a blackbody target of known physical temperature. This *hot load* reference therefore includes the entire radiometer system, including the antenna and feed horn, but excludes the hydrocarbon foam window. This feature is different from other radiometer systems wherein the antenna and feed system is switched out of the system, and the hot load switched in. In such systems the antenna losses must be estimated or measured by other means to calibrate the radiometer.

4.1.2 Electronic description of the radiometer receiver

Sky signal passes through the dielectric window to the elevation mirror and is directed into the gaussian optical antenna. From the gaussian optical antenna the signal passes through a cross-guide coupler that injects signal on command from a noise diode reference. The antenna signal then passes through an antenna isolator that blocks local oscillator leakage through the mixer from passing back out of the antenna being reflected back into the receiver as noise. The antenna signal then enters the RF port to the crossbar balanced mixer, where it is downconverted by the mixer. This downconverted signal is amplified about 65 dB, detected by a square law detector, and then amplified again by an instrumentation current amplifier. The detector-amplifier has a bandwidth of 50 to 200 mHz. The total bandwidth of the double sideband receiver is therefore 400 mHz centered at the LO frequency, minus the central 100 mHz, or 300 mHz. Output of the radiometer is scaled to 1 volt change in output for 500K of antenna signal change.

Output voltage of the amplifier is measured with a voltage-to-frequency converter. This V to F converter is calibrated during an observation cycle by referencing to system ground and to a 10 volt precision voltage reference. The V to F converter is a VCO that generates a harmonic signal whose frequency is proportional to the receiver video voltage. Zero crossings of this oscillator are counted for a predetermined interval (set to 0.5 seconds in the firmware of the EPROM on the digital board); thus, the number of zero crossings N is proportional to the receiver output voltage. The total observation period at any target can be set by the user to the sum of an integral number of 0.5 second observations; this is done in the WVR.cfg file.

4.1.3 Radiometer modifications

Subsequent to its original design in 1987, numerous modifications to the radiometer were conceived, designed, and implemented by me to increase the

WVR performance and stability. These modifications have brought the accuracy to 0.3K and resolution to 0.2K (water vapor resolution of 0.2 *mm*). These enhancements included:

1) Thermal stabilization of the RF portion of the receiver such that the effect of changes in ambient temperature upon the receiver calibration was minimized. The RF deck is held to within several tenths of a Kelvin.

2) Thermal stabilization of the noise diode mount to within several hundredths of a Kelvin. Noise diodes are GaAs avalanche diodes that have a temperature dependence of output that is somewhat less than 0.009dB/C.

4) Burn-in of the noise diode by running for a period of time at a current level well above the normal operating current of 10 ma. This appears to *season* the diode.

5) *Simmering* of the noise diode by running a forward current through the device when RF was not required. This keeps the junction hot and reduces the time for the diode output to stabilize after turn-on. The RF output mode of the diode is reverse bias.

6) Replacement of several reference resistors associated with blackbody temperature measurement with precision (0.01%) resistors that have a low temperature coefficient.

7) *Simmering* of the Gunn oscillators while not in use. The two frequencies of the dual channel receiver are selected by turning on one or the other of two Gunn local oscillators that are combined into a common broadband balanced mixer. *Simmering* induces the Gunns to come to stable output power and frequency more quickly.

8) On-site regulation of the +15 voltage to the IF amplifier. The gain of op amps is sensitive to the +15 source; ground loops between the power supply and the amplifier could previously cause gain fluctuations.

9) Modifications to the software, including:

a) improved tip curve calibration algorithms and calibration acceptance criteria,

- b) more consistent observation sequences,
 - c) finite antenna beamwidth corrections,
 - d) corrections for the dielectric window in the WVR cover.
- 10) Azimuth steering mount.

11) Analysis and testing was performed on the antenna system (gaussian optical antenna, dielectric window, feed horn, waveguide) and system electronics to determine if thermal stabilization was necessary to instrument stability. It was found that the antenna system does not significantly change in loss or variable standing wave ratio (vswr, a measure of power reflected back toward the source) with ambient temperature (see §4.6.1). The digital electronics are likewise insensitive to ambient temperature changes. The analog circuitry that controls the noise diode current contains several resistors that had to be specified at a tight temperature tolerance (see §4.6.2).

The optimum sample (observation) time was determined to be about 1 second. This determination was made as follows.

Data were taken with WVR-1000 s/n 1 by pointing the radiometer mirror to the blackbody and taking successive measurements of the blackbody radiometrically for several different observation times. The results are shown in table 4.1. This instrument was a prototype, and did not have the stability enhancements of the WVR-1100 radiometer. The prototype was similar enough, however, to assess the optimum sample time of the subsequent WVR-1100.

Such measurements are insensitive to noise diode drift and noise and to gain drifts. This radiometer was in good tune, with:

$$F_{23.8} = 5.8dB$$

$$F_{31.4} = 5.5dB$$

The absolute values of the point-to-point differences were averaged, and a correction made for drift and temperature change during the period of the measurements.

These modifications allowed us to attain a resolving power, ΔT , of about 0.3 Kelvins and similar accuracy.

TABLE 4.1 Average Point-to-Point Noise of Blackbody Observations					
Sample Time	WVR Cycle Time	23.8 GHz p-p (K)	Norm. to 1 sec.	31.4 GHz p-p (K)	Norm. to 1 sec.
12.5 sec (Keihm)	2:32	.120K	.424K	.085K	.31K
	2:32		.79K		.81K
2.5 sec	1:06	.188K	.297K	.090K	.142K
0.5 sec	1:02	.365K	.258K	.223K	.157K

4.2 The resolving power, ΔT , of the Radiometrics WVR-1100 Radiometer

In Chapter 3 the theoretical resolving power of radiometers, ΔT , was defined. Because the various radiometer operating designs use different gain and offset referencing techniques, they also have differing theoretical resolutions. A quick overview of the various common radiometer designs and their salient characteristics is given here in tabular form (Table 4.2). All components of the radiometers are assumed lossless and nonreflecting (perfect vswr, perfect matches of components). The WVR-1100 radiometer uses a modified *noise adding* method, and its resolution will be subsequently derived.

The *ideal* radiometer in the table makes a single measurement of the target with a perfectly calibrated receiver. Because gain and offset measurements of a real (nonideal) receiver must be made, and because real receivers drift in gain and offset, there are error sources beyond the gaussian (statistical) sampling of the target temperature measurement. These sources are reflected in the additional terms in the expressions for ΔT in Table 4.2. There are other factors, unique to the construction of each radiometer, that are not expressed in this table; these

errors are due to nonideal characteristics such as insertion loss, emission of noise, and imperfect impedance matching of radiometer components and subsystems.

The WVR-1100 radiometer makes a series of measurements for each sky observation; blackbody reference for receiver offset determination, noise diode injection for gain determination, sky brightness, and blackbody reference again (to assess drift during the instrument cycle). In Table 4.3 I have derived and determined the uncertainties associated with each temperature measurement in this instrument cycle. Degradation of the signal- to-noise ratio of the receiver due to component losses, noise contributions, and mismatches is not considered here, but will be addressed later. Based on the sources of uncertainty in Table 4.3, the *theoretical resolving power* ΔT for the WVR-1100 is 0.20K. This is in agreement with the measured rms difference between two WVR-1100 receivers of 0.22K.

The uncertainties of T_{bb+nd} (ambient blackbody + noise diode temperature), T_{nd} (the gain reference), and T_{offset} add to the uncertainties in the T_{sky} in a leveraged manner because they determine the slope of the calibration line, and T_{sky} is determined by extrapolation. The magnitude of these multipliers is given in the third column and varies slightly with sky temperature.

The contribution of each measurement error source to the sky temperature measurement is the product of each measurement uncertainty multiplied by its leverage factor. Additionally, gain fluctuations and offset fluctuations that occur on the time scale of the measurement interval increase the uncertainty of each of the four measurements in each instrument cycle. These gain and offset fluctuations are caused by the instrument receiver amplifier and mixer, and are therefore laboratory measured. Gain and offset fluctuations on a time scale longer than the instrument cycle tend to be averaged out because measurements of gain and offset of the receiver span the sky measurement, and a linear interpolation is made. These two fluctuations are factors in the (sky) and (blackbody+noise diode) observations.

The following notation is used in Table 4.2 below:

T_{sky} = sky physical temperature (Kelvins)

T_{bb} = blackbody or reference physical temperature (Kelvins)

T_{nd} = increase in measured temperature due to noise diode (Kelvins)

T_{sys} = the effective temperature of the receiver, typically 700K for a receiver with RF amplification, and ranging up to 3000K for receivers without RF amplification. The measured T_{sys} for the WVR-1100 is about 800K in both channels.

TABLE 4.2 The Theoretical Resolving Power, ΔT , of Various Radiometer Types

Radiometer Type	Sensitivity, ΔT	System Description
Ideal	$\Delta T_{ideal} = \frac{T_{sys}}{\sqrt{B\tau}} = \frac{T_{rcvr} + T_{sky}}{\sqrt{B\tau}}$	error-free receiver
Total Power	$[1 + B\tau \left(\frac{\Delta Gain}{Gain}\right)^2]^{\frac{1}{2}} \Delta T_{ideal}$	error from gain fluct.
Dicke switched	$\left[2 \frac{(T_{rcvr} + T_{sky})^2 + (T_{rcvr} + T_{bb})^2}{B\tau} + \left(\frac{\Delta Gain}{Gain}\right)^2 (T_{sky} - T_{bb})^2\right]^{\frac{1}{2}}$	alternates, sky and reference
balanced Dicke	$2\Delta T_{ideal}$	$T_{bb} = T_{sky}$
Noise adding	$(1 + \frac{T_{sys}}{T_{nd}}) \Delta T_{ideal}$	injects known T incr.
Autocorrelation (U.of Mass.)	$\sqrt{3.5} \frac{T_{sky} + \sqrt{2} T_{rcvr}}{\sqrt{B\tau}} \simeq 1.8 \Delta T_{ideal}$	Spectral resolution via autocorrelation

The noise diode, which is used as a receiver gain reference, has an uncertainty in output power due to the fluctuations in white noise output power of the diode. The magnitude of such fluctuations are smaller than 10^{-4} in the 0.5 sec instrument sample time. Microwave noise diodes typically have a temperature coefficient of the output power that is smaller than 0.003dB/C. The noise diode mount in this receiver is held constant to within 1C to minimize output fluctuations due to ambient temperature changes.

The Gunn oscillators, microwave mixer, and amplifier have strong nonlinear performance as a function of temperature, but the data gathering scheme of the radiometer determines the gain and offset of the receiver during each instrument cycle. Provided that the physical temperature of the radiometer does not change significantly during a measurement cycle, these temperature coefficients can be ignored.

Because of a dearth of appropriate millimeter wave test equipment available to separately test each subsystem of the WVR-1100 radiometer, and because mismatches and other factors related to test equipment introduce yet another set of errors, methods were devised to characterize the radiometer subsystems by using the radiometer system intact. In many cases these devised tests were closer to physical constants and first principles than equivalent tests with external equipment. The terms in Table 4.3 that are measured (those not due to standard deviation of the power measurement) were determined as follows:

Receiver/mixer gain: Fluctuations in gain were determined by analysis of large data sets of tipping curves. Sky noise is removed by taking a large number of sky observations (sky noise + WVR noise) and a large number of blackbody observations (blackbody noise + WVR noise), Fourier transforming with the aid of a spectrum analyzer, and differencing the spectra. The difference represents the sky noise. Dark video (RF section off, amplifier on) and blackbody + noise diode video spectra are shown in Figure 4.2 below.

The bulk of such gain fluctuations lie below 1 Hz, requiring long-term measurements, so stability of the physical temperature of the receiver and of the reference targets during testing are important.

Table 4.3 below was constructed using typical values: a noise diode injection temperature of 200K, ambient (black body) temperature of 300K, and a sky temperature of 50K. These are all statistically independent measurement errors, and therefore add as the *square root of the sum of the squares* of each measurement uncertainty:

Receiver offset: Fluctuations in receiver offset are measured by pointing

the antenna mirror to the blackbody and taking successive measurements. Such a measurement is insensitive to gain fluctuations because the offset reference (the blackbody) and the radiometric target are the same temperature. All fluctuations are therefore due to offset drift. It is important to ensure that the receiver and blackbody target are very stable thermally to isolate other drifts. This is accomplished by operating the radiometer in a temperature controlled chamber.

TABLE 4.3 WVR-1100 Measurement Uncertainties

Measurement Type	Temperature Meas. Error	Leverage Multiplier	Magnitude
Sky	$\frac{T_{rcvr}+T_{sky}}{\sqrt{B\tau}}$ (0.018K)	1	0.018K
Blackbody	$\left[\left(\frac{T_{rcvr}+T_{bb}}{\sqrt{B\tau}}\right)^2 + \Delta T_{bb}^2\right]^{0.5}$ (~ .12K)	$\frac{T_{sky}}{T_{bb}}$ (~ 1)	0.12K
Blackbody +noise	$\left[\left(\frac{T_{rcvr}+T_{bb}+T_{nd}}{\sqrt{B\tau}}\right)^2 + \left(\frac{\Delta T_{nd}}{T_{nd}}\right)^2 + \Delta T_{bb}^2\right]^{0.5}$ (~ .14K)	$\frac{T_{bb+nd}-T_{sky}}{T_{bb}-T_{sky}}$ (~ 1.1)	~ 0.15K
Gain reference	ΔT_{nd} (~ .02K)	$\frac{T_{nd}}{T_{bb}-T_{sky}}$ (~ 0.8)	10^{-4} (~ 0.02K)
Receiver gain	$\frac{\Delta Gain}{Gain} \times T_{sys}$ (~ .09K)	1	~ 0.09K
Receiver offset	ΔT_{offset} (~ .07K)	0.5	0.035K
1 complete instrument cycle	vector addition of above uncertainties		$\Delta T = 0.20K$

Noise diode: The noise diode repeatability and drift were determined by taking rapid samples of the incremental receiver voltage measured by turning the

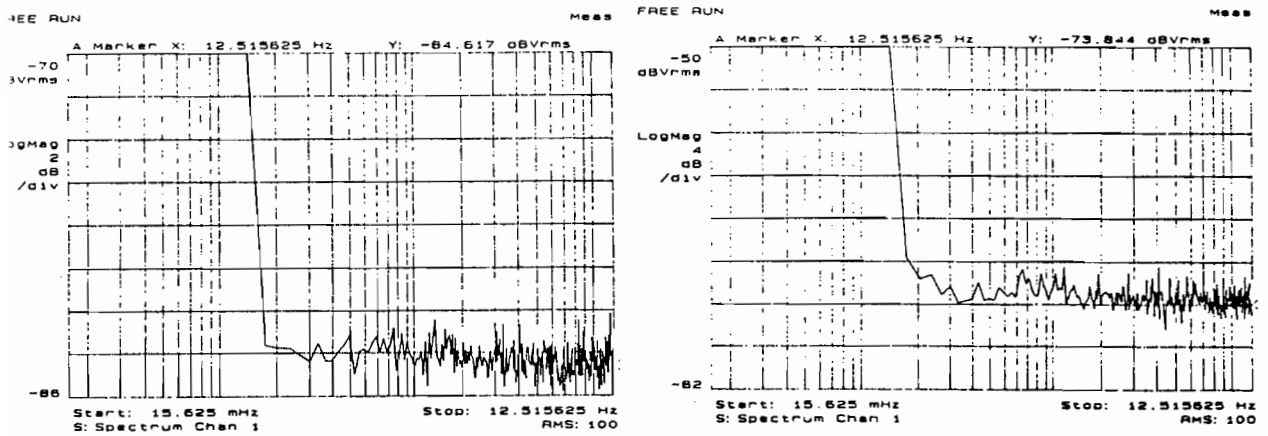


FIGURE 4.2 Noise spectra of the water vapor radiometer. The left panel is the 65 dB gain amplifier and detector noise; the right panel is the receiver noise with the antenna viewing an ambient blackbody and with the noise diode injection on. Differencing such spectra yields the power contribution of separate components of the receiver system.

noise on. In addition to the noise (repeatability) and drift, repetitive fast-sample data from the first several seconds of turn-on were stacked, and the output as a function of time just after turn-on was sampled. This measurement was made to determine how long to wait after turn-on before using the noise as a reference. These turn-on measurements prompted us to flow high current through the noise diode in the forward direction when not needed as a noise source, so that the diode junction is maintained at high temperature.

The noise diode drift measurements also contain the gain drift of the receiver. Fourier transforming long data sets of both spectra and differencing yields the spectrum due solely to the noise diode, thereby separating the gain and noise diode drifts.

Blackbody: Worst-case manufacturer's (Analog Devices AD592CN) specifications on the temperature sensors and blackbody absorber were used to establish ΔT_{bb} . The two temperature sensors have a bias whose rms average can be as great as 0.3K; this bias can be calibrated out.

Experimental verification: Provided that the blackbody reference of the radiometer can be demonstrated to be stable, or at least to be changing slowly in time relative to the WVR observation cycle time, the rapidly repetitive blackbody observations can be used to measure ΔT of the radiometer. The rms noise of these measurements reflects the resolving power of the radiometer, ΔT . This technique will also reveal drifts in the instrument offset. This measurement was periodically made, and typically yields rms values slightly under 0.3K.

Tests were also run to again assess instrument resolution and to check the consistency of the instrument across ranges of sky brightnesses and ambient temperatures. Two WVR-1100 radiometers were run side-by-side and in cadence. They used the sky as a common reference target. The sky is noisier than the blackbody reference, having a rather predictable power spectrum induced by water vapor features. The receiver signal is therefore expected to include this sky noise with the receiver noise of measurement. Clear sky comparisons show about 0.4K rms differences (0.28K attributable to each radiometer measurement).

A curious feature of sky noise was revealed through these intercomparison tests. At 100 feet separation of the two radiometers, the time series of the data exhibited some correlation, as expected. But the higher frequency (shorter period) correlations were present for some observation periods (sometimes with some short time lag), and absent for others. My supposition was that small water vapor features in the boundary layer were floating through the field of view of the antennas, which were sometimes oriented crosswind and sometimes downwind from each other. So the radiometers were moved to a separation of 35 feet. This repositioning increased the correlation and, within the resolution of the data set, removed the time lags. The implication is that there are water vapor features on the scale of 100 feet and at altitudes below about 500 feet. Longer observation times in a better-planned experiment might better define the scale, altitude, population, and occurrence of such features.

4.3 Uncertainty in phase path delay as a function of uncertainty in brightness

Utilizing the definition of mean radiating temperature, we can define atmospheric opacity for a tenuous medium as:

$$\tau = \ln\left(\frac{T_{mr} - T_c}{T_{mr} - T_B}\right) \quad (4.1)$$

Differentiating w.r.t. T_B , we obtain:

$$d\tau = \frac{dT_B}{T_{mr} - T_B} \sim \frac{\delta T_B}{T_B} \quad (4.2)$$

Water vapor can be inferred from the Radiometrics radiometer by utilizing a two-frequency retrieval algorithm, approximated by the expression:

$$water\ vapor(cm) \simeq 21\tau_{23.8} - 12\tau_{31.4} \quad (4.3)$$

The coefficients are only approximate. The radio phase path delay is approximately 6.5 times the vapor burden:

$$radio\ phase\ path\ delay\ (cm) = 6.5 \times (water\ vapor) \quad (4.4)$$

Assuming the uncertainties in the two measurement channels are not correlated, we can estimate the uncertainty in phase path delay as:

$$\Delta(path\ delay)(cm) = 6.5 \times \sqrt{\left(\frac{21\Delta T_{B23.8}}{T_{mr} - T_{B23.8}}\right)^2 + \left(\frac{12\Delta T_{B31.4}}{T_{mr} - T_{B31.4}}\right)^2} \quad (4.5)$$

The uncertainty in τ , and therefore in phase path delay, increases in brighter skies for a given uncertainty in brightness measurement.

Note that, by the manner in which the measurements are taken, uncertainties due to gain fluctuations ΔG in the receiver are only slightly affected by sky brightness T_b . This can be shown by writing the radiometer equation:

$$T_B = T_{bb} - G^{-1}(N_{bb} - N_{sky}) \simeq T_{mr} - G^{-1}(N_{bb} - N_{sky}) \quad (4.6)$$

(T_{mr} can be approximated as 95% of the surface temperature, which is approximately T_{bb}) So:

$$\Delta(\text{path delay})(cm) \simeq 6.5 \times \sqrt{\left(\frac{21\Delta G_{23.8}}{N_{bb23.8} - N_{B23.8}}\right)^2 + \left(\frac{12\Delta G_{31.4}}{N_{bb23.8} - N_{B31.4}}\right)^2} \quad (4.7)$$

Using representative sky brightnesses of 30 and 15 K for the two channels, and assuming an equal error in each of the two radiometer channels, we obtain:

$$\begin{aligned} \Delta(\text{path delay})(cm) &= 6.5 \times \sqrt{\left(\frac{21}{T_{mr} - T_{B23.8}}\right)^2 + \left(\frac{12}{T_{mr} - T_{B31.4}}\right)^2} \Delta T_B \\ &= 0.654 \Delta T_B \end{aligned} \quad (4.8)$$

Or, a 0.3K error yields a 2 mm error in path delay, consistent the observed value of 2.05 mm (2.9 mm rms between two WVRs) from intercomparisons described in §4.5.1. The uncertainty in the vertical GPS position from this *single measurement* noise is about 3 times the zenith path delay uncertainty, or about 6 mm . Averaging of successive measurements diminishes this noise source.

4.4 WVR-1100 Receiver Noise Figure

The Radiometrics receiver can be modeled as a series of two-port devices, each with a gain and insertion loss. These losses and gains contribute to the effective noise of the receiver. For example, waveguide has a finite resistive loss which causes temperature dependent microwave emission into the receiver system. A typical waveguide ohmic loss of 0.01 dB/cm can add as much as 2K/ cm to the receiver temperature, depending upon the waveguide construction and plating. Such emissions, normalized to a physical temperature of 290K, are expressed as *noise figure*, labelled F .

The figure of merit of a two port device (such as a microwave radiometer) is *noise figure*. The fundamental measurement of noise figure is accomplished

by measuring the output signal of the device while referenced to two different input sources. For a radiometer, these sources are two targets or injected signals of known temperature. The ratio of the two resultant signal voltages is defined as Y .

The effective input noise temperature for such a two-port device is written as:

$$T_e = \frac{T_h - YT_c}{Y - 1} \quad (4.9)$$

where T_h (T_c) is the hotter (colder) of the two injected references.

The WVR-1100 radiometer uses an ambient target for T_c and adds a noise signal, T_{nd} , to this ambient signal for T_h . So for this radiometer the expression for T_e reduces to:

$$T_e = \frac{T_{nd}}{Y - 1} - T_c \quad (4.10)$$

The ambient reference (T_c) and *ambient+injected noise* reference (T_c+T_{nd}) establish gain and offset of the receiver. T_{nd} is measured using atmospheric tipping curves.

The Noise Figure F is defined as:

$$F(dB) = 10 \log \left(\frac{T_e + T_0}{T_0} \right) \quad (4.11)$$

where T_0 is the *reference source temperature* of 290K. If T_c , the ambient temperature, is approximately 290K, we can write:

$$F(dB) = \log \left(\frac{T_e + T_c}{T_c} \right) = \log \left(\frac{T_{nd}}{(Y - 1)T_c} \right) \quad (4.12)$$

This approximation of the ambient temperature is valid within 0.15dB of noise figure F for a radiometer receiver temperature of 750K, and a 10K difference in a range between ambient and 290K. 750K is typical for the WVR-1100 radiometer, which does not use a microwave amplifier before the mixer, but rather amplifies the downconverted signal after the mixer.

Receiver performance is optimized by minimizing this Noise Figure; an ideal device has a Noise Figure of 0. In practice, F is minimized by maximizing Y .

A rough rule of thumb to determine the change in Noise Figure F due to a small change in Y (useful in tuning the radiometer) is:

$$dF(dB) = d\left(4.343\ln\left(\frac{T_{nd}}{(Y-1)290K}\right)\right) = -4.343\frac{dY}{Y-1} \quad (4.13)$$

Or, for each 0.1 dB change in F , the value of $(Y-1)$ must change by 2.3%

The approximate (estimated or measured) losses of the WVR-1100 receiver components are shown in Table 4.4, and sum to a total noise figure of about 5.7 dB. Such analysis is valuable in determining which components of the receiver contribute most to receiver noise, and therefore require the most attention to construction.

The measured noise figure of the WVR-1100 receiver is about 5.5 dB, in good agreement with the estimated sum. This measurement is accomplished by pointing the antenna mirror to the black body reference and measuring the receiver output with and without a known temperature injected into the antenna waveguide. The known temperature is provided by the noise diode, the injection temperature of which is determined from tipping curves. Because the noise is injected behind the antenna system, this measurement does not include the losses of the microwave window, feed horn, antenna lens, and mirror, the total losses of which are about 0.7 dB.

The effective receiver temperature is:

$$T_e = \frac{T_h - YT_c}{Y - 1} = (10^{F(dB)/10} - 1) \times 290K \quad (4.14)$$

For a noise figure of 5.5dB, the receiver effective temperature is 740K.

TABLE 4.4 WVR-1100 Component Losses		
Receiver Element	23.8 GHz Insertion Loss (dB)	31.4 GHz Insertion Loss (dB)
teflon window	0.01	0.01
mirror	0.01	0.01
gaussian antenna	0.90	0.70
waveguide	0.12	0.12
crosscoupler	0.10	0.10
antenna isolator	0.45	0.55
mixer+amplifier (amplifier gain)	4.00 (+65.5)	4.00 (+65.5)
Total Noise Figure	5.69	5.59

Because the WVR-1100 radiometer uses common receiver components for both the 23.8 and 31.4 GHz frequencies, optimization of the receiver noise figure is a matter of tradeoff between the two operating frequencies. An optimum set of parameters for one frequency is not the optimum set for the other, so a slight penalty in performance is suffered by compromise. One of the variables in this tuning procedure is matching of the RF port of the mixer to the antenna waveguide. This match is a function of the positioning of the mixer crossbar and diodes, with final tuning accomplished by tuning the port with Teflon material to change capacitance (impedance match) of the RF port.

Another variable is the local oscillator drive level to the LO port of the mixer. Balanced mixers typically have a minimum conversion loss at 8 to 10 dBm of LO drive. The optimum LO drive is determined by attenuating the LO drive with a blade attenuator while turning the noise diode on and off, and observing the Y value, the ratio of (signal with noise on)/(signal with noise off).

4.5 Demonstration of accuracy and precision; WVR intercomparisons and LN2 target tests at Boulder

4.5.1 Intercomparison

To ascertain the effectiveness of the WVR modifications, and therefore the resolution and accuracy of the radiometer, several tests were conducted at Boulder. The first test was an intercomparison between two radiometers at Boulder. The two instruments were placed side-by-side (10 meter separation), calibrated with tipping curves, and then commanded to stare vertically. These several tests spanned several days in late summer, and included cloudy and clear conditions. The data are shown in Figure 3.2.

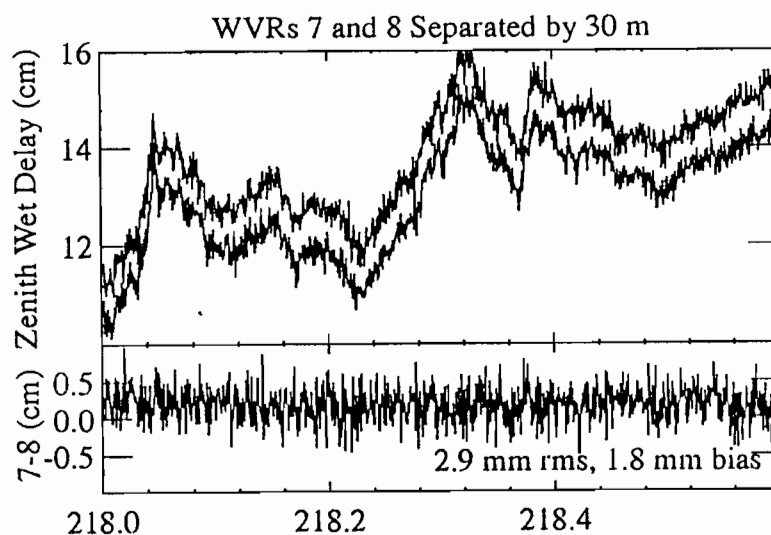


FIGURE 4.3 Intercomparison of WVR7 and WVR8. The measured rms difference in water vapor path delay measurements was less than 3 mm for the two instruments (2 mm for each WVR), consistent with the 2 mm calculated from conservatively estimated instrument errors and resolution.

Path delays were calculated from these data using line shape models prior to the Keihm modification [1991]; the more recent line shape models would have

made little difference in the intercomparisons. Fifteen hours of intercomparison under rather active skies (30% variation in water vapor) yielded a 1.8 *mm* bias in inferred water vapor induced path delay between the two instruments, and an rms difference of 2.9 *mm*.

These intercomparison tests speak to the stability and resolution of the WVRs but not to absolute accuracy. To determine absolute accuracy, a cryogenic blackbody target was constructed. A target well separated in temperature from ambient was required to determine gain stability as the ambient target within the WVR is used to establish a reference offset.

4.5.2 Verification of the tip curve calibration of the radiometer

The radiometer measurement is based on measurements of radiometer voltage signals while the antenna is at two known temperature references. These two references are the *blackbody target*, about 300K and the *blackbody+noise diode*, about 500K. The receiver response is assumed linear, and is crudely verified by measuring the voltage added to the receiver by the noise diode while the antenna is at the blackbody reference 300K) and at the sky (about 20K). For measurements, the *antenna temperature vs. receiver voltage* relation is extrapolated to the range of observables (sky temperatures). This extrapolation is roughly equal to the span of the two references, and is therefore very sensitive to errors in the reference measurements and to nonlinearity in the receiver. This nonlinearity across the dynamic range of the receiver is due to amplifier compression and non square law detector behavior. Because of this nonlinearity, a reference in the range of the observables is needed to assess linearity of the receiver across the range of observations. A cryogenic target was therefore conceived and constructed.

The cryogenic target was built consisting of Eccosorb convoluted blackbody foam placed, convolutions down, in a polystyrene foam cooler. The foam is immersed in liquid nitrogen. The boiling point of the LN2 defines the internal target temperature, to which small corrections are added for the liquid-air in-

terface and any windows between the radiometer and the target. The original cryogenic target concept was to have the field of view of the upward looking radiometer captured by curved aluminum reflectors and directed downward into an open-mouthed Dewar flask. It is preferable to have the radiometer looking upward such that any sidelobes would detect the sky rather than at ambient (terrestrial) sources; the offset between cryogenic target and sidelobe view, and therefore the resultant bias, would be smaller and subject to smaller error when corrected for. This target required some care, however, to avoid condensation and formation of the fogs of water vapor, CO₂, oxygen, and other atmospheric constituents in the field of view of the radiometer. Additionally, such condensed gases could mix with the LN₂ and raise its boiling temperature, degrading the accuracy of our reference temperature. Placing a dual-pane microwave window over the Dewar, and purging the Dewar volume with dry nitrogen gas before the addition of LN₂, would minimize but not eliminate these problems.

An alternate target configuration was conceived wherein the WVR would look upward through the bottom of a polystyrene (Styrofoam) container that is transparent to microwaves. This scheme would eliminate most of the above difficulties and uncertainties. The low tangent loss of Styrofoam was measured at the two radiometer frequencies by placing a thick slab in and out of the WVR field of view while the antenna was at a cold target (sky). This exercise produced a 0.3K increase at 23.8 GHz and 0.4K at 31.4 GHz for a slab of the thickness that was employed in the target; this ratio of temperatures matches the wavelength-to-thickness dependence of insertion loss for small loss tangents. With a linear gradient of temperature from 77K to ambient across the foam slab the actual temperature contribution of the foam with liquid nitrogen at one surface is one half of these values.

As shown in Figure 4.4, saddle was constructed to sit on top of the WVR and support a cooler of this Styrofoam material above the WVR. The saddle was constructed with metal lining and blinders such that side lobes would be reflected and terminate in the cold target. An aluminum plate was placed above

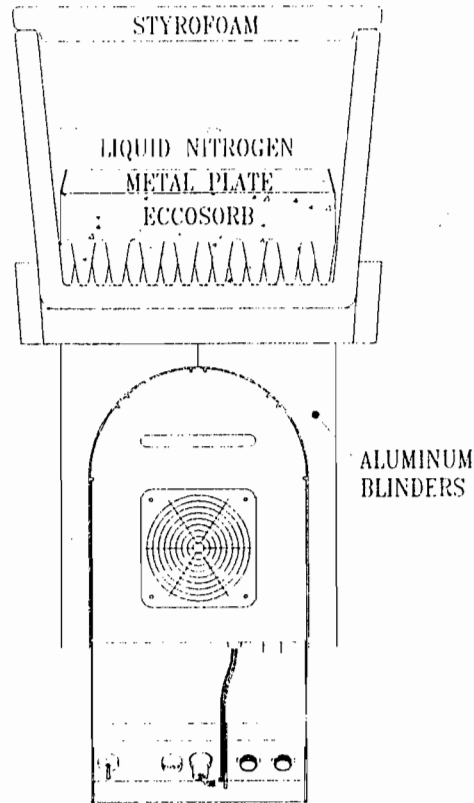


FIGURE 4.4 The cryogenic blackbody target. The temperature of the liquid nitrogen, and therefore of the blackbody, is known to within 0.05K. Metal blinders direct the field of view of the side lobes into the blackbody to eliminate offset errors. An aluminum plate shields from external radiation and doubles the effective path length through the blackbody absorber.

the foam to minimize ambient signal from penetrating the foam from above.

In these tests the cryogenic target was placed over the radiometer for about 4 hours. After 1.2 hours, moisture condensation on the underside of the cooler began to raise target temperatures, so only the first 1.2 hours of data were usable. The dew blower fan, subsequently incorporated to keep the microwave window free from dew, would have forestalled this condensation problem. But a longer period of observation would not enhance the value of this measurement except as yet another measure of drift stability of the WVR.

The orthogonal reflection contribution at the lower surface of the liquid nitrogen was calculated from the dielectric coefficient of LN2 at 0.00724K/K, or 1.62K for reflections to sources at 300K. The boiling point of the liquid nitrogen, and therefore the internal target temperature, was calculated from NIST tables for the atmospheric pressure. For convenience, an expression, accurate to 0.05K from 700 mb to 1030 mb, was obtained by a regression fit to the NIST tables:

$$LN2 \text{ boiling temperature } T(K) = \frac{68.23}{68.21} + 0.009037 \times P(mb) \quad (4.15)$$

Closed cell blackbody foam was tried as the blackbody absorber, but nitrogen gas bubbles from boiling of the LN2 would accumulate under the foam, causing scintillations in the signal of the upward-looking radiometer. The open cell convoluted foam solved this problem by allowing gases to flow through the foam.

TABLE 4.5 WVR-1100 Cryogenic Target Measurements				
	23.8 GHz (K)		31.4 GHz (K)	
liquid nitrogen at 849 mb	75.88		75.88	
LN2 surface reflection	1.62		1.62	
Styrofoam contribution	0.0007 K/K	0.15	0.0009 K/K	0.2
Calculated target temperature	77.65		77.70	
Mean measured temperature	77.67		77.94	
Difference of mean and calculated	+0.02		+0.24	
rms difference	0.23		0.33	

*7 verified
3/5/94
for 2 cm
Styrofoam
Colder*

4.6 WVR-1100 receiver gain temperature coefficient

Although the WVR-1100 water vapor radiometer microwave RF receiver is temperature stabilized to within several tenths of a Kelvin, the radiometer has a residual gain dependence upon ambient temperature. The earlier version of this radiometer, the WVR-1000, was not temperature stabilized, and exhibited a much more significant temperature dependence than the WVR-1100. Tempera-

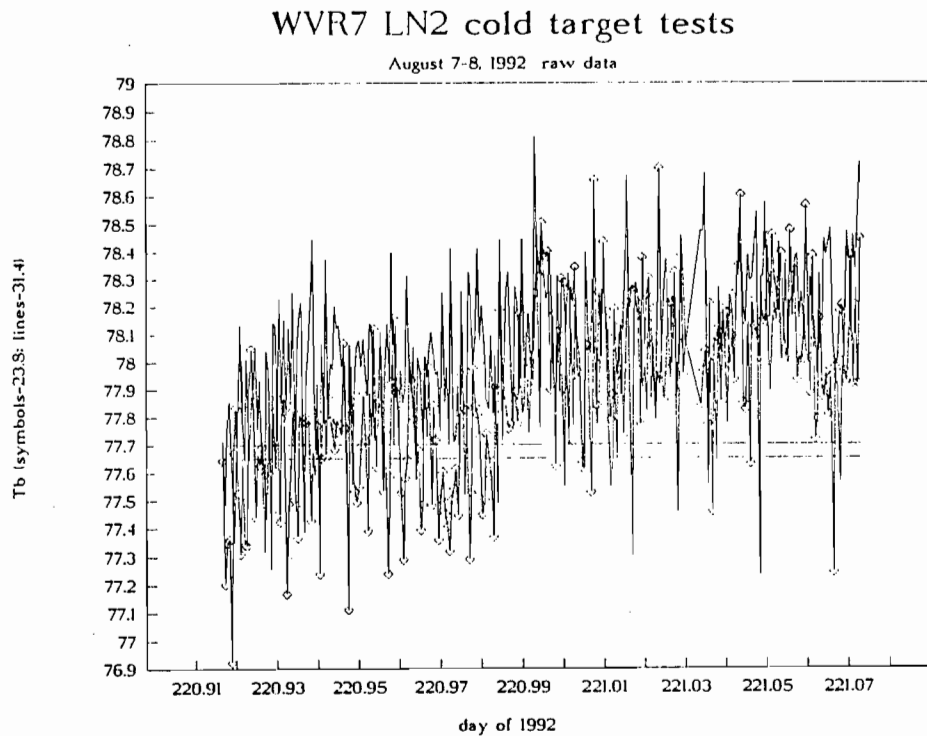


FIGURE 4.5 WVR observations of the cryogenic target. The temperature rise at day 221.0 is due to moisture condensation on the underside of the target. The horizontal lines at 77.65 and 77.70K are the calculated target temperatures for 23.8 and 31.4GHz.

ture stabilizing of the WVR-1100 eliminated the following sources of temperature dependence in the WVR-1000:

- 1) The RF output of the Gunn local oscillators, which diminishes with increased physical temperature, while the mixer that they drive requires more power with increasing temperature to maintain the maximum noise figure. The conversion loss of the mixer was therefore a function of physical temperature.

- 2) The isolation and insertion loss of the dual-junction antenna isolator are slightly temperature dependent.

- 3) The noise diode cross coupler, due to the change in physical dimensions and conductivity with temperature.

4) The gain temperature coefficient of the 65 dB gain amplifier.

5) Critical resistors with temperature coefficients in the measurement and voltage control circuits, which were replaced with resistors of lower temperature coefficients. These resistors are located on PC boards that are not temperature stabilized, and were associated with measurement of the blackbody temperature, and with noise diode current control.

Stabilizing the receiver eliminated the above drifts; the WVR still, however, exhibited a temperature coefficient. The temperature coefficient of the temperature stabilized WVR-1100 receiver is smaller and much more consistent from WVR to WVR than the previous model (WVR-1000), and does not appear to change with instrument aging and abuse. In an attempt to identify the origin of the remaining temperature dependence, an analysis was undertaken to see if the coefficient could be predicted theoretically from changes in waveguide hardware with temperature. Measurements were also made by heating various components of the WVR system and measuring system gain with a LN2-ambient targets system. Analyses of the systems electronics were also performed to determine if the temperature coefficients of any of the components could affect the gain of the instrument.

4.6.1 Antenna system analysis

The antenna system components that could contribute to the temperature dependence are (from the sky inward):

1) Etalon effects of the microwave window and RexoliteTM lens

a) **The microwave window.** The window is a very low density closed cell polyethylene foam, consisting mostly of air. As the ambient temperature, and therefore the air pressure in the cells, changes, the foam changes thickness. The total dielectric absorption does not change, but because there is reflection from the dielectric at the inner and outer surfaces, there can be slight destructive interference. This is analogous to a Fabrey-Perot etalon.

The plano-parabolic Rexolite lens. As with the polyethylene foam window, the lens changes in thickness with changing temperature, and the etalon effect therefore changes transmission. This dimensional change, described the thermal coefficient of the lens material (about 80×10^{-6}), is much smaller than that of the gas in the polyethylene foam (about 800×10^{-6}), but the index of refraction is much greater (1.6) than the polyethylene foam (1.06). The temperature dependent etalon losses for these two elements are therefore of the same magnitude. This lens has an *f stop* of $f = 1.0$, and therefore cannot be treated with thin lens theory. The Rexolite lens etalon effects are therefore very hard to model. Their magnitudes can, however, be estimated. From prior analysis we can show that the variation in the etalon loss with temperature is less than 2×10^{-6} K/K. I will show that the conductivity and cutoff losses are about 200 times larger for the waveguide described below than for the etalon losses of the polyethylene window and for the Rexolite lens. I will also show that the conductivity and cutoff coefficients are insignificant; the smaller etalon effects of the window and lens can therefore be ignored and are therefore not investigated here. The feed horn is complex geometrically and is not amenable to modelling. It is also subject to small manufacturing variances that manifest themselves as small variations in the electrical performance of the feed horn. Feed horn effects are therefore not modeled, but rather measured.

2) Temperature dependent dielectric effects of the microwave window and Rexolite lens.

The absorption of the lens and foam window are bulk effects; the total absorption is proportional to the total material mass along the propagation path. It is therefore independent to thickness change due to thermal expansion to first order.

Note that it is not practical to thermally stabilize the polyethylene window and the Rexolite lens because they must remain unobstructed, are exposed to the cold sky, and therefore lie in radiative-convective equilibrium at a temperature somewhere between ambient and sky. The only feasible way to heat them is

with forced air heat.

3) The corrugated feed horn and the waveguide that joins the feed horn and the temperature stabilized RF receiver. Because they are amenable to accurate modeling, this paper focuses on the waveguide sources of temperature coefficient. The WR34 waveguide used in Radiometrics radiometers is shown to have a temperature coefficient that originates, in part, from the frequency cutoff and conductivity characteristics of the WR34 waveguide in the non-stabilized antenna path of the instrument. The following analysis derives the temperature coefficient of this section of waveguide, one end of which is at ambient, and the other end which is at the stabilized temperature of the RF receiver.

The received sky signal (called antenna temperature) T_A received at the antenna is attenuated to T'_A by losses in the waveguide components from the antenna to the temperature stabilized microwave receiver:

$$T'_A = T_A e^{-\alpha(T) \cdot L} \quad (4.16)$$

where L is the length of waveguide undergoing temperature change, and α is the temperature dependent loss coefficient due to cutoff. This attenuation can be treated as an effective change in the gain coefficient g of the receiver, because it reduces the sensitivity of the receiver. The radiometer equation for output voltage V_o of a radiometer with no antenna path losses is:

$$V_o = V_{sys} + g_o T_A \quad (4.17)$$

where V_{sys} is the receiver noise in the absence of antenna signal, due to electronic and component noise. For a lossy antenna path, we can write:

$$V_o = V_{sys} + g_o T_A e^{-\alpha(T)L} + g_o T_{wg} (1 - e^{-\alpha(T)L}) \quad (4.18)$$

where T_{wg} is the receiver noise contribution due to the waveguide emission. V_{sys} and $g_o T_{wg} (1 - e^{-\alpha(T)L})$ are receiver offsets, independent of antenna signal; this

offset is established as part of each observation cycle of the WVR-1100. We can therefore ignore these offsets and write the gain variation due to attenuation as:

$$\frac{g}{g_o} = e^{-\alpha(T) \cdot L} \sim -\alpha(T)L \quad (4.19)$$

where, because these gain changes are small ($\sim 10^{-4}/K$), I have expanded the exponent. The gain of the receiver is therefore modulated by the ambient temperature. I shall now establish the theoretical temperature coefficient of gain due to the waveguide components that are not temperature stabilized.

The cutoff wavelength $\lambda_c = 2a$ for WR34 waveguide is 1.72 cm (a is the major dimension of the waveguide cross section). The frequency f_c is $f_c = c/2a = 17.34GHz$. The cutoff is not abrupt; the group velocity decreases to zero, and the waveguide loss α increases, as this frequency is approached from above. Because the brass waveguide changes dimension and conductivity with temperature, the cutoff frequency and attenuation change with temperature. The WVR-1100 uses brass WR34 plated with about 50 microns of gold propagating in TE_{01} mode. For frequencies above the cutoff frequency the TE_{01} attenuation per unit length due to cutoff and finite conductivity of the waveguide is (see Jackson, 1975):

$$\begin{aligned} \alpha(\text{nepers/length}) &= \frac{1}{\eta} \sqrt{\frac{\pi f \mu}{\sigma}} \frac{1}{\sqrt{1 - \left(\frac{f_c}{f}\right)^2}} \left[\frac{1}{b} + \frac{2}{a} \left(\frac{f_c}{f}\right)^2 \right] \\ &= \frac{1}{\eta} \sqrt{\frac{\pi f \mu}{\sigma}} \sqrt{1 + \frac{c^2}{4a^2 f^2 - c^2}} \left[\frac{1}{b} + \frac{c^2}{2a^3 f^2} \right] \end{aligned} \quad (4.20)$$

where

$$\eta = \sqrt{\frac{\mu_0}{4\pi}} = 376.7 \text{ ohms, the impedance of free space}$$

$$\mu = 4\pi \times 10^{-7} \text{ henrys/mho}$$

$$f_c = c/2a$$

$$\sigma \simeq 1.57 \times 10^7 \text{ mhos/meter for brass}$$

and a and b are the major and minor inside dimensions of the waveguide.

The temperature dependence of this attenuation is due to the linear expansion coefficient of the waveguide material; as the temperature increases, the dimensions of the waveguide increase relative to the wavelength, lowering the cutoff frequency. The conductivity also has a temperature dependence, being roughly proportional to the inverse absolute temperature. The WVR temperature coefficients of the gain of the receiver system are called $C_{nd23.8}$ and $C_{nd31.4}$, and are defined as *(Kelvins change in the noise diode injection temperature T_{nd})/(Kelvins change in ambient temperature)*. T_{nd} is the increase in measured antenna temperature realized by turning on a broad-band noise diode that injects white noise into the antenna waveguide via a Moreno 27dB crossguide coupler. The temperature coefficients C_{nd} are established by performing tipping curve calibrations across a range of ambient temperatures, and regression fitting a linear dependence of T_{nd} vs. ambient temperature.

$$C_{nd} = \frac{dT_{nd}}{dT} = T_{nd} \frac{dg}{dT} \quad (4.21)$$

Although the change in receiver gain is seen in the tipping curve fundamental calibrations, for simplicity it is instead applied in the correction algorithm to the stable noise diode reference that carries the gain calibration, rather than being applied to the sky data. Decreases in receiver sensitivity due to antenna path losses are therefore reflected as *increases* in the internal noise diode calibration level. If we assume that all of this temperature coefficient comes from temperature dependent waveguide losses α , we can write:

$$C_{nd} = \frac{dT_{nd}}{dT} = T_{nd} L \frac{d\alpha}{dT} \quad (4.22)$$

The temperature dependence of waveguide absorption due to dimensional and conductivity changes is:

$$\frac{d\alpha}{dT} (\text{nepers/length} \cdot K) = \frac{\partial\alpha}{\partial a} \frac{da}{dT} + \frac{\partial\alpha}{\partial b} \frac{db}{dT} + \frac{\partial\alpha}{\partial\sigma} \frac{d\sigma}{dT}$$

$$= \alpha \left\{ \left[\frac{1}{a \left(\left(\frac{f}{f_c} \right)^2 - 1 \right)} + \frac{3}{a \left(1 + \frac{a}{2b} \left(\frac{f}{f_c} \right)^2 \right)} \right] \frac{da}{dT} + \frac{1}{b \left(1 + \frac{2b}{a} \left(\frac{f_c}{f} \right)^2 \right)} \frac{db}{dT} + \frac{1}{2\sigma} \frac{d\sigma}{dT} \right\} \quad (4.23)$$

Notice that $\frac{1}{a} \frac{da}{dT}$ and $\frac{1}{b} \frac{db}{dT}$ are the thermal expansion coefficients; the coefficient of linear expansion for the brass waveguide material is:

$$k_{brass} = 20 \times 10^{-6} = \frac{1}{a} \frac{da}{dT} = \frac{1}{b} \frac{db}{dT} \quad (4.24)$$

The temperature dependence of conductivity σ for brass is (the 50 micron gold plating is only to prevent oxidation, and does not affect the conductivity):

$$\frac{d\sigma}{\sigma dT} = -.002/C \text{ (.004/C, aluminum feed horn)} \quad (4.25)$$

The temperature coefficients can therefore be expressed as:

$$\begin{aligned} C_{nd} &= T_{nd} L \frac{d\alpha}{dT} \\ &= T_{nd} L \alpha \left\{ \left[\frac{1}{\left(1 - \left(\frac{f}{f_c} \right)^2 \right)} - \frac{3}{\left(1 + \frac{a}{2b} \left(\frac{f}{f_c} \right)^2 \right)} - \frac{1}{\left(1 + \frac{2b}{a} \left(\frac{f_c}{f} \right)^2 \right)} \right] k_{brass} - \frac{d\sigma}{2\sigma dT} \right\} \\ &\simeq T_{nd} L \alpha \left\{ \left[\frac{2}{\left(\left(\frac{f_c}{f} \right)^2 - \left(\frac{f}{f_c} \right)^2 \right)} + \frac{3}{\left(1 + \left(\frac{f}{f_c} \right)^2 \right)} \right] \times 0.00002 + 0.001 \right\} \quad (4.26) \end{aligned}$$

for $a \simeq 2b$, the typical aspect ratio for rectangular waveguide.

For WR34 waveguide in brass, $a = 0.340$ inches, $b = 0.170$ inches, and conductivity $\sigma = 1.57 \times 10^7$ mhos/meter. Table 4.6 below summarizes the theoretical temperature coefficients for this waveguide size.

TABLE 4.6 Sources and Magnitudes of WR34 Waveguide Losses and Temperature Coefficients		
Quantity	23.8 GHz	31.4 GHz
α , Nepers/inch	.00270	.00217
$C_{nd}/inch$, K/K-inch		
cutoff effect	-0.000028	-0.000014
conductivity effect	+0.000544	+0.000444
total	+0.000516	+0.000430

Additional temperature dependence could come from the corrugated feed horn, which is of WR34 scale, 4" long, and made of aluminum. The conductivity of aluminum is about 2.5 times that of brass, and the temperature coefficient of the conductivity of the feed horn is $\sigma = -.0039/C$, about twice that of the brass waveguide. I would expect the feed horn to have a coefficient roughly four times that of the brass waveguide; the sum of the waveguide and feed horn coefficients does not account for the observed temperature dependence and is of the opposite sign.

The above investigation of temperature dependence of gain in the antenna subsystem due to waveguide cutoff and to conductivity does not explain the gain temperature coefficient that the WVR-1100 exhibits (up to 5×10^{-4}). An experiment wherein the gain of the WVR was measured as the feed horn was heated revealed that the temperature dependence might be due to changes in feed horn properties. The change in conductivity of the aluminum feed horn has been shown to be negligible. The effect of the change in vswr with temperature is therefore investigated below. Subsequent to the below analysis the experiment was repeated and a faulty waveguide component was found.

The variable standing wave ratio is defined as a function of the power reflection coefficient by:

$$vswr = \frac{1 - \Gamma}{1 + \Gamma} \quad (4.27)$$

and conversely:

$$\Gamma = \frac{1 - vswr}{1 + vswr} \quad (4.28)$$

A propagating signal experiences a reflection at each change in impedance (mismatch) that it encounters. For the feed horn-isolator subsystem there are multiple reflections between the two components that can result in standing waves and that lose power due to transmission at each impedance change. For this interaction (with feedhorn to waveguide power reflection coefficient Γ_h and isolator antenna port reflection coefficient Γ_i), the antenna signal is diminished as it passes through these components by:

$$\begin{aligned} I &= I_o(1 - \Gamma_h)(1 - \Gamma_i)(1 + \Gamma_i\Gamma_h \cos\phi + (\Gamma_i\Gamma_h \cos\phi)^2 + (\Gamma_i\Gamma_h \cos\phi)^3 + \dots) \\ &= I_o(1 - \Gamma_h)(1 - \Gamma_i)e^{\Gamma_i\Gamma_h \cos\phi} \end{aligned} \quad (4.29)$$

where the phase angle $\phi = \frac{4\pi l}{\lambda}$; l is the phase distance between the reflectors.

The temperature dependence of gain (loss) upon the feed horn vswr and waveguide length temperature coefficient is:

$$\frac{dI}{I} = \left(\Gamma_i \cos\phi - \frac{1}{1 - \Gamma_h} \right) \frac{\partial \Gamma_h}{\partial T} dT - \Gamma_i \Gamma_h \sin\phi \frac{d\phi}{dT} dT \quad (4.30)$$

Now,

$$\frac{d\phi}{dT} = \frac{4\pi}{\lambda} \frac{dl'}{dT} = \frac{4\pi l'}{\lambda} \left(\frac{1}{l'} \frac{dl'}{dT} \right) \quad (4.31)$$

where l' is the length between the reflections that is changing with temperature; e.g., the portion of the path that is not temperature controlled. Note that

$$\frac{1}{l'} \frac{dl'}{dT} \quad (4.32)$$

is the thermal coefficient of expansion for the brass (aluminum) waveguide (feed horn) = 20×10^{-6} (25×10^{-6}). For this system, l' is effectively about 3λ in brass (the waveguide) and 9λ in aluminum (the feed horn) at 23.8 GHz.

The measured vswr and calculated reflection coefficients for the isolator and the feedhorn/GOA are given below.

TABLE 4.7 VSWR and Reflection Coefficients of WVR antenna system components		
component	vswr	reflection coefficient Γ
dual junction isolator	1.1	.05
gaussian optical antenna	1.15	.07
corrugated feed horn (est.)	$< \sim 1.05$	$< \sim 0.025$

It is not practical to theoretically predict the temperature coefficient of the feed vswr ($\frac{d\Gamma_h}{dT}$), because a large component of this effect would come from manufacturing variations. The effect was therefore measured by thermally insulating the feed horn and heating the horn while measuring the gain of the WVR and measuring the physical temperature of the feed horn. Thermal insulation of the feed horn from the antenna waveguide was accomplished with a 1/2" section of ABS plastic WR34 waveguide, plated in copper and then gold. Gain was measured by alternately observing a LN2 and an ambient target. The temperature of the feed horn was cycled quickly to avoid heating the Rexolite lens and other GOA components. The feed horn was found not to vary in transmission or vswr with temperature, within the resolution of the experiment. One of the Moreno noise diode crosscouplers was found to be sensitive to the physical strain caused by heating the feed horn, and was reworked and replated.

4.6.2 Temperature coefficient of the system electronics - the analog board

No components on the digital board that would affect the gain with temperature variation were identified.

Several receiver voltages and currents are controlled by the analog board.

These are the RF deck physical temperature control, the Gunn oscillator supply voltages, the Gunn simmer voltages, the noise diode current, the noise diode simmer current, and measurement of the physical temperature of the black body. Only the noise diode output variations and black body temperature measurements can contribute to gain reference errors; because the receiver gain is measured at each observation, receiver gain drift is taken out of each observation. The error and temperature drift in black body temperature measurements are directly proportional to the error and drift in the reference resistance associated with the two blackbody temperature sensors. These resistances are high precision, 0.01% and 5 ppm/C (RN55C mil spec metal film resistors are typically 1% and 200 ppm/C).

A noise diode is used as a gain reference for the WVR receiver. The output of this reference is dependent upon its drive current. This current is compared to a precision voltage reference via a shunt resistor. We are searching for sources of about $\pm 500\text{ppm}/C$. The voltage reference has a maximum temperature coefficient of $\pm 2.5\text{ppm}/C$, and is therefore not part of the observed gain drift.

Two OPA27FZ precision instrumentation op amps are associated with the noise diode current control. These op amps have a maximum input offset voltage drift of $1.3\ \mu\text{volt}/C$ for a total maximum drift of less than $\pm 3\text{ppm}/C$. These op amp drifts are therefore ignored.

To determine the effect of temperature changes on the noise diode current regulator circuitry, and therefore upon the noise diode power output, the variation of noise diode output with current was measured, and the specification resistance coefficient of $\pm 200\text{ppm}/C$ for the 1% resistors was used to calculate the overall gain reference temperature coefficient. The noise diode video output for one receiver was found to be:

$$V_{nd23.8}(\text{volts}) = 1.805 - 0.0668i(\text{ma}) \quad (4.33)$$

$$V_{nd31.4}(\text{volts}) = 0.703 + 0.0910i(\text{ma}) \quad (4.34)$$

over the range of 8 to 11 ma. Or as fractional changes, which are directly related to changes in the gain reference:

$$d(\text{gain}_{23.8}) = \frac{dV_{nd23.8}}{V_{ave}} \simeq -0.6 \frac{di}{i_{ave}} \quad (4.35)$$

$$d(\text{gain}_{31.4}) = \frac{dV_{nd31.4}}{V_{ave}} \simeq +0.6 \frac{di}{i_{ave}} \quad (4.36)$$

There are 7 resistances in the noise diode current regulation circuitry, all of which have roughly the same directly proportional effect upon the current regulation. The rms coefficient due to resistor tolerances then becomes $\pm 200 \text{ppm} \times \sqrt{7} \sim 0.0005$, and the gain coefficient becomes:

$$\frac{d(\text{gain}_{23.8})}{dT} = \frac{\frac{dV_{nd23.8}}{V_{ave}}}{dT} = \frac{\frac{dV_{nd23.8}}{V_{ave}}}{\frac{di}{i_{ave}}} \frac{di}{dT} = \pm 0.6 \times 0.0005/C = \pm 0.0003/C \quad (4.37)$$

$$\frac{d(\text{gain}_{31.4})}{dT} = \frac{\frac{dV_{nd31.4}}{V_{ave}}}{dT} = \frac{\frac{dV_{nd31.4}}{V_{ave}}}{\frac{di}{i_{ave}}} \frac{di}{dT} = \pm 0.6 \times 0.0005/C = \pm 0.0003/C \quad (4.38)$$

These coefficients are of the magnitude of the observed $0.0005/C$ gain coefficient in the WVRs. These resistances have therefore been replaced with 0.01% and 10ppm/C resistors.

4.6.3 Conclusions regarding the temperature coefficient of gain

Antenna system: The above analysis shows that the temperature coefficient due to physical change in waveguide size and to the change in conductivity with temperature are insignificant effects relative to the observed temperature dependence of WVR receiver gain with temperature. The origin of the observed temperature coefficient remains uncertain, but can be measured for the WVR and is sufficiently stable and predictable. An appropriate correction can therefore be modeled.

Yet unexplored candidates for the coefficient are: strains that change with temperature in the waveguide system (especially the noise diode cross coupler)

(high probability), change in insertion loss of the Rexolite lens (low probability), hygroscopic uptake of the Rexolite lens (low probability), and change in feed horn sidelobe patterns with temperature (remote probability).

Electronics: Two elements of the electronics system require high thermal stability; the measurement of the black body temperature, and control of the noise diode current. High precision resistors are implemented where required. None of the ICs required higher temperature stability.

4.7 Observation reduction algorithms of the Radiometrics WVR-1100 water vapor radiometer

4.7.1 The radiometer measurements

The radiometer makes sky observations by making a series of radiometric measurements in the following manner, but not necessarily in the given sequence (the sequence and content of the sequence are user-selected).

1) A radiometric measurement of the blackbody target of known temperature is made with the noise diode off by turning the antenna mirror to the blackbody. This measurement includes the antenna and mirror system, but not the hydrocarbon microwave window.

2) A radiometric measurement is made with the noise diode off of the sky. This measurement includes the antenna, mirror, and hydrocarbon window.

3) A radiometric measurement is made of either the sky or the blackbody (or both) with the noise diode on. This third measurement, when subtracted from the measurement of the same target with the noise diode off, gives the temperature (in counts) added to the receiver by the noise diode.

Additionally, at the dictate of the operator, some of the observations can be repeated or omitted in each observing cycle. This measurement routine is user defined in the WVR.cfg file.

4.7.2 The radiometer equation

The radiometer equation for the Radiometrics WVR is:

$$T_{sky} = T_{bb} - \frac{(N_{bb} - N_{sky})}{G} \quad (4.39)$$

where all terms contain their inherent errors and uncertainties, and where G , the gain of the receiver, is:

$$G = \frac{N_{bb+nd} - N_{bb}}{T_{nd}} \quad (4.40)$$

and where

T_{sky} is the temperature of the field of view of the antenna (sky), as calculated from receiver observations. This observation includes the subKelvin contribution of the hydrocarbon window.

T_{bb} is the physically measured blackbody temperature

N_{bb} is the number of counts, or zero crossings, of the output of the V to F converter while the antenna field of view is directed to the blackbody.

N_{sky} is the number of counts of the output of the V to F converter while the antenna field of view is directed to the sky.

N_{bb+nd} is the number of counts while the antenna field of view is directed to the blackbody and the noise diode is on.

T_{nd} is the temperature added to the antenna waveguide by the noise diode. This added temperature is predetermined from tip curve calibrations.

The errors in these measurements were described in Table 4.3.

Determination of T_{nd} is described in the following section, entitled *Tipping (Tip) Curves as Calibration*.

4.7.3 Tipping (tip) curves as calibration

The radiometer gain is calibrated utilizing tipping curves. Sky observations are made at several different elevation angles, and therefore through several air masses. Assuming homogeneous sky conditions, assumptions about these

observations can be made that allow us to estimate both the zenith brightness temperature and the instrument gain without any a priori knowledge of either. The assumption that is made is that opacity is a linear function of air mass and that the intercept of this function must pass through the origin since at zero air mass there should be zero opacity.

The following method is adopted from methods due to Hurst [1987] that were subsequently incorporated into software methods by Röcken and James Johnson of UNAVCO. In order to begin the calibration, we must first make a guess at either the zenith brightness temperature or the gain of the instrument. From this first assumption, opacity is calculated for each air mass. A fit of opacity vs. air mass is then made and the intercept noted. If the intercept passes through the origin within a tolerance of 0.0001 nepers, then it is assumed that the initial guess was correct and no further calibration steps are necessary. If, however, the intercept does not pass through the origin, then the opacity at each air mass is moved such that the linear fit does pass through the origin. These new opacities are then taken to be actual opacities and brightness temperatures are recalculated at each air mass. The gain of the instrument is calculated at each air mass by comparison to the black body measurement then averaged to give a new estimate of the radiometer gain. The process is then repeated until the intercept is within tolerance of the origin or a maximum of 5 iterations have been made. A detailed outline of the algorithm follows:

(1) Observations (N_{sky}) are made at n elevation angles (el_i) and air mass (AM_i) is calculated:

$$AM_i = \frac{1}{\sin(el_i)} \quad (4.41)$$

(2) Gain of the instrument is estimated using the current value of the noise diode:

$$G = \frac{N_{bb+nd} - N_{bb}}{T_{nd}} \quad (4.42)$$

(3) Brightness temperatures are calculated at each elevation angle:

$$T_{sky_i} = T_{bb} - G^{-1}(N_{bb} - N_{sky_i}) - (T_{corr_{bw}} + T_{corr_{win}}) \quad (4.43)$$

The last two terms are corrections due to beam width and the radiometer window, respectively.

(4) Opacity is calculated:

$$\tau_i = \ln\left(\frac{T_{mr} - T_{cosmic}}{T_{mr} - T_{sky_i}}\right) \quad (4.44)$$

(5) A least squares fit is calculated for opacity vs. air mass:

$$[a, b, r] = LSFIT(AM, \tau) \quad (4.45)$$

Where $\tau_i = a \cdot AM_i + b$ and r is the regression coefficient.

(6) If the intercept is within tolerance of the origin, then we stop and use the current gain as the gain of the radiometer. If this is the second iteration, then we continue even if the intercept is valid. This is because when we convert corrected opacities back to brightness temperatures, we must put back the beam width and window corrections. The beam width corrections that are used to ‘uncorrect’ the brightness temperatures are the values obtained in step (3) and may not be valid if new brightness temperatures are extremely different from the old brightness temperatures. Therefore if we iterate at all, we make sure we do it at least twice so that we ‘uncorrect’ the new brightness temperatures with a reasonable beam width correction value.

(7) Adjust opacities to force intercept to go through the origin and recalculate brightness temperatures:

$$\tau_i = \tau_i - b \quad (4.46)$$

$$T_{sky_i} = T_{mr} - (T_{mr} - T_{cosmic})e^{-\tau_i} + (T_{corr_{bw}} + T_{corr_{win}}) \quad (4.47)$$

(8) A new gain is calculated by averaging gains obtained at each new brightness temperature:

$$G_{new_i} = \frac{N_{bb} - N_{sky_i}}{T_{bb} - T_{sky_i}} \quad (4.48)$$

$$G = \overline{G}_{new} \quad (4.49)$$

(9) We go back to step (3) to check to see how well our new gain will give an opacity fit that goes through the origin.

(10) Once we have a gain we are satisfied with, we check the regression coefficient for the last fit to opacity vs. air mass. If it is greater than the value read in from the WVR.cfg file, then the tip curve is considered to be good and a new noise diode value is calculated using the new gain. This new noise diode value is then used to update the exponential average of the noise diode:

$$T_{nd_{new}} = G^{-1}(N_{bb+nd} - N_{bb}) \quad (4.50)$$

$$T_{nd_{NewExpAve}} = 0.9T_{nd_{OldExpAve}} + 0.1T_{nd_{new}} \quad (4.51)$$

Note that errors in the mean radiating temperature T_{mr} do not effect the noise diode calibration. This is because, after the opacity values are iterated to intercept zero at zero air masses, the receiver offset at zero air masses (0K) and the receiver video while the antenna is at the blackbody are used to determine receiver gain. These values are independent of the selection of T_{mr} . This gain is then transferred to the noise diode.

Errors in T_{mr} do affect calculations of opacity from line-of-sight brightness observations, however. This error source was discussed in Chapter 3.2.

4.7.4 Line-of-sight measurements

Line-of-sight values are determined by making an observation of the sky (with window and beamwidth corrections, see below) and of the blackbody. The blackbody measurement determines the receiver offset, while the noise diode determines the receiver gain. The sky temperature is then calculated in the following manner:

$$T_{sky} = T_{bb} - G^{-1}(N_{bb} - N_{sky}) \quad (4.52)$$

where:

$$G = \frac{N_{bb+nd} - N_{bb}}{T_{nd}} \quad (4.53)$$

or

$$G = \frac{N_{sky+nd} - N_{sky}}{T_{nd}} \quad (4.54)$$

The reference target is the choice of the user, as defined in the WVR.cfg file.

4.7.5 Software corrections to the observations

1) Hydrocarbon window correction: The contribution of this window is known from manufacturer's specifications, and is entered into the WVR.cfg file. The increase in observed temperature is of the magnitude of 0.5K, and is proportional to the *difference* between ambient and sky temperature. This contribution is calculated as follows.

The insertion loss within a nonpermeable dielectric is:

$$insertion\ loss\left(\frac{dB}{cm}\right) = \frac{2\pi(8.686)}{\lambda_0} \sqrt{\frac{K_d}{2} \left[\sqrt{1 + \tan^2 \delta_d} - 1 \right]} \quad (4.55)$$

These losses contribute to temperature by reradiating to the same extent as the insertion loss. The hydrocarbon window used by Radiometrics in the WVR has the following electrical properties that create an insertion loss:

dielectric constant $\epsilon = 1.06$

loss tangent $\tan(\delta_d) = 0.0001$

thickness 0.125 inches = 0.32cm

The insertion loss calculates from (A) above to be:

$$insertion\ loss\left(\frac{dB}{cm}\right) = \frac{.0028}{\lambda_0(cm)} \quad (4.56)$$

or

$$insertion\ loss(dB)_{23.8} = .00071dB \quad (4.57)$$

$$insertion\ loss(dB)_{31.4} = .00094dB \quad (4.58)$$

for .32cm hydrocarbon foam material.

This represents an insertion contribution of:

$$23.8 \rightarrow 0.00164(K/K) \quad (4.59)$$

$$31.4 \rightarrow 0.00217(K/K) \quad (4.60)$$

where the (K/K) represents the temperature contribution per K of temperature *difference* between the target and ambient.

We need to consider the reflections from the front and back surfaces of the dielectric. The window is near $\lambda/4$, the criterion for destructive interference for reflection. For 23.8 GHz, this $\lambda/4$ criterion is sufficiently satisfied, but for 31.4 GHz there is a slight reflection. The reflection at each interface is:

$$\frac{reflected\ power}{incident\ power} = \left[\frac{\sqrt{\epsilon} - 1}{\sqrt{\epsilon} + 1} \right]^2 = .0002 \quad (4.61)$$

After applying the phase thickness of the window at 31.4GHz, this results in a coefficient of 0.0001K/K.

The insertion loss at 23.8 GHz, and the insertion loss and reflection at 31.4 GHz result in the following coefficients:

$$0.00164K/K\ at\ 23.8\ GHz \quad (4.62)$$

$$0.00227K/K\ at\ 31.4\ GHz \quad (4.63)$$

Again, these coefficients are applied against the *difference* between the target (sky) temperature and the window (ambient) temperature.

2) Antenna beamwidth corrections: Corrections to brightness are made in software to compensate for the finite beamwidth of the field of view. The theoretical antenna pattern is that of a circular aperture, with Bessel function field solutions. In practice, the E plane and H plane patterns differ from

theoretical because of less-than-ideal conductivity and construction of the feed horn and lens, with the E plane typically deviating from theoretical more than the H pattern.

The pattern of a feed horn can be described as a gaussian central lobe, with the sidelobes approximated as a Lorentzian function (see Lundquist and Potash, 1985). The Radiometrics antenna is a lensed feedhorn, yielding the performance of a feed horn much larger than is incorporated. The feed horn is corrugated to modify the field in the E-plane from uniform at the apex of the feed horn to cosine at the aperture. The lens focuses plane wave signal incident upon the antenna into the phase center of the feed horn. The usual drawback of such a lensed antenna is that the Rexolite lens has an insertion loss and therefore contributes to antenna temperature, but this is overcome in the Radiometrics radiometer by measuring the blackbody reference through the antenna system, thereby including the Rexolite in the measurement.

Although the sidelobes of the gaussian optical antenna are down from the central peak (about 30 dB for the first sidelobe), the sidelobes are at a larger radius, and therefore can incorporate significant area and are located well off the central axis. Segments of the sidelobes can therefore receive from elevation angles (and therefore, from paths through air masses) very different from the central axis. This effect is especially significant at low antenna angles. For example, an observation at 30 degrees elevation is in error by about 0.4% of the air mass value for a 5 degree FWHM antenna, and about 1.4% at 20 degrees [Elgered, et al., 1985]. These biases are mitigated somewhat, but not eliminated, in tipping curve calibration by the linear fitting of opacity to air mass.

The beam correcting routine presently implemented is adopted from the Kamikaze software of S. Robinson, JPL. In this routine, the sensitivity of the GOA is approximated by a gaussian curve, rotated about its center to generate a pattern symmetrical about the central (propagation) axis of the antenna. The sidelobes are ignored. Because the logarithm (utilized to calculate opacity) is a transcendental function, an iterative solution is required. The brightness cor-

rection is iterated until the change in brightness correction is less than $0.05K$.

The iterated correction to the brightness temperature is:

$$T_{corr} = \frac{0.36067(T_{MR} - T_b)(FWHP \text{ beamwidth})^2 \tau}{2/\cos^2\theta - \tau \tan^2\theta} \quad (4.64)$$

where:

T_{corr} is the correction to the brightness

θ is the zenith angle of the beam center

This correction is subtracted from the observed brightness temperature.

3) Receiver temperature correction: The microwave receiver is temperature controlled to within several Kelvins. The noise diode mount is controlled to within several hundredths of a Kelvin. Not temperature controlled, and therefore floating at ambient temperature, are:

(1) The hydrocarbon microwave window, as described above.

(2) The gaussian optical antenna, including the Rexolite lens and the absorber inside the barrel and on baffles within the antenna housing.

(3) The corrugated feed horn within the gaussian antenna.

(4) A short (about 3") 90 degree E-bend section of waveguide that couples the antenna system to the temperature controlled receiver. One end of this elbow is at ambient temperature, and the other is at the receiver temperature. This short section of gold-plated WR34 waveguide has an insertion loss of about $0.06dB$, and varies slightly with ambient temperature. This temperature dependence is analyzed in §4.7.1.

There is a slight dependence of gain of the radiometer receiver upon the ambient temperature. Because this coefficient can occur with either a plus or minus sign, it cannot be solely attributed to temperature dependent insertion losses of components (which would always be minus), but rather is presumably due to a change in vswr and matching of one or more of the above uncontrolled components. This coefficient is of undetermined origin, varies from instrument to instrument and between the two channels, and can be as great as $\pm 0.04\%$

change in gain per Kelvin. The coefficient is applied against the noise diode injection temperature, and therefore against gain, as the dependence manifests itself as a linear effect upon gain of the receiver.

There are temperature dependent offsets (as opposed to gain) that are due to losses in components that are not temperature stabilized. These components are contributors to measured temperature to the same extent that they are losses, with their radiative contribution proportional to their physical temperature. The contributions include ohmic losses in the waveguide and feed horn, dielectric losses in the Rexolite lens, and antenna sidelobes that terminate in absorber rather than intended target. Offset changes due to these contributions of antenna system losses are accounted for by referencing to the blackbody in the measurement cycle. The receiver system equivalent temperature T_{sys} , and therefore antenna thermal contributions, are included in the counts measured at this target.

This temperature coefficient of the gain is determined by performing many tipping curves through a range of ambient temperatures, and then taking a linear regression (least squares) fit of (*noise diode injection temperature*) as a function of (*blackbody temperature*). The *ND_Calib.log* file contains raw gain (*noise diode injection temperature*) data along with ambient temperature (*blackbody*) data, and is therefore a convenient source of data for this regression fit. This coefficient is expressed as K/K (Kelvins change in T_{nd} per Kelvin change in ambient temperature, T_{bb}), and is entered by the user into the *WVR.cfg* file.

A number of valid (passing) tips (more than, say, 10) must be performed after this coefficient is changed to allow the compensated and averaged T_{nd} values to converge to their correct value. Alternately, one can use the regressed values to determine the noise diode injection temperature at T_{nom} , $290K$, and insert this value into the *ND_Calib.log* file for the last entry.

4.7.6 Quality control algorithms

There are several checks that are made upon the operation of and values produced by the radiometer. If any of these checks are out bounds, an error message is written to the screen, and is be written to a file named *yjjjhhmm.err* (year-Julian day-hour-minute.err) when the WVR.exe Version 4.0 code is completed.

The performance checks, in the order that they are made, are listed below.

The following EPROM checks are performed upon power-up.

Ground and +10 volt precision voltage reference checks with voltage-to-frequency converter. These measurements must be in bounds, or the comment *V to F problems* is echoed.

The elevation of the mirror is brought to zero (nadir) upon initialization. The azimuth drive, if attached, is then indexed to zero. At present, failure of either of these rotations to find the index flag does not produce an error message. Such flagging is being considered. Instead, the stepping motors will step 30,000 steps (750 motor revolutions, mirror; 1500 motor revolutions, azimuth drive) and then halt.

The following checks are performed in the FORTRAN code.

System voltages are measured and compared to predefined limits. These voltages include power supply voltages, Gunn diode oscillator voltages, noise diode voltage, and physical temperatures of the blackbody, mixer, and Gunns.

The Gunn/mixer stability is checked by turning on each Gunn separately and observing consecutive 0.5 second video voltage readings while the antenna is at the blackbody. Readings are taken until successive readings are within 500 microvolts of each other. This test may take some time if the receiver is cold. It will take from 5 to 15 minutes for the microwave receiver to warm to its preset physical temperature, depending upon the receiver initial temperature. Each test is annunciated to the screen with an asterisk (*). This testing can be passed over by pressing ENTER at the keyboard.

The blackbody (and internal cabinet temperature) will float several degrees above ambient temperature because of power dissipated by the receiver and its heater. The blackbody has two physical temperature sensors. The values from these two sensors are averaged. Should either of these sensors fail and give a temperature reading less than 250K or greater than 350K, or if the temperatures differ by more than 1K, an error is announced to the screen and is written into the *yjjhhmm*.err* file.

Chapter 5 The WVR and Geodesy Experiments and Results

5.1 The UNAVCO-Platteville Baseline

After the two radiometers were characterized in local experiments, the radiometers and two TrimbleTM 2000SST 8 channel dual frequency GPS receivers were located at each end of a 50 *km* baseline between the UNAVCO facility at Boulder and the VLBI site at Platteville Colorado NE of Boulder. This experiment was to determine the increase in vertical accuracy (if any) that could be realized by removing water vapor anisotropies with pointed WVR observations. GPS phase data were taken at 30 second intervals for all satellites above 15 degree elevation angle. The WVR elevation mask was set to 10 degrees so that interpolation of WVR data could be performed down to the 15 degree GPS mask. Data at the UNAVCO end were manually downloaded every 4 days. GPS data from Platteville were automatically downloaded each night. The radiometer at Platteville was operated via a MUXed dedicated NOAA telephone line that terminated at NOAA Wave Propagation Laboratory (WPL) in Boulder. Data were retrieved via Laplink cable from the PC to a laptop computer at NOAA WPL every week. The telephone links were very reliable, with the exception of a cable cut by a backhoe and a lightning hit. The Platteville site was visited several times during the 4 months of operation (August through December), but was otherwise unattended.

Satellite ephemerides were obtained from the GPS receivers and read by the WVR controlling program. This program determined which GPS satellites were above a preselected elevation angle (15 degrees), ranked them by azimuth, and then measured the water vapor along the propagation path to each of these satellites in sequence. In addition to the elevation cutoff, an elevation mask was established at each site to eliminate obstructions such as radio towers and trees.

A solar software mask was also created that removed data that had included the sun in the main antenna lobe of the WVR.

Each pointed WVR observation took about 1 minute. This ranking and observing routine was then repeated for 12 hours, at which time 4 orthogonal tip curves were performed to verify calibration of the WVRs. At the end of each 24 hour period, the WVR program was terminated to close the data files, and the computers rebooted in the event that the RS232 port(s) had locked up. RS232 ports under DOS are prone to problems.

In September it was found that the WVR tripod at Platteville had slipped, bringing the WVR about 2 degrees out of level. It was determined from the tip curve data when the slump occurred, and line of sight data were corrected accordingly. Slight WVR elevation pointing errors were corrected by a simple *cosecant* function correction. On December 19 it was found that the radiometer mount at UNAVCO had loosened and the radiometer had rotated. From low-angle brightnesses it was determined when the radiometer had rotated, and data that were erroneous in azimuth were mapped to and used for zenith calculations only. Because these were not true zenith observations, they were averaged for 20 minutes. The laptop computer clocks had been set 12 hours off on several occasions; we were able to find and correct these occurrences, but the pointing data were erroneous and could only be used for zenith calculations.

5.2 Results

A total of about 600 hours of usable WVR data were collected. Of this data set, there were 19 days of data with more than 20 hours and where all observation systems were operational. For convenience and rapid reference, WVR and surface meteorological data were catalogued as in Figure 5.1 below.

Bernese (Astronomical Institute at the Universität Bern, Switzerland) version 3.3 [Beutler et al., 1987] software was modified by Chris Röcken of UNAVCO to include Kalman filter and by Teresa Van Hove of UNAVCO to include least

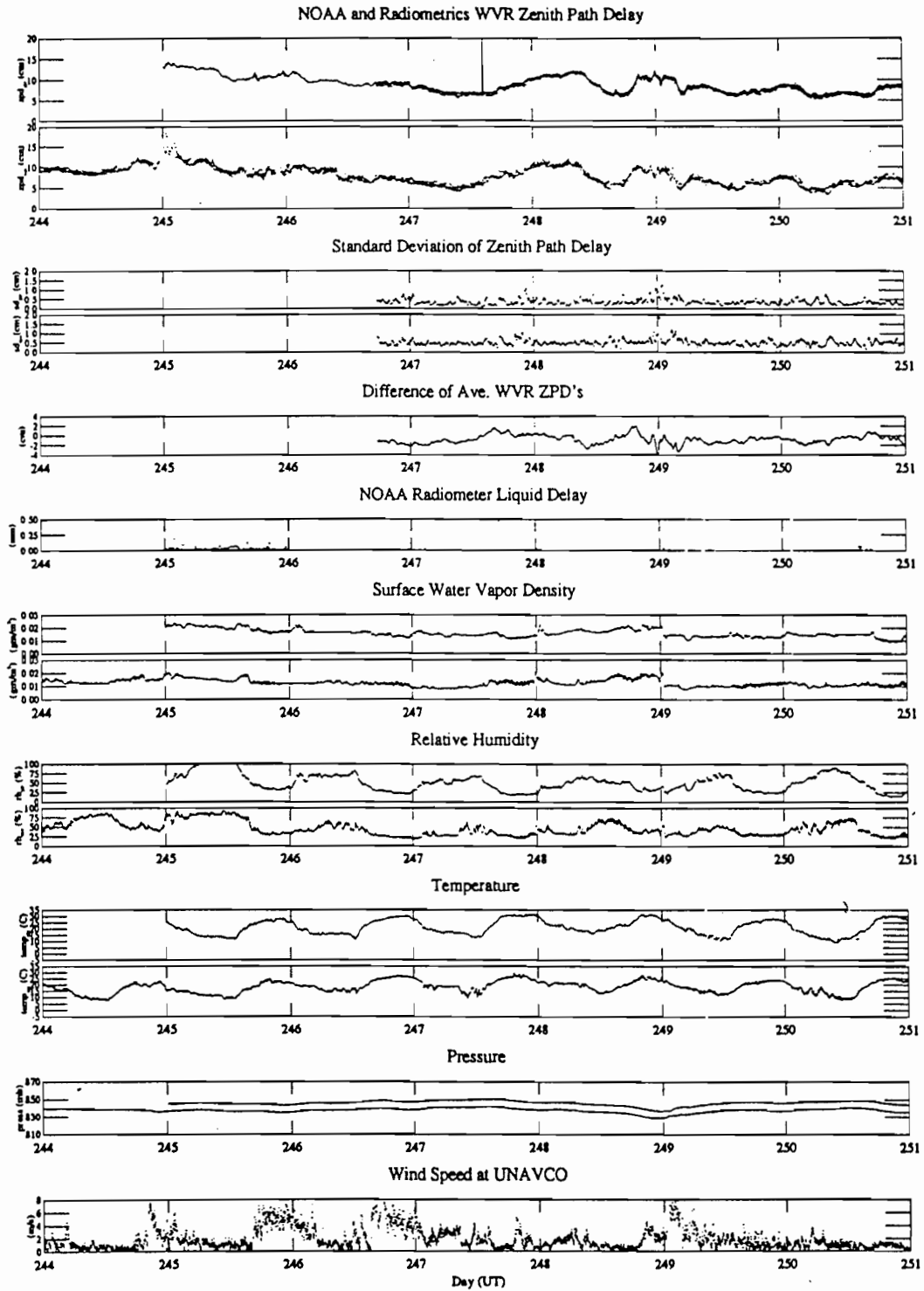


FIGURE 5.1 Typical field data

squares atmospheric delay estimates, and to ingest the WVR and surface meteorological data and then solve the WVR-corrected GPS data.

We used the Saastamoinen model [Saastamoinen, 1972] which relates surface pressure, temperature, relative humidity, latitude and altitude of the site, to the zenith propagation delay. This model is:

$$\Delta L^z = \frac{0.002277 \left[P_s + \left[\frac{1255}{T_s} \right] e_s \right]}{1 - 0.0026(1 - \sin^2 \phi) - 0.00032H} \quad (5.1)$$

or, as implemented in the Bernese software,

$$\Delta L^z = \frac{0.002277}{\cos \theta} \left[P_s + \left[\frac{1255}{T_s} + 0.5 \right] e_s - b \times \tan^2 \theta \right] \\ + \textit{small tabular (lookup) correction} \quad (5.2)$$

where P_s , T_s , and e_s are the surface values of pressure, temperature, and vapor pressure (millibars, Kelvins), and ϕ and H are latitude and ellipsoidal altitude of the observing site. This zenith delay must be combined with a mapping function to determine off-zenith delays. The Cfa-2.2 model of Davis [1985] is considered a good representation. The Bernese software offers the choice of many mapping models, including Saastamoinen, Hopfield (modified), and Marini Murray. Because the Bernese and other GPS processing software solves in a least squares sense for corrections to the zenith tropospheric delay, solutions are somewhat insensitive to the starting model. The Bernese software used herein incorporates the Saastamoinen model.

Because of the poor correlation of surface relative humidity and surface temperature in the boundary layer with values aloft, in all cases below, the surface temperature was taken as +18C and the surface RH as 50%. The pressure was scaled to the antenna height relative to sea level at standard pressure (1013 mb) and a lapse rate of 7km.

The results of the vertical repeatability of the UNAVCO to Platteville baseline are described below and are summarized in Table 5.1 and in the bargraph below. The three methods utilizing pointed WVR observations (PWVR) were superior to all other methods. Two different sets of orbits were utilized, from the PGGA (Permanent Geodetic GPS Array) and from CODE (Centre for Orbit

Determination, Europe). The PGGA orbits were available for 19 of the 26 data days; the CODE orbits were available for all days. The CODE orbits resulted in better repeatability, presumably because they are derived from longer orbital arcs than the PGGA orbits. The results in rank of increasing repeatability (precision) with 26 days of CODE orbits are:

(a) Saastamoinen model with no least squares estimation of tropospheric delay allowed.

(b) WVR observations along the propagation path to each of the GPS satellites mapped to the zenith with a simple *cosecant* function and averaged over 10 WVR observations (about 10 minutes of observations), and no estimation of tropospheric delay allowed in the GPS solution. Surface pressure was used for the “dry” tropospheric delay.

(c) Saastamoinen model with least squares estimation of tropospheric delay allowed on a 24 hour basis.

(d) Saastamoinen model with least squares estimation of tropospheric delay allowed on an hourly basis.

(e) Saastamoinen model with Kalman filtering following the methods of Tom Herring of MIT, and holding the state vector (3 spatial coordinates, the satellite cycle ambiguities, and the allowed time rate of change of the atmospheric delay) fixed for the first 11 epochs. This stabilizes the Kalman filter but costs some repeatability. Otherwise, the position solution oscillates for several epochs until the (underdamped) state vector stabilizes. The tropospheric delay was constrained to change no faster than $4 \times 10^{-8} \text{ cm}^2/\text{sec}$. The same repeatability was realized by only allowing $1 \times 10^{-8} \text{ cm}^2/\text{sec}$ tropospheric change, and by constraining the Kalman state vector for the first 11 epochs to stabilize the solution.

(f) Saastamoinen model and Kalman filtering as above, but without holding the state vector fixed at the beginning of the data set.

(g) WVR observations along the propagation path to each of the GPS satellites, with daily least squares estimates of a spherically symmetric troposphere

allowed in the GPS solution.

TABLE 5.1 Vertical repeatabilities (<i>mm</i>) under different measurement and analysis methods and with CODE and PGGGA orbits		
Method	CODE 26 days	PGGA 19 days
a) Saastamoinen, no tropospheric offset	11.8	12.85
b) zenith WVR	5.4	5.6
c) Saastamoinen w/daily tropospheric estimate	4.9	7.5
d) Saastamoinen w/hourly tropospheric estimate	4.6	6.8
e) constrained Kalman filter (11 epochs)	4.5	7.4
f) unconstrained Kalman filter	4.4	6.6
g) pointed WVR w/one daily tropospheric estimate	3.8	5.1
h) Pointed WVR w/no tropospheric estimate	2.6	2.7
i) Pointed WVR w/hourly tropospheric estimate	2.3	3.3

(h) WVR observations along the propagation path to each of the GPS satellites, and no estimation of tropospheric delay allowed in the GPS solution.

(i) WVR observations along the propagation path to each of the GPS satellites, with hourly least squares estimates of a spherically symmetric troposphere allowed in the GPS solution. Allowing one more degree of freedom, the estima-

tion of tropospheric offset, improved the repeatability about 15% and diminished the vertical offset bias of the PWVR solutions from the Kalman and other solutions. Presumably this estimation of the residual troposphere served to partially remove this offset.

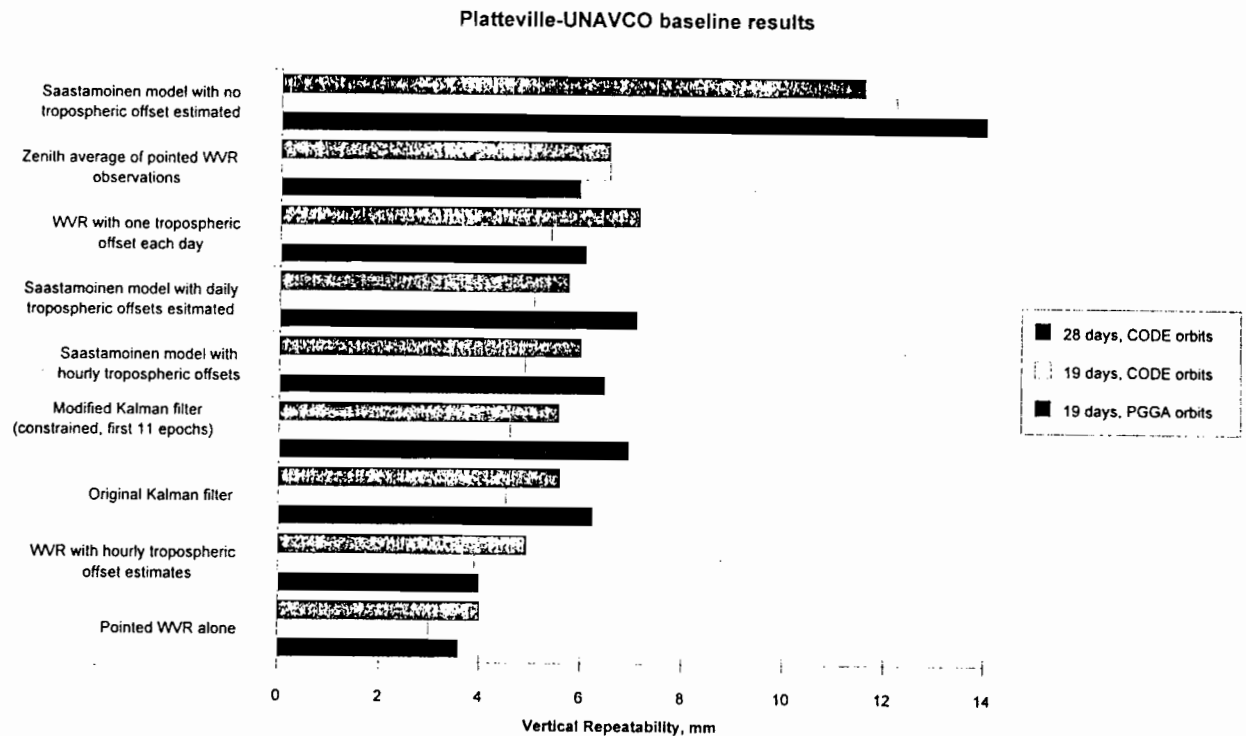


FIGURE 5.2 Comparison of the several data reduction methods that were employed. Repeatability of hourly solutions was about 40% better with PWVR solutions than the next best method.

The pointed WVR solutions (h) showed nominally a 9 mm bias from the Kalman and least squares solution methods (Figure 5.3). When a least squares estimate of residual tropospheric delay was allowed in the position solution, this bias disappeared (although the repeatability degraded). We therefore suspect a barometric pressure measurement offset. The surface pressure measurements

were required for these pointed solutions but not for any of the other solutions performed. A pressure bias at either the NOAA surface meteorology station at Platteville or the NCAR PAM II station proximate to the UNAVCO site, or alternatively, an error in measurements of the elevation differences between the sensors and the GPS antennas, or a combination of these errors would account for the observed bias. The pressure transducers were not accurate to submillibar levels, and further, one had not been calibrated in years. This bias in vertical dimension would reflect about a 1 *mb* error in the pressure sensors, or about a 9 meter error in the elevation differences.

The *zenith* WVR vertical repeatability results (5.4 *mm* precision) are somewhat consistent with the repeatabilities found by previous investigators. That the pointed WVR observations improved repeatabilities (2.6 *mm* precision) by a factor of two indicates that azimuthal and other variations in wet path delay can significantly degrade GPS positioning.

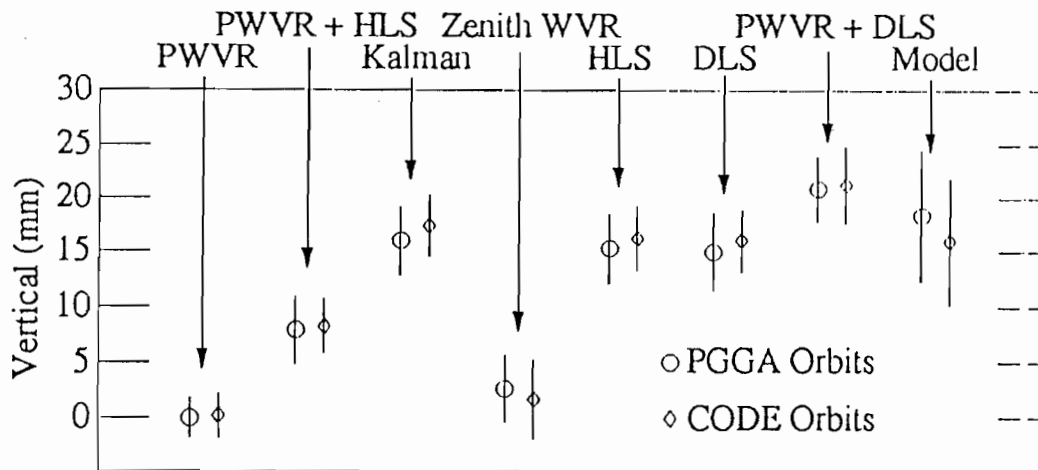


FIGURE 5.3 Difference in height of UNAVCO and Platteville, as determined by the various data reduction methods. Kalman filter and least squares methods were offset by more than 1 *cm* from the pointed WVR solutions. The unexplained offset may be due to surface pressure measurement offset, important to the PWVR solution.

Water vapor gradient solutions of VLBI data have been attempted with only occasional success [Tom Herring, personal communication]. The inference is that anisotropies in water vapor are not generally simple gradients, but often somewhat random inhomogeneities.

Inhomogeneities of a more random characteristic (of smaller spatial scale) have been observed in this thesis experiment. Chris Alber of UNAVCO is studying the spatial structure of the sky in water vapor in his PhD thesis effort, and finds differences as great as 5 *cm* in zenith-mapped vapor delays across some skies. The average zenith delays were about 10 *cm*; rms variations for the period of this experiment were on the order of 1.5 *cm*. Gradients were not often in evidence in these Colorado skies, indicating that estimations of gradients via the GPS solutions for inland sites may not show much improvement over tropospheric estimations without gradients.

5.2.1 Experimental errors

1) **Retrieval errors** are about 2 *mm* of water vapor under clear skies and near 4 *mm* for cloudy conditions (see §3.6). However, because of the similarity in atmospheres at the ends of this short baseline, we found that retrieval and mean radiating temperature errors tend to cancel. We found no change in repeatability for significant changes in retrieval coefficients and for changes in T_{mr} .

2) **WVR errors** have been discussed in §4.2 through §4.5, and are estimated at about 2 *mm* of zenith path delay (0.3 *mm* of water vapor). The two radiometers used in this experiment showed an rms difference of about 3 *mm* (2 *mm* attributable to each WVR).

3) **GPS orbit errors** for single differences contribute to baseline errors by the (*vector difference of the unit vectors from each of the two receivers to the satellite*), dotted into the (*orbit error*). Thus, for short baselines, the effect of orbit errors upon the baseline vector is minimal. That the quality of the orbits is important is shown above by the difference between CODE orbit and PGGA orbit solutions for position. We estimate the orbit errors at about 0.5 *mm* for

this baseline.

4) **GPS receiver temperature coefficient** effects were discovered in this experiment (see Chapter 6). These effects are estimated to contribute to the error budget at about 1.5 *mm* or less.

5) **Nonzero mean antenna multipath effects** tend to modulate the antenna position by several centimeters in periods of many minutes. Provided that the observation times are long enough and that the multipath environment is symmetric or perfectly random, these errors tend to average to zero mean. From the data we estimate the multipath error to be less than 1 *mm*. Solutions for 26 days with 12 hour of data were degraded from the 19 days with 20 hours of data by 30%; this degradation may be in part to nonzero mean multipath.

6) **Total rms error** of the above sources calculates to 3.1 *mm*. We are obtaining a slightly better experimental result than this (2.9 *mm*).

7) **Bias due to the barometers** at each end of the baseline. The barometers at each end of the baseline, necessary to GPS solutions using WVRs, were only accurate to about 1 millibar, and the calibration on one end was suspect. The resolution (precision) of the barometers was good, but an offset is suspected to be responsible for the vertical bias in the WVR + GPS solutions from the software GPS solutions. A 1 millibar error in each of these barometers would induce the observed bias.

5.2.2 Sensitivity to length of data set for daily solutions

An increase in repeatability for 24 hour data sets was found. Smaller data sets occurred at inconsistent periods during the day, and therefore were random cycles during the diurnal cycle. We observe a slight diurnal dependence of position solutions. There are several candidate causes; from revisiting the field data it is difficult to separate some of them.

Through laboratory experiments at UNAVCO it was found that the Trimble SSE receivers have a slight temperature dependence.

The diurnal variation of T_{mr} and its variation with weather regimes may be

a small effect, although it was found that short baselines are insensitive to T_{mr} .

Another temperature quantity (that can also be calculated from RAOBs) is T_m , the *mean temperature* (not *mean radiating temperature* of the atmosphere. This quantity is important to the refractivity of the atmosphere. Recall from §2.2.3 and §3.6 that refractivity is inversely proportional to the gas temperature (not water vapor temperature). Because water vapor distribution is different from the dry atmosphere distribution, this temperature differs from T_{mr} .

The antenna multipath may have some unidentified diurnal dependence, such as change in the surface moisture of the Bentonitic clay soil at Platteville. This soil becomes quite ionic with moisture. Surface moisture diminishes under the heating of the Sun, and increases at night because of capillarity and dew.

Slight temperature dependence of the barometer could also modulate the GPS solution. We propose highly accurate barometers (0.3 *mb*) mounted in temperature controlled environs for future precise experiments.

A subsequent field experiment is proposed in Chapter 6 to apply remedies to this and other effects that were revealed in this field experiment.

5.2.3 Short baseline insensitivity to errors in T_{mr} and in retrieval coefficients

Although §3.3 demonstrated the importance of the choice of T_{mr} , this choice was not critical in this experiment. Atmospheric profiles, and therefore the mean radiating temperature, of the short (50 km) baseline in this experiment were highly correlated. The induced errors are therefore common to both ends of the baseline and tend to cancel. This insensitivity to T_{mr} was revealed by solving the entire data set for vertical accuracy using (a) fixed values for T_{mr} , and (b) calculating T_{mr} at 0 and 12 UT from concurrent Denver RAOBs. The results were the same, within the process noise. T_{mr} was also correlated to surface temperature for 1992 Denver RAOBs, with rms deviations of about 3K. Using continuous surface temperature to estimate T_{mr} in the retrievals also showed

little improvement over using a fixed T_{mr} . The surface temperatures at the two ends of the baseline seldom differed by 10 C; presumably the mean radiating temperatures differed by less.

To test the sensitivity of the experiment to radiometer retrieval coefficients and line shape models, coefficients were generated with the old 1985 Liebe and Rosenkranz line shape models. The retrievals were then recalculated using the more current 22.235 GHz water vapor line shape models of Liebe [1987] as modified by Keihm [1991], and the updated oxygen line shape model due to Rosenkranz [1975]. These line shape models include a roughly 8% increase in the strength of the water vapor line, and a 15% increase in the underlying tail of the assemblage of oxygen lines at 60 GHz.

These coefficients were:

TABLE 5.2 Comparison of Denver Retrieval Coefficients with old and new line shape models (see equations 3.15ff)		
Coefficient	1985 Liebe	1991 Liebe/Keihm
water vapor:		
offset	0.019	-0.003
$\tau_{23.8}$	21.1	19.5
$\tau_{31.4}$	-12.2	-10.9
liquid water:		
offset	-0.009	0.048
$\tau_{23.8}$	-0.170	-0.023
$\tau_{31.4}$	0.621	1.260
phase path delay:		
offset		8.6
$\tau_{23.8}$		123.4
$\tau_{31.4}$		-59.4

5.2.4 Inference of water vapor from GPS solutions

The resultant difference in inferred water vapor was roughly 6%. The resultant change in elevation difference was about 1 mm . Again, because of the similarity of atmospheres at both ends of this short baseline, the difference in

vertical accuracy statistics was minimal for these two cases. These insensitivities, in contrast to the improvement of GPS vertical accuracy using *pointed* WVR corrections, highlight the importance of the effect of anisotropy of water vapor to the accuracy of GPS solutions.

Because it is a component of atmospheric refractivity, atmospheric water vapor was once a source of noise to GPS position measurements. GPS geodesy now has evolved to a point where such GPS measurements can estimate *differences* in atmospheric water vapor values between sites as well as position; what was once measurement noise can now be viewed as signal. Although this measurement is an *integrated* value of water vapor and not a profile, it is of great value in weather modeling [see, for instance, Bevis, 1992; Kuo, et al., 1993]. It is also of value in global climate research [Yuan, et al., 1992].

With known orbits and *a priori* knowledge of position, the GPS position solution can be allowed to estimate the tropospheric delay in a least squares sense. This delay is due to the *dry* and the *wet* components of the troposphere. As shown in §2.2.1, the dry delay can be removed with a sensitive barometric measurement (several tenths of a millibar). The difference is then the delay due to atmospheric water vapor. Estimations in this experiment matched the difference in the WVR measurements to within about 1 *mm* rms. Presently, the available GPS software models the wet delay as a spherically symmetric distribution; gradients and anisotropies are therefore ignored.

The GPS solutions were found to be quite capable of measuring the *difference* of water vapor burdens between GPS sites, but are not accurate at determining absolute offset. Very short baselines can determine the offset only to within about 5 *cm* (which can be > the total vapor value). Longer baselines (500 *km*), wherein the GPS antennas see the satellites at different positions in the sky, improve the ability to determine this offset to better than 2 *mm* of error.

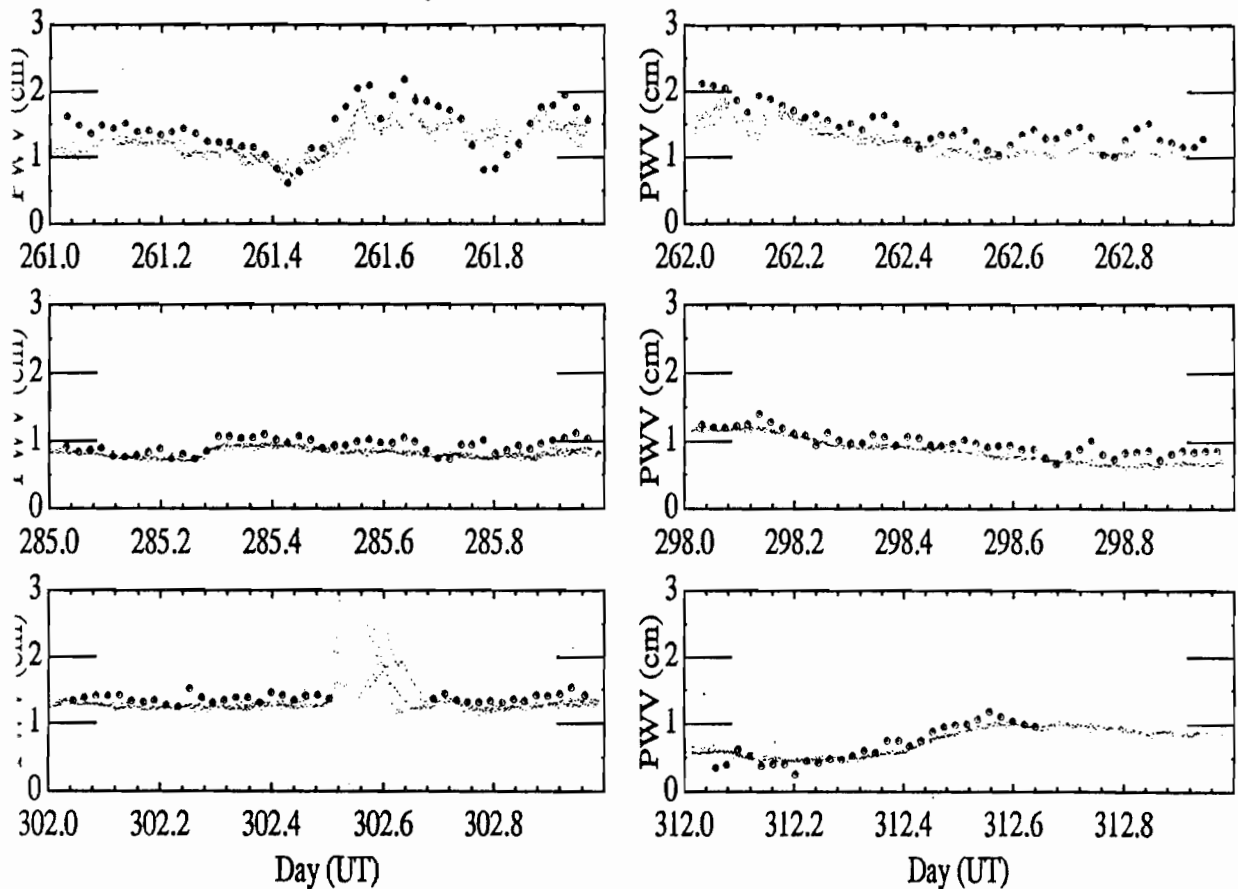


FIGURE 5.4 Comparison of zenith water vapor burdens as estimated by GPS solutions and as measured by WVRs. The open circles are 30 minute tropospheric least squares estimations in the GPS solution, and the small dots are pointed WVR observations that have been mapped to the zenith. The scatter in the WVR data is due to the anisotropy of atmospheric water vapor. On Day 261 the sky became quite anisotropic, and the GPS inferred water vapor deviates from the WVR. On Day 302.6 rainfall on the WVR window gave erroneous results which were not used. (From Röcken et al., 1990.)

Chapter 6 Epilogue - An Improved Follow-On Experiment

Although the Platteville-to-Boulder baseline experiment demonstrated improved results over all other GPS techniques, several unaddressed sources of error were realized during the experiment. By having identified these sources, we are able to devise remedies whereby we hope to further improve the vertical repeatability and accuracy of vertical geodesy. These are listed below.

Better barometric measurements: The pointed WVR data demonstrated an offset of about 9 *mm* from the Kalman and other data (Figure 5.3). The origin of this offset is unknown, but I suspect that one or the other of the barometric pressure transducers had a calibration offset. This vertical offset could be accounted for by a 1 *mb* error in the barometers. We will use our own Paro Scientific pressure transducers and automatically log pressure and surface data with the WVR/geodesy data set.

Temperature control: We also found a very slight diurnal variation in vertical difference. One of the SST receivers was inside the UNAVCO facility, while the other was in an unheated trailer at Platteville. To confirm and measure the temperature dependence, a receiver was placed in a container that could be heat cycled while a second receiver was held at a constant temperature. Both receivers were attached to a single GPS antenna. The resultant error is estimated to contribute 1.5 *mm* or less to vertical precision and position bias.

We will use new Trimble SSE receivers in the proposed experiment, and will stabilize their temperature environment. The SSEs are also more successful at fixing biases (carrier cycles or wavelengths) than the SSTs. We find that about 90% of the biases that could not be fixed by the SST receivers in a given observation scenario can be resolved by the SSEs.

Gipsy software: We used Bernese version 3.3 in this experiment. We intend to use JPL's Gipsy software as well as Bernese version 3.4 in the proposed

experiment. Gypsy allows “single satellite” solutions that will yield phase path length to any selected satellite.

24 hour solutions: In order to better remove multipath signal, and to defeat diurnal effects discussed in §5.2.2, the proposed system is to be robust so that longer data sets will be created. This will be accomplished with uninterrupted power supplies and local logging of data in the event of communication link loss. A more permanent WVR mount is also to be constructed; field tripods are not sufficient.

T_{mr} : Although the water vapor retrievals are somewhat insensitive to choice of T_{mr} on short baselines because the atmosphere is highly correlated, such is not true on longer baselines. We therefore intend to develop a mechanism to predict T_{mr} from surface temperature (about 4K rms error) and/or numeric weather models (about 2.5K rms errors).

Multipath: We will locate antennas to minimize multipath noise. Multipath noise is one of the significant remaining errors in GPS geodesy.

Preprocessing of RINEX files: We will develop software to correct RINEX (receiver independent exchange) format files for the pointed tropospheric delays, such that the product files will have the troposphere and its anisotropies removed.

Fieldworthy system: We intend to develop a GPS-WVR system that is fieldworthy, based on one controlling and data logging computer, including automatic logging of surface meteorology. Computer clock time is to be obtained from the GPS receiver to eliminate computer clock errors. The system will have a modem port for remote retrieval of data and conveyance of instructions if desired.

References

- Becker, G.E., and S.H. Autler, *Water vapor absorption of electromagnetic radiation in the centimeter wave-length range*, **Phys. Rev.** **70**, No. 5, pp 300-307, 1946.
- Beutler, Gerhardt, I. Bauersima, W. Gurtner, M. Rothacher, Tl Schildknecht, G. Mader, D. Abell, *Evaluation of the 1984 Alaska GPS Campaign with the Bernese GPS Software*, **J. Geophys. Res.**, **92**, 1295-1304, 1987.
- Bevis, M., S. Businger, T. A. Herring, C. Röcken, R. A. Anthes, and R. H. Ware, *GPS Meteorology: Remote Sensing of Atmospheric Water Vapor using the Global Positioning System*, **Journal of Geophysical Research**, **97**, 15,787-15,801, 1992.
- Bevis, M., S. Businger, T. A. Herring, C. Röcken, R. A. Anthes, and R. H. Ware, *GPS Meteorology: Mapping Zenith Wet Delays onto Precipitable Water*, **Journal of Geophysical Research**, submitted 1993.
- Bögel, Werner, *Neue Näherungsgleichungen für den Sättigungsdruck des Wasserdampfes und für die in der Meteorologie gebräuchlichen Luftfeuchte-Parameter (New Approximate Equations for the Saturation Pressure of Water Vapor and for the Commonly Used Meteorological Humidity Parameters)*, **Deutsche Forschungs- und Versuchsanstalt für Physik der Atmosphäre**, Oberfaffenhofen, 1977.
- Born, M., and E. Wolf, *Electromagnetic Theory of Propagation Interference and Diffraction of Light*, Chapter 2, Sixth Edition, Pergamon Press, 1980.
- Brunner, F., and Min Gu, *An improved model for the dual frequency ionospheric correction of GPS observations*, **manuscripta geodaetica No. 16** pp 205-214, 1991.
- Budden, K.G., *The Propagation of Radio Waves, The Theory of Low Power Radio Waves in the Ionosphere and Magnetosphere*, Cambridge University Press, 1985.
- Chandrasekhar, S. *Radiative Transfer*, Dover Publications, 1960
- Chao, C.C., *A model for tropospheric calibration from daily surface and radiosonde balloon measurements*, **Technical Memo 391-350**, JPL, Pasadena CA, 1972.
- Chiswell, S.R., S. Businger, M. Bevis, F. Solheim, C. Röcken, *The Impact of Mean Radiating Temperature in Retrieval of Integrated Water Vapor from Water Vapor Radiometer Measurements*, **submitted JOAT**, 1993.

Cohen, C. E., and B. W. Parkinson, *Mitigating Multipath Error in GPS Based Attitude Determination*, 14th Annual AAS Guidance and Control Conference, **AAS 91-024**, 53-68, September, 1991.

Cohen, C. E., and B. W. Parkinson, *Integer Ambiguity Resolution of the GPS Carrier for Spacecraft Attitude Determination*, 15th Annual AAS Guidance and Control Conference, **AAS 92-015**, 11 pages, 1992.

Davies, K. *Ionospheric Radio Propagation*, **NBS Monograph 80**, April 1, 1965.

Davis, J.L., T.A. Herring, I.I. Shapiro, A.E.E. Rogers, and G. Elgered, *Geodesy by radio interferometry: Effects of atmospheric modeling errors on estimates of baseline length*, **Radio Science 20**, No. 6, pp 1593-1607, Nov.-Dec. 1985.

Davis, J.L., W. Prescott, J. Svarc, K. Wendt, *Assessment of GPS Measurements for Studies of Crustal Deformation*, **J. Geophys. Res.**, **94**, 13635-13650, 1989.

Debye, P., **Polar Molecules**, The Chemical Catalog Company, Dover Publications, 1929.

Dixon, T., and S. Kornreich Wolf, *Some Tests of Wet Tropospheric Calibration for the CASA Uno Global Positioning System Experiment*, **Geophysical Research Letters**, **17**, 203-206, 1990.

Elgered, G., B. Rönnäng, E. Winberg, and J. Askne, *Satellite-Earth Range Measurements 1. Correction of the Excess Path Length due to Atmospheric Water Vapour by Ground Based Microwave Radiometry*, **Research Laboratory of Electronics and Onsala Space Observatory Research Report 147**, 1985.

Elgered, G., *Characterizing of Atmospheric Water Vapour Fluctuations Using Microwave Radiometry*, **Research Laboratory of Electronics and Onsala Space Observatory Research Report No. 165**, 1990.

Elgered, G., *Tropospheric Radio-Path Delay from Ground-Based Microwave Radiometry*, in **Atmospheric Remote Sensing by Microwave Radiometry**, Wiley, ISBN 0-471-62891-3, 1993.

Flock, W.L., S.D. Slobin, and E.K. Smith, *Propagation effects on radio range and noise in earth-space telecommunications*, **Radio Science 17**, No. 6, pp 1411-1424, 1982.

Flock, W.L., *Propagation Effects on Satellite Systems at Frequencies below 10 GHz*, **NASA Publication 1082(02)**, 1987.

Gary, B.L., S.J. Keihm, and M.A. Janssen, *Optimum Strategies and Performance for the Remote Sensing of Path-Delay using Ground-Based Microwave Radiometers*, **IEEE Trans. Geosci. and Rem. Sens.**, **GE-23**, No. 4, July 1985.

Gu, M. and F.K. Brunner, *Theory of the Two Frequency Dispersive Range*

- Correction manuscripta geodetica* 15, pp 357-361, 1990.
- Herring, T.A., J.L. Davis, and I.I. Shapiro, *Geodesy by radio interferometry: The application of Kalman filtering to the analysis of very long baseline interferometry data*, **J. Geophys. Res.** 95, 12,561-12,581, 1990
- Hoehne, W.E., *Precision of National Weather Service upper air measurements*, NOAA Technical Memo NWS T & ED-16, 1980.
- Hufford, G., *A Model for the Complex Permittivity of Ice at Frequencies below 1 THz*, **Int. Jour. IR and MM waves** 12, No. 7, 1991.
- Hufford, G., *A Model for the Complex Permittivity of Ice at Frequencies below 1 THz*, **Int. Jour. IR and MM waves** 12, No. 7, 1991.
- Hurst, K.J., *The measurement of vertical crustal deformation*, PhD thesis, Columbia University, 1987
- Ippolito, L.J., *Propagation Effects Handbook for Satellite Systems Design*, **NASA Reference Publication 1082(04)**, 1989.
- Jackson, J.D., **Classical Electrodynamics**, 2nd Edition, John Wiley & Sons, 1975.
- Johansson, J.M., G. Elgered, and J.L. Davis, *Optimization of Wet Path Delay Algorithms using Microwave Radiometer Data*, **Research Report No. 152**, Dept. of Radio and Space Science with Onsala Observatory, Chalmers University of Technology, Gothenburg, Sweden, 198 .
- Kiehl, J.T., *Atmospheric Circulation models*, **Climate System Modeling**, Kevin E. Trenberth, Editor, Cambridge Press, 1992.
- Keihm, S.J., *Water Vapor Radiometer Intercomparison Experiment: Platteville, Colorado, March 1-14, 1991*, **JPL Task Plan 80-3289**, July 1991.
- Kuo, Ying-Hwa, Yong-Run Guo and E. R. Westwater, *Assimilation of precipitable Water Measurements inot a Mesoscale numerical Model*, **Monthly Weather Review** 121, No. 4, April 1993.
- Laws, J.O., and D.A. Parsons, *The relation of raindrops-size to intensity*, **Trans. Amer. Geophys. Union**, 24, Part II, 1943.
- Liebe, H.J., *An Atmospheric Millimeter Wave Propagation Model*, **NITA Report 83-137**, Feb 1983.
- Liebe, H.J., *An Updated Model for Millimeter Wave Propagation in Moist Air*, **Radio Science** 20, 1069-1089, 1985.
- Liebe H.J., K. C. Allen, G. R. Hand, R. H. Espeland, E. J. Violette, *Millimeter-Wave Propagation in Moist Air*, **NTIA Report 85- 171**, 1985.

- Liebe, H.J., *MPM-An Atmospheric Millimeter-wave Propagation Model*, **Int. Jour. of IR and MM Waves**, 10, No. 6, 1989a.
- Liebe, H.J., T. Manabe, and G.A. Hufford, *Milimeter-Wave Attenuation and Delay Rated Due to Fog/Cloud Conditions*, **IEEE Trans. on Ant. and Prop.**, 37, No. 12, December 1989b.
- Liebe, H.J., G.A. Hufford, and T. Manabe, *A Model for the Complex Permittivity of Water at Frequencies below 1 THz*, **Int. Jour. of IR and MM Waves**, 12, No. 7, 1991.
- Liebe, H.J., P.W. Rosenkranz, and G.A. Hufford, *Atmospheric 60 GHz Oxygen Spectrum: New Laboratory Measurements and Line Parameters*, **Journal of Quantitative Spectroscopy and Radiative Transfer**, 48, No. 5/6 pp 629-643, 1992.
- Liebe, H.J., G.A. Hufford, and M. Cotton, *Propagation Modeling of Moist Air and Suspended Water/Ice Particles at Frequencies Below 1000 GHz*, AGARD 52nd Specialists' Meeting of the Electromagnetic Wave Prop. Panel, Palma de Mallorca, Spain, 17-21 May 1993.
- Lundquist, G.L. and R.I. Potash, *WVR Brightness Temperature Corrections due to Finite Beamwidth*, **Interferometrics Inc./GSFC report**, 30 August 1985.
- Marini, J.W., *Correction of satellite tracking data from an arbitrary atmospheric profile*, **Radio Science** 7, 223-231, 1972.
- Marshall, J.S., and W. McK. Palmer, *The Distribution of Raindrops with Size*, **Journal of Meteorology**, 5, 1948.
- B.E. Martner, E.R. Westwater, E.G. Strauch, B.B. Stankov, D.B. Wuertz, W.L. Ecklund, K.S. Gage, D.A. Carter, J.B. Snider, J.C. Churnside, J.A. Shaw, K.P. Moran, J.C. Reynolds, "A Field Evaluation of Remote Sensor Measurements of Wind, Temperature, and Moisture for ARM Integrated Sounding System Research," **NOAA Technical Memorandum ERL WPL-211**, October 1991.
- B. Martner, D.B. Wuertz, B.B. Stankov, R.G. Strauch, E.R. Westwater, K.S. Gage, W.L. Ecklund, C.L. Martin, W.F. Dabberdt, "An Evaluation of Wind Profiler, RASS, and Microwave Radiometer Performance," **Bull. of Am. Meteor. Soc.**, 74, No. 4, 1993.
- Massonnet, Didier, Marc Rossi, Cesar Carmona, Frdric Adragna, Gilles Peltzer, Durt Fcigi, and Thierry Rabaute, *The displacement field of the Landers earthquake mapped by radar interferometry*, **Nature** No. 864, pp 138-142, 8 July 1993.
- Morgan, W., and M. G. DeBiche, *Horizontal gradients in the atmosphere; using numerical calculations to compute the tropospheric correction for GPS measure-*

ments, 1990 (preprint).

Neill, A.E., *Accuracy of Atmosphere Correction and Estimation from Rawinsonde Raytrace Calculation: 1. Instrument Errors*, **VLBI Geodetic Technical Memo #7**, MIT Haystack Observatory, 10 August 1992.

Oguchi, T., *Electromagnetic Wave Propagation and Scattering in Rain and Other Hydrometeors*, **Proceedings of the IEEE**, **71**, No. 9, September 1983.

Pruppacher, H.R., and R.L.Pitter, *A semi-empirical determination of the shape of cloud and rain drops*, **J.Atmos.Sci.** **28**, January 1971.

Ray, P.S., *Broadband Complex Refractive Indices of Ice and Water*, **Applied Optics**, **11**, No. 8, August 1972.

Röcken, C., *The Global Positioning System: A New Tool for Tectonic Studies*, PhD thesis, University of Colorado, 1988

Röcken, C., J. Johnson, R. Neilan, M. Cerezo, J. Jordan, M. Falls, L. Nelson, R. Ware, and M. Hayes, *The Measurement of Atmospheric Water Vapor: Radiometer Comparison and Spatial Variations*, **IEEE Transactions on Geoscience and Remote Sensing**, **29**, 3-8, 1991.

Röcken, C., and C. Meertens, *Monitoring selective availability dither frequencies and their effect on GPS data*, **Bulletin Geodesique NO. 65**, 162-169, 1991.

Röcken, C., Randolph Ware, Teresa Van Hove, Fredrick Solheim, Chris Alber, James Johnson, *Sensing Atmospheric Water Vapor with the global Positioning System*, in press **Geophysical Research Letters**, 1993.

Rogers, R.R., and A.P. Schwartz, *Mesoscale Fluctuations in Columnar Water Vapor*, **Journal of Applied Meteorology** **30**, pp 1305-1309, 1991.

Rogers, A.E.E., and A.E. Neill, *A "top down" model of the "dry" path delay through the atmosphere*, **VLBI Geodetic Technical Memo #10**, MIT Haystack Observatory, 30 August 1993.

Rosenkranz, P.W., *Shape of the 5mm Oxygen Band in the Atmosphere*, **IEEE Transactions on Antennas and Propagation**, **AP-23**, pp 498-506, July 1975.

Rothacher, Markus, *Orbits of Satellite Systems in Space Geodesy*, **Geodätisch-geophysikalische Arbeiten in der Schweiz**, **46**, 1992.

Saastamoinen, J., *Atmospheric correction for the troposphere and stratosphere in radio ranging of satellites*, in **The Use of Artificial Satellites for Geodesy**, **Geophysical Monographs Series**, **15**, S.W. Henricksen *et al.*, editors, pp 247-251, AGU Washington, D.C. 1972.

Saastamoinen, J., *Contributions to the Theory of Atmospheric Refraction part*

1, **Bulletin Geodesique** 105, 279-298, 1972.

Saastamoinen, J., *Contributions to the Theory of Atmospheric Refraction* part 2, **Bulletin Geodesique** 107, 13-34, 1972.

Schmidlin, F.J., J.J. Olivero and M.S. Nestler, *Can the standard radiosonde system meet special atmospheric research needs?*, **Geoph. Res. Letters** 9, 1109-1112, 1982

Schroeder, J. A., *A Comparison of Temperature Soundings Obtained from Simultaneous Radiometric, Radio-Acoustic, and Rawinsonde Measurements*, **JOAT** 7, No. 3, pp 495-503, June 1990.

Schroeder, J.A. and E.R. Westwater, *User's Guide to WPL Microwave Radiative Transfer Software*, **NOAA Technical Memorandum ERL WPL-213**, October 1991.

Snider, J.B., *Temporal and Spatial Variability of Atmospheric Water Vapor in the Los Angeles Basin*, 1984, (unpublished NOAA IOM).

Spilker, J.J. Jr., *GPS Signal Structure and Performance Characteristics*, **Journal of the Institute of Navigation** 25, No. 2, Summer 1978.

Spilker, J.J. Jr., *GPS Signal Structure and Performance Characteristics*, **Journal of the Institute of Navigation** 246, 1980.

Thayer, G.D., *An improved equation for the radio refractive index of air*, **Radio Science**, 9, October 1974.

Tralli, D., T. Dixon, and S. Stephens, *The Effect of Wet Tropospheric Path Delays on Estimation of Geodetic Baselines in the Gulf of California using GPS*, **Journal of Geophysical Research**, 93, 6545-6557, 1988.

Tralli, D. M., and S. M. Lichten, *Stochastic Estimation of Tropospheric Path Delays in Global Positioning System Geodetic Measurements*, **Bulletin Geodesique**, 64, 127-159, 1990.

Tralli, D. M., S. M. Lichten, and T. A. Herring, *Comparison of Kalman filter Estimates of Zenith Atmospheric Path Delays using the Global Positioning System and Very Long Baseline Interferometry*, **Radio Science**, 27, 999-1007, 1992.

Turco, R.P., *Atmospheric Chemistry*, in **Climate System Modeling**, K. Trenberth, editor, Cambridge Press, 1992.

Van Vleck, J.H., **The Theory of Electric and Magnetic Susceptibilities**, Oxford University Press, 1965.

Ware, R., C. Röcken, and J. Snider, *Experimental Verification of Improved GPS-Measured Baseline Repeatability Using Water Vapor Radiometer Corrections*,

IEEE Transactions on Geoscience and Remote Sensing, GE-23, 467-473, 1985.

Ware, R., C. Röcken, and K. J. Hurst, *A GPS Baseline Determination Including Bias Fixing and Water Vapor Radiometer Corrections*, **Journal of Geophysical Research**, 91, 9183-9192, 1986.

Ware, R., C. Röcken, Fredrick Solheim, Teresa Van Hove, Chris Alber, James Johnson, *Pointed Water Vapor Radiometer Corrections for Accurate Global Positioning System Surveying*, in press, **Geophysical Research Letters**, 1993.

Waters, J.W., *Absorption and Emission by Atmospheric Gases*, **Methods of Experimental Physics**, M.L.Meeks, 12, pp 142-176, 1976.

Westwater, E.R., *The accuracy of water vapor and cloud liquid determination by dual-frequency ground-based radiometry*, **Radio Science** 13, pp 677-685, July-August 1978.

Westwater, E.R., M.J. Falls, and I.A. Popo Fotino, *Ground-Based Microwave Radiometric Observations of Precipitable Water Vapor: A Comparison with Ground Truth from Two Radiosonde Observing Systems*, **JOAT**, 6, pp 724-730, August 1989.

Westwater, E.R., J.B. Snider, and M.J. Falls, *Ground-based Radiometric Observations of atmospheric Emission and Attenuation at 20.6, 31.65, and 90.0 GHz: A Comparison of Measurements and Theory*, **IEEE Trans. on Antennas and Propagation** 38, No. 10, October 1990.

Yuan, L., R. A. Anthes, R. H. Ware, C. Röcken, W. Bonner, M. Bevis, and S. Businger, *Sensing Climate Change Using the Global Positioning System*, **Journal of Geophysical Research** 98, 14,925-14,937, 1993.

Zuffery, C.H., *A Study of Rain Effects on Electromagnetic Waves in the 1- 600 GHz Range*, **MS Thesis**, Department of Electrical Engineering, University of Colorado, February 1972.